

# LACUSTRINE ICE-MARGIN DYNAMICS IN WEST GREENLAND

JOSEPH MALLALIEU



Submitted in accordance with the requirements for the degree  
of Doctor of Philosophy

The University of Leeds  
School of Geography

January 2020

The candidate confirms that the work submitted is his own, except where work which has formed part of jointly authored publications has been included. The contribution of the candidate and the other authors to this work has been explicitly indicated below. The candidate confirms that appropriate credit has been given within the thesis where reference has been made to the work of others.

The work in chapter 5 of this thesis has appeared in publication as follows:

- Mallalieu J., Carrivick J.L., Quincey D.J., Smith M.W. and James W.H.M. 2017. An integrated Structure-from-Motion and time-lapse technique for quantifying ice-margin dynamics. *Journal of Glaciology*. **63**, pp.937-949.
- Mallalieu J., 2016. Case Study: The application of an automated camera array to generate ice-margin feature geometry in west Greenland. In: Carrivick J.L., Smith M.S., and Quincey D.J. eds. *Structure from Motion in the Geosciences*. Chichester, Wiley Blackwell, pp.166-169.

The research was conceived and designed by Mallalieu, Carrivick, Quincey and Smith. Funding for the research was secured by Mallalieu and Quincey. Fieldwork was completed by Mallalieu, Carrivick, Quincey and James. Data processing and analysis was performed by Mallalieu, with support from Smith. Both manuscripts were written by Mallalieu with editorial comments from Carrivick, Quincey and Smith.

The work in chapter 6 of this thesis has appeared in publication as follows:

- Mallalieu, J., Carrivick, J.L., Quincey, D.J. and Smith, M.W. 2020. Calving Seasonality Associated With Melt-Undercutting and Lake Ice Cover. *Geophysical Research Letters*. **47**, GL086561.

The research was conceived and designed by Mallalieu, Carrivick, Quincey and Smith. Data processing and analysis was performed by Mallalieu. The manuscript was written by Mallalieu with editorial comments from Carrivick, Quincey and Smith.

This copy has been supplied on the understanding that it is copyright material and that no quotation from the thesis may be published without proper acknowledgement.

The right of Joseph Mallalieu to be identified as Author of this work has been asserted by Joseph Mallalieu in accordance with the Copyright, Designs and Patents Act 1988.

## Acknowledgements

I am indebted to my supervisors Jonathan Carrivick and Duncan Quincey, not only for devising this project, but for their consistent support, enthusiasm, and limitless patience over the last seven years. I would also like to thank my unofficial supervisor Mark Smith for sharing his SfM expertise and patiently answering the same questions about point cloud error at roughly six-month intervals throughout the entire project. The wider support of my friends and colleagues in the School of Geography is also gratefully acknowledged, particularly Paul Morris, Karen Bacon, Julie Peacock, Rob Pheasant, Megan Klaar, Andy Baird, Brian Irvine and Arjan Gosal for so willingly sharing their research and/or teaching wisdom over the years. I would also like to thank the School of Geography for awarding the Graduate Assistantship that allowed me to pursue this research, and the following organisations for providing additional funding for fieldwork and equipment: the Royal Institute of Chartered Surveyors Research Trust; the Mount Everest Foundation; the Gilchrist Educational Trust; Sigma Xi; and the River Basin Processes and Management research cluster in the School of Geography. I am also grateful for the detailed feedback provided by my examiners, Lee Brown and Tris Irvine-Flynn, which has improved this thesis.

I would like to thank my fellow PhDers in the School of Geography for enlivening the experience, in particular Will James, Greta Dargie, Freddie Draper and Sarah Fell, all of whom appear to be incapable of leaving the place. I would also like to thank my friends outside the university whom I have not seen nearly enough of over the last seven years for their excellent company, particularly Johnny, Sarah, Andy, Cammie, Mark, Tom, Chessterton and Rich.

Finally, I'd like to thank my family. My parents Tim and Carol, who met at this university many moons ago, for their constant support and endearing bemusement about why anyone would willingly undertake a PhD. And my partner Cassandra Raby, for many things, but particularly for reminding me to never take things too seriously. Obviously, I don't learn, but thanks for trying.

## Abstract

There has been a progressive increase in the number and area of ice-marginal lakes along the western margin of the Greenland Ice Sheet (GrIS) since the late 1980s. Ice-marginal lake formation and growth have been widely associated with accelerated rates of mass loss and terminus recession at alpine glaciers, yet their impacts on the GrIS have remained unquantified. This thesis therefore investigated the influence of ice-marginal lakes on ice-margin dynamics in west Greenland at multiple spatial and temporal scales, using both established remote sensing techniques and the novel integration of time-lapse photography with Structure-from-Motion and Multi-View Stereo.

A regional-decadal scale analysis of ice-margin change along a ~5000 km length of the GrIS revealed that lake-terminating ice-margins receded faster than their terrestrial counterparts between 1987 and 2015. In addition, the rate of recession at lake-terminating ice-margins accelerated over the study period and increasingly outpaced recession at terrestrial ice-margins. Altitude, latitude, lake area and the length of the lake – ice-margin interface were also identified as significant controls on rates of lake-terminating ice-margin recession.

Local-seasonal scale ice-margin dynamics were investigated using the first continuous year-round volumetric record of calving at a lacustrine ice-margin. These data highlighted two distinct calving regimes; with melt-undercutting driving high calving rates under ice-free lake conditions, and force imbalances at the ice-cliff driving low calving rates when the lake was frozen.

These results are important because they demonstrate that ice-marginal lakes are key regulators of ice-margin dynamics at the GrIS. The quantitative data derived through this study provide an empirical foundation upon which modelling efforts can incorporate the influence of ice-marginal processes. This is particularly pertinent given that rates of mass loss and recession at lake-terminating margins of the GrIS are likely to accelerate in coming decades in response to continued ice-marginal lake expansion and a lengthening melt season.

# Contents

Acknowledgements.....	iii
Abstract.....	iv
List of Tables.....	viii
List of Figures.....	ix
List of Abbreviations.....	xiii

## Chapter 1: Introduction

1.1 Terminology and Focus.....	1
1.2 Research Rationale.....	1
1.3 Research Aims and Objectives.....	3
1.4 Thesis Structure.....	4

## Chapter 2: Literature Review and Study Area

2.1 Ice-Marginal Lakes.....	6
2.1.1 Form, Setting and Evolution.....	6
2.1.2 Contemporary and Historical Distribution.....	7
2.2 Lacustrine Ice-Margin Dynamics.....	8
2.2.1 Ice-Marginal Lake – Glacier Interactions.....	8
2.2.2 Frontal Ablation.....	11
2.2.3 Summary.....	14
2.3 Regional Setting.....	14
2.3.1 The Greenland Ice Sheet.....	14
2.3.2 Russell Glacier Ice-Dammed Lake.....	16

## Chapter 3: Methods Overview

3.1 Introduction.....	20
3.2 Regional-Decadal Scale Lacustrine Ice-Margin Dynamics.....	20
3.3 Local-Seasonal Scale Lacustrine Ice-Margin Dynamics.....	22
3.3.1 Field Surveying and Time-Lapse Photography.....	22
3.3.2 Structure-from-Motion and the Time-Lapse Camera Array.....	23
3.3.3 Malham Cove Pilot Study.....	24
3.4 Summary.....	27

## Chapter 4: A Multi-Decadal Analysis of Lacustrine Ice-Margin Change in West Greenland

4.1 Abstract.....	29
-------------------	----

4.2 Introduction.....	29
4.3 Methods.....	32
4.3.1 Landsat Scene Selection.....	32
4.3.2 Ice-Marginal Lake Inventory.....	34
4.3.3 Ice-Margin Vectors.....	37
4.3.4 Measurements of Ice-Margin Change.....	37
4.3.5 Statistical Analyses.....	38
4.4 Results.....	39
4.4.1 Model Fit.....	39
4.4.2 Ice-Margin Change at Lacustrine, Terrestrial and Marine Margins.....	39
4.4.3 Controls on Lacustrine Ice-Margin Change.....	43
4.5 Discussion.....	44
4.5.1 Ice-Margin Change in West Greenland.....	44
4.5.2 Lacustrine Ice-Margin Recession.....	46
4.5.3 Implications and Future Research.....	47
4.6 Conclusions.....	49

**Chapter 5: An Integrated Structure-from-Motion and Time-Lapse Technique for Quantifying Ice-Margin Dynamics**

5.1 Abstract.....	51
5.2 Introduction.....	51
5.3 Study Site.....	54
5.4 Methods.....	55
5.4.1 Time-Lapse Camera Array Setup.....	55
5.4.2 Ground Control Points.....	57
5.4.3 Point Cloud Processing.....	57
5.5 Results.....	61
5.5.1 Camera Array Viability and Point Cloud Construction.....	61
5.5.2 Point Cloud Parameters.....	62
5.5.3 Quantification of Ice-Margin Dynamics.....	65
5.6 Discussion.....	66
5.6.1 Camera Array Geometry.....	67
5.6.2 Ambient Lighting Effects.....	67
5.6.3 Point Cloud Error.....	68
5.6.4 Ground Control Point Distribution.....	69
5.6.5 Camera Clocks and Workflow Automation.....	70

5.6.6 Detection of Ice-Margin Dynamics.....	70
5.6.7 Appraisal Against Terrestrial Laser Scanning .....	71
5.7 Conclusions and Recommendations.....	71

**Chapter 6: Seasonal Variability in Calving Processes at a Lacustrine Margin of the Greenland Ice Sheet**

6.1 Abstract.....	75
6.2 Introduction.....	75
6.3 Data and Methodology.....	77
6.3.1 Study Site.....	77
6.3.2 Image Acquisition and Point Cloud Generation.....	77
6.3.3 Point Cloud Analysis.....	78
6.3.4 Calving Classification.....	82
6.3.5 Lake Volume and Meteorological Data.....	84
6.4 Results.....	85
6.4.1 Calving Event Attributes.....	85
6.4.2 Seasonal Variability in Calving Dynamics.....	86
6.4.3 Effects of Sudden Lake Drainage on Calving Dynamics.....	88
6.5 Discussion.....	89
6.5.1 Calving Processes.....	89
6.5.2 Seasonal Variability in Calving Dynamics.....	91
6.5.3 Effects of Sudden Lake Drainage on Calving Dynamics.....	93
6.5.4 Methodological Evaluation.....	94
6.6 Conclusions.....	95

**Chapter 7: Discussion and Conclusions**

7.1 Introduction.....	97
7.2 Research Summary.....	97
7.3 Research Implications.....	99
7.4 Future Research.....	101
7.4.1 Local-Seasonal Scale Priorities.....	103
7.4.2 Regional-Decadal Scale Priorities.....	104
7.4.3 Theoretical Approaches.....	106
7.4.4 Broader Applications of the Time-Lapse Camera Array.....	107
7.5 Conclusions.....	108

<b>References.....</b>	<b>110</b>
------------------------	------------

## List of Tables

Table 2.1. Selected studies of contemporary ice-marginal lakes.....	8
Table 2.2. Dates and available parameters of known Russell Glacier IDL drainage events...19	
Table 3.1. Parameters of key optical imaging satellite sensors operating over the Greenland Ice Sheet. Table updated from Quincey and Luckman (2009).....	21
Table 4.1. Attributes of Landsat scenes used in this study.....	33
Table 4.2. LMM and Robust LMM variables and coefficients.....	39
Table 4.3. Summary statistics of ice-margin composition throughout the study period.....	40
Table 4.4. Summary statistics of ice-margin change throughout the study period.....	40
Table 4.5. LMM results. Significant relationships are highlighted in bold.....	41
Table 5.1. Survey range between the cameras and ice-margin.....	57
Table 5.2. Seasonal variations in point cloud parameters.....	59
Table 5.3. Standard deviations and mean changes for inactive point cloud pairs.....	61
Table 5.4. Area and volume calculations for calving events displayed in Figure 5.7. Note 'i' and 'ii' denote distinct calving events detected in the same active point cloud pair (see Figure 5.7).....	65
Table 6.1. Attributes of point clouds employed in calving analysis and associated lake measurements.....	79
Table 6.2. Tools and associated values employed for point cloud analysis in CloudCompare. Where parameters are absent from the table default settings were adopted. Note that all clouds were transformed so that the ice-cliff was normal to the Y axis prior to analysis.....	80
Table 6.3. Standard deviations of M3C2 distances measured between vertical 30 m <sup>2</sup> subsections of the ice-margin lacking structural changes.....	82
Table 6.4. Summary statistics of calving mechanisms, areas and volumes for events detected between 27 July 2014 and 20 September 2015 at Russell Glacier IDL.....	85



## List of Figures

Figure 2.1. Principal topographic settings and potential drainage pathways of ice-marginal lakes: (a) proglacially ice-dammed; (b) in a trunk valley dammed by a tributary glacier; (c) between a glacier at its terminal moraine; (d) dammed by converging glaciers; and (e) laterally ice-dammed. Figure adapted from Tweed and Russell (1999).....	7
Figure 2.2. Cumulative anomalies in GrIS mass balance and equivalent sea level contribution between 1980 and 2018. Total change (dark blue) can be partitioned into changes associated with surface mass balance (green) and ice dynamics (light blue). Figure from Shepherd et al. (2020).....	15
Figure 2.3. Regional setting of Russell Glacier in west Greenland, showing the ice-dammed lake (IDL), and the subglacial (dashed blue line) and subaerial (solid blue line) pathway of outburst floods emanating from sudden lake drainage events. The maximum lake extent is delineated by the dashed white line. The red arrow denotes the position and orientation of the photographs in Figure 2.4. Basemap from Google Earth.....	17
Figure 2.4. Oblique images of Russell Glacier IDL on (a) 14 <sup>th</sup> September and (b) 19 <sup>th</sup> September 2013, either side of the 15 <sup>th</sup> September drainage event. Note in (b) the stranded icebergs and thermo-erosional notch cut at the pre-drainage lake level (denoted by the black arrow). For scale, the freeboard of the ice-cliff following lake drainage is ~60 m. The site and orientation of the photographs is denoted by the red arrow in Figure 2.3. Photographs by Adam Lyberth.....	18
Figure 3.1. Satellite image of Russell Glacier IDL in 2014, illustrating potential sites for trail camera installation between 500 m and 1000 m from the centre of the lacustrine ice-margin. Basemap from Google Earth.....	25
Figure 3.2. Overview of the time-lapse camera-array pilot study at Malham Cove. Grey shading denotes positions with an obscured view of the cove following viewshed analysis. Basemap from Digimap.....	25
Figure 3.3. Dense point clouds of Malham Cove reconstructed from image sets acquired by (a) the LtL Acorn 5210A trail camera and (b) the Sony Nex-5 bridge DSLR camera.....	26
Figure 4.1. Study location in west Greenland. The spatial extent of the analysis is illustrated with false-colour Landsat scenes from 2015 (see Table 4.1).....	31
Figure 4.2. Illustration of key stages in ice-margin vector construction: (a) unprocessed Landsat ETM+ band 2 (green) scene affected by SLC failure; (b) mosaiced scene to fill SLC induced gaps; (c) NDSI classification; (d) water mask; (e) application of NDSI threshold and water mask to differentiate snow and ice from land and water; and (f) tidied ice-margin vector.....	34

Figure 4.3. Example of dataset, comprising terrestrial, lacustrine and marine ice-margins, and the respective points/centroids used for measurements of ice-margin change. Small circles on marine and lacustrine ice-margins represent the vertices over which distance measurements are averaged. Basemap: 2015 false-colour Landsat OLI scene..... 35

Figure 4.4. Illustration of temporal variation in lake area and lake – ice-margin intersect over the survey period. Note partial lake drainage between 2000-2005, and subsequent refilling.....36

Figure 4.5. Box plots of ice-margin change throughout the study period at: (a) terrestrial, lacustrine and marine margins; and (b) terrestrial and lacustrine margins only. To improve clarity, 7 and 21 outlying data points have been cropped from (a) and (b) respectively..... 42

Figure 4.6. Linear regression of annual change and year, showing trends in ice-margin recession at terrestrial and lacustrine margins. The final year of each epoch has been used to plot the linear relationship. Grey shading represents the 95% confidence interval. Individual data points have been removed to improve clarity..... 42

Figure 4.7. Linear regressions of annual change at lacustrine ice-margins and lake parameters, comprising: (a) latitude; (b) altitude; (c) lake area; (d) intersect length; and (e) year. NB. The final year of each epoch has been used to plot the linear relationship in (e). Grey shading represents the 95% confidence interval. Individual data points have been removed to improve clarity..... 43

Figure 5.1. Study location on the northern margin of Russell Glacier, western Greenland (inset) and camera array geometry. Heavier blue shading represents increased camera overlap..... 54

Figure 5.2. Example of a trail camera installation at the lake shore.....56

Figure 5.3. Schematic of point cloud differencing workflow: (a & b) Point clouds from 13:00 on 25 and 26 July 2014 respectively; (c) the resultant output of the M3C2 cloud differencing algorithm; and (d) the M3C2 output trimmed to the sector of ice-front possessing greatest camera coverage (note the black square denotes the location of 30 m<sup>2</sup> patch). The differencing of inactive cloud pairs provides a measure of internal consistency in cloud geometry. The changes detected on the stable lake shores are indicative of poor camera coverage in peripheral survey areas.....60

Figure 5.4. Aerial view of dense point cloud derived from imagery acquired at 13:00 on 25 July 2014, illustrating the spatial extent of cloud reconstruction and camera overlap. Black bars delineate the trimmed section of ice-margin used for analysis..... 60

Figure 5.5. (a) Cropped image of ice-margin recorded at 13:00 on 25 July 2014 from camera A12; (b) corresponding view of the derived dense-point cloud; (c) enlargement of area bounded by dashed line in panel b, with detail illustrating the effect of crevasse peaks on point cloud reconstruction of the ice sheet surface. Note for scale the vertical height of the ice-margin is ~50 m..... 63

Figure 5.6. (a) Images recorded by camera A11 on 25 July 2014 showing daily variation in lighting conditions and accepted and rejected feature matches (blue and white circles respectively); (b) corresponding histograms of reprojection error for accepted feature matches; (c) reprojection error for individual points in the sparse point clouds derived from the (i) 09:00, (ii) 13:00, and (iii) 17:00 imagery..... 64

Figure 5.7. Camera imagery and M3C2 outputs for calving events identified in the active point cloud pairs. Events are dated: (a) 20-21 August 2014; (b) 19-20 February 2015; (c) 12-13 June 2015; and (d) 10-11 August 2015. Note for scale the vertical height of the ice-margin is ~50 m..... 66

Figure 6.1. Schematic of workflow for point cloud analysis and derivation of calving data..... 81

Figure 6.2. Classification of the five calving mechanisms observed at Russell Glacier IDL, based on geometric changes at the ice-margin (determined via point cloud differencing), interpretation of camera imagery pre- and post-calving, and existing calving categorisations. Approximate calving event magnitudes are indicated by the scale bars on the differenced point clouds..... 83

Figure 6.3. 2D profiles illustrating topographic changes at the ice-cliff associated with the 2014 and 2015 lake drainage events, including characteristics of key calving mechanisms. The positions of the 2D profiles along the ice-cliff are delineated by transects A-E in Figure 6.7. (a) ~1 m deep thermo-erosional notch at the waterline revealed by lake drainage; (b) outward toppling of ice-cliff at higher elevations prior to failure; (c) ice-fall above notch, reflecting undercutting and structural weaknesses in the ice-cliff; (d) collapse spanning full height of the ice-cliff; (e) failure at the waterline, likely to reflect undercutting by a thermo-erosional notch..... 84

Figure 6.4. Area-volume relationship for calving events recorded at Russell Glacier IDL..... 86

Figure 6.5. Seasonal record of calving, lake and meteorological activity at Russell Glacier IDL between 27 July 2014 and 20 September 2015. (a) Mean daily air temperature; (b) mean daily lake temperature from spring 2010 and 2012 (from Carrivick et al., 2017a); (c) lake volume, indicating onset of lake freeze/thaw and occurrence of drainage events on 3 August 2014 and 28 July 2015; (d) calving volume and cumulative calving volume over the survey duration; (e) calving rate; (f) calving volume by mechanism (%); (g) calving frequency by mechanism. Note that calving data were measured at 7 ( $\pm 1$ ) day intervals from 27 July to 19 Oct 2014 and 11 May to 20 Sept 2015, but are aggregated and plotted here at 28 day intervals to maintain a consistent sampling interval across the survey.....87

Figure 6.6. Spearman’s rank correlation matrix of calving and environmental variables at Russell Glacier IDL. Statistically significant relationships ( $p < 0.05$ ) are denoted by a coloured circle. (a) Relationships between calving and environmental variables whilst the lake remained ice-free (27 July - 29 September 2014 and 26 June - 20 September 2015); (b) relationships between calving and environmental variables whilst the lake was partially or fully frozen (29 September 2014 - 26 June 2015).....88

Figure 6.7. Spatio-temporal record of calving associated with lake drainage events commencing on the 3 August 2014 and 28 July 2015. Transects A-E denote the positions of the 2D ice-cliff profiles illustrated in Figure 6.3..... 89

Figure 7.1. Conceptual diagram illustrating the key impacts of ice-marginal lakes on the ice-margin dynamics of the GrIS at (a) a local-seasonal scale and (b) a regional-decadal scale. Impacts observed and/or quantified in this thesis are italicised. Note exaggerated vertical scale for illustrative purposes..... 102

## List of Abbreviations

2D	Two-Dimensional
3D	Three-Dimensional
AIC	Akaike Information Criterion
ASTER	Advanced Spaceborne Thermal Emission and Reflection Radiometer
BP	Before Present
DEM	Digital Elevation Model
dGPS	Differential Global Positioning System
DOY	Day of Year
DSLR	Digital Single-Lens Reflex
ENVI	Environment for Visualizing Images
ETM+	Enhanced Thematic Mapper Plus
GCP	Ground Control Point
GLOF	Glacial Lake Outburst Flood
GPS	Global Positioning System
GrIS	Greenland Ice Sheet
IDL	Ice-Dammed Lake
LiDAR	Light Detection and Ranging
LMM	Linear Mixed-Effects Model
LWIR	Longwave Infrared
M3C2	Multi-Scale Model-to-Model Cloud Comparison
MMS	Multimedia Messaging Service
MODIS	Moderate Resolution Imaging Spectroradiometer
MP	Megapixel
MSS	Multispectral Scanner System
MVS	Multi-View Stereo
NDSI	Normalised Difference Snow Index
NDWI	Normalised Difference Water Index
NIR	Near Infrared
OBIA	Object-Based Image Analysis
OLI	Operational Land Imager
PGIC	Peripheral Glaciers and Ice Caps
RAM	Random Access Memory

RMSE	Root-Mean-Square Error
SD	Standard Deviation
SfM	Structure-from-Motion
SLC	Scan Line Corrector
SPOT	Satellite Pour l'Observation de la Terre
SWIR	Shortwave Infrared
TIR	Thermal Infrared
TLS	Terrestrial Laser Scanning
TM	Thematic Mapper
USGS	United States Geological Survey
VNIR	Visible and Near Infrared

# Chapter 1

## Introduction

### 1.1 TERMINOLOGY AND FOCUS

Lakes are a ubiquitous feature of proglacial environments wherever glacial meltwater is constrained by topography, sedimentary deposits, or the ice-margin itself. Such lakes have been increasingly recognised within the literature as important regulators of ice-margin dynamics, glacier mass loss, and associated meltwater and sediment fluxes (Carrivick and Tweed, 2013). However, the terminology associated with these landforms is often inconsistent, with a wide variety of modifiers commonly employed to describe lakes with contrasting topographic settings or physical characteristics within the proglacial environment (including glacial-, proglacial-, ice-contact, ice-dammed and ice-marginal). In this thesis, the term *ice-marginal lake* is employed to strictly describe those lakes situated adjacent to, but in direct contact with, ice-margins. The precondition that lakes are in physical contact with ice-margins is specifically imposed to consider their influence on ice-margin dynamics.

### 1.2 RESEARCH RATIONALE

Contemporary deglaciation is driving increases in the number and size of ice-marginal lakes in many of the world's glacierised regions, including: Iceland (Schomacker, 2010; Dell et al., 2019; Gudmundsson et al., 2019); the European Alps (Paul et al., 2007; Buckel et al., 2018); the Hindu Kush, Karakoram and Himalaya (Zhang et al., 2015; Nie et al., 2017); the Southern Alps of New Zealand (Kirkbride, 1993; Chinn, 1996); the Peruvian Cordillera Blanca (Emmer et al., 2020); Patagonia (Loriaux and Casassa, 2013; Wilson et al., 2018); and west Greenland (Carrivick and Quincey, 2014). The increased prevalence of ice-marginal lakes is significant because of their propensity to accelerate rates of mass loss and glacier recession through a range of thermo-mechanical controls at the ice-margin, including: enhanced basal water pressure, buoyancy and sliding (e.g. Anderson et al., 2005; Riesen et al., 2010; Tsutaki et al., 2011); terminus flotation (e.g. Naruse and Skvarca, 2000; Mayer et al., 2008; Tsutaki et al., 2013); and the onset and promotion of calving (e.g. Warren et al., 2001; van der Veen, 2002). Furthermore, ice-marginal lakes are particularly susceptible to catastrophic drainage in the form of glacial lake outburst floods (GLOFs), which pose significant threats to downstream communities and infrastructure (Tweed and Russell, 1999; Carrivick and Tweed, 2016).

However, despite the growing observational record of ice-marginal lake formation and accelerated glacier recession, a sparsity of quantitative data means that lacustrine ice-margin dynamics, particularly lacustrine calving processes, remain poorly understood and are thus omitted from mechanistic models of glacier change and sea level rise.

The enhanced formation and growth of ice-marginal lakes in west Greenland is therefore of particular significance because: (i) the Greenland Ice Sheet (GrIS) is one of largest individual contributors to current and predicted sea level rise; and (ii) dynamical change at ice sheet margins is one of the greatest sources of uncertainty in sea level rise projections (Church et al., 2013). However, the contemporary impacts of ice-marginal lakes on the dynamics of the GrIS margin remain unquantified and existing knowledge of lacustrine ice-margin dynamics is almost exclusively derived from alpine glaciers. Consequently, a detailed assessment of lacustrine ice-margin dynamics at the GrIS is increasingly necessary to: (i) determine the dynamic response of the ice sheet to ice-marginal lake expansion; (ii) refine projections of sea level rise; and (iii) provide better constraints on the magnitude, location and frequency of GLOF events.

Regional-decadal scale analyses of lacustrine ice-margin dynamics, particularly changes in ice-margin extent, velocity, structure and surface elevation (e.g. Howat et al., 2008; Mernild et al., 2012; Willis et al., 2012; King et al., 2019), have been facilitated in recent decades by the increasing availability and longevity of satellite remote sensing archives. Conversely, local-seasonal scale lacustrine ice-margin dynamics, such as buoyancy and calving, remain poorly constrained due to the sparsity of quantitative datasets arising from the hazardous nature of fieldwork at lacustrine ice-margins. In addition, the climatic and financial constraints of fieldwork have confined existing local-scale analyses of ice-margin dynamics to the melt season, thus neglecting seasonal variability in ice-marginal processes. Although time-lapse photography can be employed to acquire extended observational records of change at water-terminating ice-margins (e.g. Amundson et al., 2010; Rosenau et al., 2013; Minowa et al., 2018), the absence of volumetric data limits the capacity of the technique for quantifying ice-margin dynamics. However, the generation of high-resolution topographic datasets from photographic image archives is now possible due to recent advances in the fields of Structure-from-Motion (SfM) and Multi-View Stereo (MVS) photogrammetry (Fonstad et al., 2013; Smith et al., 2016a; Eltner et al., 2016). Consequently, the integration of time-lapse photography and SfM-MVS techniques has significant potential for the



characterisation and quantification of local-scale lacustrine ice-margin dynamics over extended durations, although such an approach is yet to be explored in the literature.

### **1.3 RESEARCH AIMS AND OBJECTIVES**

The overall purpose of this thesis is to quantitatively assess the impact of ice-marginal lakes on the ice-margin dynamics of the GrIS at multiple spatial and temporal scales. West Greenland is the optimal site for such an analysis because it has the greatest regional concentration of land-terminating, and thus lacustrine, margins of the GrIS, and has also experienced some of the highest rates of atmospheric warming recorded in the Arctic since the 1980s (Carr et al., 2013; Ding et al., 2014). Focusing analysis here is also particularly pertinent given that this sector of the ice sheet is forecast to undergo some of the greatest rates of ice-margin recession and reductions in ice cover over the next millennia (Aschwanden et al., 2019). The three primary aims of this thesis and their respective objectives are outlined below:

1. To perform a regional-decadal scale analysis of changes in ice-margin extent along the western margin of the GrIS.
  - a. Generate an inventory of ice-marginal lakes in west Greenland at systematic intervals between 1987 and 2015.
  - b. Delineate the western margin of the GrIS at systematic intervals between 1987 and 2015.
  - c. Conduct a comparative analysis of ice-margin advance and recession at lacustrine, terrestrial and marine terminating ice-margins.
  - d. Investigate the relationships between ice-marginal lake properties and rates of change at lacustrine ice-margins.
  
2. To develop a new method for the extended acquisition of fine spatio-temporal resolution datasets of local-seasonal scale ice-margin dynamics.
  - a. Investigate the capacity of SfM-MVS software to reconstruct 3D feature geometry from sparse image datasets acquired using time-lapse cameras.
  - b. Install an array of time-lapse cameras at a lacustrine terminating margin of the GrIS with sufficient image overlap to permit point cloud generation and analysis.
  - c. Evaluate the capacity of the camera array to detect and quantify ice-margin dynamics by analysing multi-temporal point clouds of ice-margin geometry.

3. To quantify seasonal variability in calving processes at a lacustrine margin of the GrIS.
  - a. Generate point clouds of ice-margin geometry systematically between July 2014 and September 2015 using the time-lapse camera image dataset.
  - b. Develop an extended (>1 yr) volumetric record of calving by differencing successive point clouds.
  - c. Analyse spatial and temporal patterns in calving event frequency, volume and mechanism, and their relationships with environmental drivers.
  - d. Opportunistically explore the effects of two sudden lake drainage events on calving processes and ice-margin stability.

#### **1.4 THESIS STRUCTURE**

The results presented in chapters 4-6 of this thesis are designed to stand alone as independent journal articles and thus each includes a dedicated literature review and discussion. Consequently, the remaining chapters of the thesis are designed to provide a succinct overview of lacustrine ice-margin dynamics, introduce the study site and selected methodologies, and to provide a unifying synthesis of the research and consideration of its implications.

- Chapter 2, Literature Review and Study Area: summarises existing knowledge of lacustrine ice-margin dynamics and provides local and regional context for the selected study sites in west Greenland.
- Chapter 3, Methods Overview: details the rationale for the respective research approaches employed for the regional-decadal and local-seasonal scale analyses of lacustrine ice-margin dynamics. This chapter also provides background on the development and piloting of the time-lapse camera array used to acquire the datasets in chapters 5 and 6.
- Chapter 4, Results 1: presents a regional-decadal scale remote sensing and statistical analysis of ice-margin extent at the terrestrial, lacustrine and marine margins of the GrIS in west Greenland between 1987 and 2015. This section also includes an assessment of how ice-marginal lake parameters affect rates of lacustrine ice-margin recession.

- Chapter 5, Results 2: presents and evaluates a new methodology for acquiring fine spatio-temporal resolution datasets of local-seasonal scale ice-margin dynamics via the integration of time-lapse photography with developments in the fields of SfM and MVS. This work is the basis of a research article published in the Journal of Glaciology in 2017 (Mallalieu et al., 2017).
- Chapter 6, Results 3: utilises the technique developed in the preceding chapter to explore local calving processes at an ice-marginal lake in west Greenland over a 14 month period. A total of 56 point clouds of the ice-margin are analysed to investigate seasonal calving processes and assess the response of the ice-margin to two sudden lake drainage events. This work is the basis of a research article published in Geophysical Research Letters in 2020 (Mallalieu et al., 2020).
- Chapter 7, Discussion and Conclusions: summarises the work presented in the thesis, considers the wider implications of the results and identifies priorities for future research.

## Chapter 2

### Literature Review and Study Area

#### 2.1 ICE-MARGINAL LAKES

##### 2.1.1 FORM, SETTING AND EVOLUTION

Ice-marginal lakes are prevalent landforms at the margins of many glaciers, ice caps and ice sheets, but exhibit considerable diversity in form, setting and scale. They typically form where glacial meltwater is impounded by a natural dam, most commonly composed of ice, bedrock, moraine deposits or landslide debris (Costa and Schuster, 1988). Some of the principle topographic settings of the ice-marginal lakes cited in this chapter are illustrated in Figure 2.1. The physical setting of an ice-marginal lake and the composition of its dam have been shown to be key indicators of lake stability (Carrivick and Tweed, 2013). In particular, ice- and moraine-dammed lakes are susceptible to abrupt drainage events that cause glacial lake outburst floods (GLOFs), which are major agents of downstream landscape change and significant natural hazards in many glacial environments (Tweed and Russell, 1999; Clague and Evans, 2000; Carrivick and Tweed, 2016; Dubey and Goyal, 2020; Veh et al., 2020). The composition of the lake dam also determines the possible lake drainage mechanisms and pathways. For example, ice-dammed lakes are susceptible to draining subglacially if the flotation threshold of an ice-dam is exceeded by the depth of the lake (e.g. Anderson et al., 2005; Riesen et al., 2010; Carrivick et al., 2017a), ice-marginally if the ice-dam fails mechanically (e.g. Walder and Costa, 1996), or supraglacially if the ice-surface downwastes below the lake level (e.g. Mayer and Schuler, 2005) (Figure 2.1). Furthermore, because lake evolution is closely linked to ice-margin dynamics, enhanced ice-marginal lake activity, such as lake formation, growth and drainage, can be an indicator of instability at an ice-margin (Carrivick and Tweed, 2013). For example, advancing and thickening ice-margins can encourage lake formation by impounding meltwater, particularly in trunk valleys (Figure 2.1b), whereas receding and downwasting ice-margins create favourable conditions for lake formation between glacier termini and their respective terminal moraines (Figure 2.1c). Receding and thinning ice-margins can also promote lake drainage events in response to the increased fragility and reduced flotation threshold of ice-dams, or the decoupling of confluent glaciers (Figure 2.1d) (Evans and Clague, 1994; Tweed and Russell, 1999).

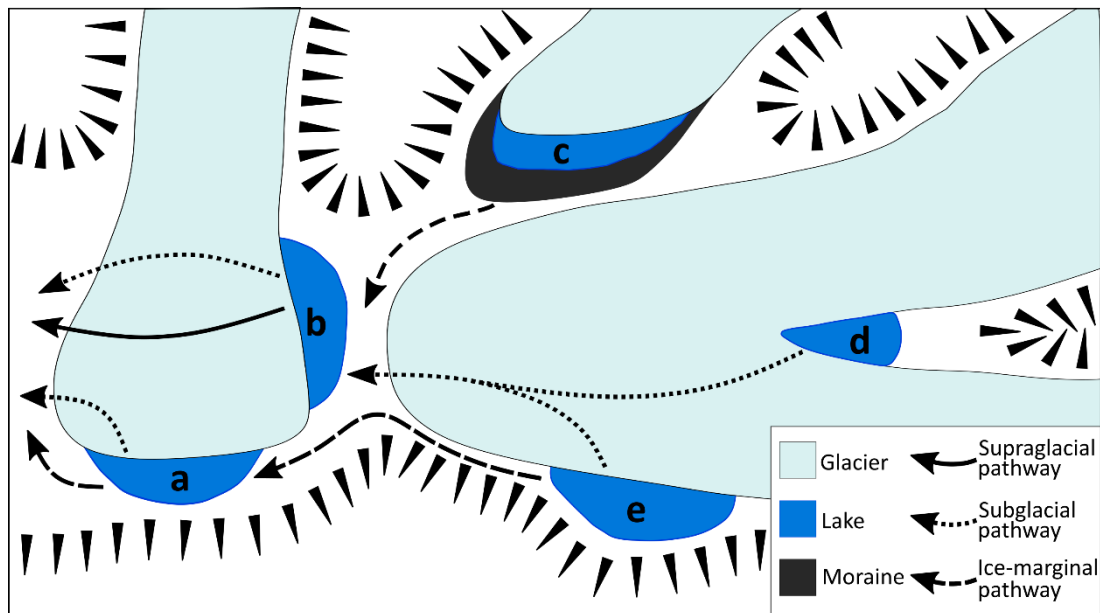


Figure 2.1. Principal topographic settings and potential drainage pathways of ice-marginal lakes: (a) proglacially ice-dammed; (b) in a trunk valley dammed by a tributary glacier; (c) between a glacier at its terminal moraine; (d) dammed by confluent glaciers; and (e) laterally ice-dammed. Figure adapted from Tweed and Russell (1999).

### 2.1.2 CONTEMPORARY AND HISTORICAL DISTRIBUTION

The presence of ice-marginal lakes is increasingly well documented in the majority of the world's glacierised regions (Table 2.1). However, there is a bias in the existing literature to studies of lakes situated at the margins of alpine glaciers in the mid-latitudes, and very few studies of ice-marginal lakes abutting ice caps and ice sheets. Furthermore, many glacierised regions have experienced recent growth in the number and size of ice-marginal lakes in response to contemporary deglaciation, including: Iceland (Schomacker, 2010; Dell et al., 2019; Gudmundsson et al., 2019); the European Alps (Paul et al., 2007; Buckel et al., 2018); the Hindu Kush, Karakoram and Himalaya (Zhang et al., 2015; Nie et al., 2017); the Southern Alps of New Zealand (Kirkbride, 1993; Chinn, 1996); the Peruvian Cordillera Blanca (Emmer et al., 2020); Patagonia (Loriaux and Casassa, 2013; Wilson et al., 2018); and west Greenland (Carrivick and Quincey, 2014).

Extensive ice-marginal lakes were a characteristic feature at the margins of continental ice masses during the late Quaternary deglaciation, including the Laurentide (Teller, 1995; Utting and Atkinson, 2019), Scandinavian (Rosentau et al., 2009; Stroeven et al., 2016; Patton et al., 2017) and Barents-Kara ice sheets (Mangerud et al., 2004; Larsen et al., 2006). Climate modelling has demonstrated that the scale and significant heat capacity of the ice-marginal lakes in central Eurasia was sufficient to regulate local climate and modify rates of ice sheet

advance and decay (Krinner et al., 2004). In addition, several studies have also identified ice-marginal lakes as key controls on ice-stream initiation and subsequent rapid ice sheet collapse during deglaciation (Stokes and Clark, 2003; Stokes and Clark, 2004; Demidov et al., 2006; Perkins and Brennand, 2015). Consequently, the growth and coalescence of ice-marginal lakes at contemporary ice sheet margins may be indicative of a period of enhanced lacustrine forcing of ice sheet dynamics.

Table 2.1. Selected studies of contemporary ice-marginal lakes.

Region	Selected references
European Alps	Huggel et al., 2002; Deline et al., 2004; Diolaiuti et al., 2006; Huss et al., 2007; Sugiyama et al., 2008; Riesen et al., 2010; Tsutaki et al., 2011; Tsutaki et al., 2013.
Scandinavian Mountains	Duck and McManus, 1985; Knudsen and Theakstone, 1988; Kennett et al., 1997.
Caucasus Mountains	Stokes et al., 2007.
Tien Shan	Mayer et al., 2008; Kingslake and Ng, 2013; Bolch et al., 2011; Engel et al., 2012.
Hindu Kush, Karakoram and Himalaya	Komori, 2008; Gardelle et al., 2011; Basnett et al., 2013; Zhang et al., 2015*; Nie et al., 2017; Brun et al., 2019*; King et al., 2019; Tsutaki et al., 2019; Watson et al., 2020.
Tibetan Plateau	Chen et al., 2007; Yao et al., 2010; Wang et al., 2011.
Southern Alps (New Zealand)	Kirkbride, 1993; Chinn, 1999; Warren and Kirkbride, 2003; Röhl, 2006; Quincey and Glasser, 2009; Dykes et al., 2011; Purdie et al., 2016.
Patagonia	Naruse and Skvarca, 2000; Warren et al., 2001; Skvarca et al., 2003; Haresign and Warren, 2005; Loriaux and Casassa, 2013; Minowa et al., 2018.
Pacific Coast Ranges (USA & Canada)	Anderson et al., 2003; Motyka et al., 2003a,b; Walder et al., 2006; Boyce et al., 2007; Trussel et al., 2013; Wilcox et al., 2014; Wolfe et al., 2014; Kienholz et al., 2020.
Greenland Ice Sheet	Furuya and Wahr, 2005; Mayer and Schuler, 2005; Russell et al., 2011; Carrivick and Quincey, 2014.
Svalbard	Bennett et al., 1998.
Iceland	Roberts et al., 2005; Geirsdottir et al., 2008; Schomacker, 2010; Storrar et al., 2017; Dell et al., 2019; Gudmundsson et al., 2019; Baurley et al., 2020.

\* Dataset also comprises ice-marginal lakes in the Tien Shan and Tibetan Plateau.

## 2.2 LACUSTRINE ICE-MARGIN DYNAMICS

### 2.2.1 ICE-MARGINAL LAKE – GLACIER INTERACTIONS

Studies of contemporary lacustrine glacier margins have identified a number of thermo-mechanical controls by which ice-marginal lakes influence ice-margin dynamics. The controls are typically manifest in two outcomes: changes to ice motion and changes to mass loss, which together determine the changing position of the ice-front. Furthermore, the status and evolution of an ice-marginal lake (whether it is forming, subsisting or draining) dictates the nature and magnitude of lake – glacier interactions, and thus the extent to which the lake is able to exert control over ice-margin dynamics. The following section therefore considers lake – glacier interactions under the following scenarios: (i) during lake formation and subsistence; (ii) during lake drainage; and (iii) immediately following lake drainage. Mass

loss at lacustrine margins via frontal ablation processes (calving and subaqueous melt) is discussed separately in the following section.

The presence of water at and below a glacier terminus following ice-marginal lake formation can have considerable implications for ice-margin dynamics, particularly ice motion and buoyancy. The propagation of water beneath an ice-front increases basal water pressure, thereby reducing bed friction and enhancing rates of basal sliding (e.g. Bindschadler, 1983; Anderson et al., 2005; Riesen et al., 2010; Tsutaki et al., 2019; Liu et al. 2020). These effects can be further amplified by the increases in lake depth that are typically associated with lake expansion. For example, Tsutaki et al. (2011) measured year-on-year increases in the terminus velocity of the Rhonegletscher in Switzerland following the formation and progressive expansion of its ice-marginal lake. Positive correlations between ice-marginal lake stage and horizontal ice motion have also been recently recorded at several Alaskan glaciers (e.g. Armstrong and Anderson, 2020; Kienholz et al., 2020). Furthermore, the influence of ice-marginal lakes on ice motion can extend beyond the immediate vicinity of the ice-margin itself. For example, ice-marginal lakes at outlets of the Vatnajökull Ice Cap in Iceland have been observed to impact the longitudinal flow regimes of glaciers for several kilometres up-ice of their respective termini (Storrar et al., 2017; Dell et al., 2019; Baurley et al., 2020). In situations where basal water pressure exceeds the ice overburden pressure, either in response to increased lake depth or downwasting of the ice-margin, two outcomes can prevail. If, under buoyant forces, the bending stresses along the ice-margin are sufficiently accommodated by ice creep, a floating terminus can be sustained (Warren et al., 2001; Tsutaki et al., 2013). For example, the lacustrine terminating Yakutat Glacier in Alaska maintained an extensive floating ice tongue measuring 17.2 km<sup>2</sup> for over a decade before its subsequent collapse in 2010 (Trussel et al., 2013). In addition, the Mendenhall Glacier in Alaska and the Glaciar Upsala in Sweden have also been observed to retain floating termini for several years (Boyce et al., 2007; Naruse and Skvarca, 2000). However, where abrupt increases in buoyant forces exceed the rate of ice creep, fracturing can result in extensive calving across the ice-front, triggering a rapid phase of ice-margin recession (e.g. Boyce et al. 2007). In addition, buoyancy and flotation at ice-margins can enable lakes to reconnect to existing subglacial drainage networks or flow underneath ice-dams, and is therefore one of the primary mechanisms through which ice-marginal lake drainage events are triggered (Tweed and Russell, 1999).

During ice-marginal lake drainage events the abrupt injection of large volumes of water to a glacier bed can regulate the horizontal and vertical motion of ice-margins over relatively short timescales. For example, Anderson et al. (2005) recorded considerable fluctuations in ice-surface displacement during the annual drainage of Hidden Creek Lake in Alaska, where steady increases in ice motion were observed throughout the 12 days prior to the lake drainage event, followed by a rapid acceleration in ice motion coincident with the onset of the lake drainage itself, during which the maximum lateral and vertical glacier displacement corresponded with the peak lake discharge. Upon cessation of the lake drainage event, ice motion immediately fell to below pre-drainage levels, which was inferred to be a response to the collapse of the subglacial drainage network following the abrupt reduction in basal water pressures. Similar observations of short term regulation of glacier motion during ice-marginal lake drainage events have also been observed at the Gornergletscher in Switzerland by both Sugiyama et al. (2008) and Riesen et al. (2010). The enhanced ice motion typically associated with lake drainage events has also been observed to promote calving activity (e.g. Clement, 1984).

The imbalance between outward-directed cryostatic forces and backward-directed hydrostatic forces creates large stress gradients at water-terminating ice-margins (Benn et al., 2007). Consequently, the abrupt reduction in hydrostatic forces, and hence lateral support, at an ice-cliff immediately following ice-marginal lake drainage events can have a considerable impact on the longitudinal stress regime of a glacier, with implications for mass loss and ice motion at a range of timescales. For example, the periodic drainage of a large ice-dammed lake at the margin of Russell Glacier in Greenland has been observed to trigger both extensive ice-front collapse in the hours immediately following lake drainage and, in the ensuing months, the advance of the ice-margin into the former lake basin (Sugden et al., 1985; Russell et al., 2011). Similar advances of an ice-front into a lake basin following ice-marginal lake drainage have also been observed at Mendenhall Glacier in Alaska (Kienholz et al., 2020). However, despite global increases in both the number of ice-marginal lakes and ice-marginal lake drainage events (Carrivick and Tweed, 2019), knowledge of the response of ice-margin dynamics to lake drainage remains confined to a sparse number of observational records.



### 2.2.2 FRONTAL ABLATION

In addition to subaerial ablation, mass loss at water-terminating ice-margins can occur through the processes of subaqueous melt and calving, which together comprise frontal ablation. Isolating the mechanisms and drivers of calving is challenging for several reasons, including: the complexity of the interacting processes at the ice – water interface; the relative sparsity of quantitative datasets of calving activity; and the absence of a standardised system for classifying individual calving events. However, recent advances in discrete element modelling have identified three broad mechanisms associated with calving: ice-cliff failure, undercut calving and buoyancy-driven calving (Åström et al., 2013; Benn et al., 2017). Because the latter two calving mechanisms are closely related to water temperature and water depth respectively, variability in ice-marginal lake properties can have considerable impacts on rates and mechanisms of mass loss at lacustrine ice-margins.

There is notable heterogeneity in existing records of ice-marginal lake water temperatures, with some lakes maintaining relatively low temperatures in the range of 0-3 °C throughout the melt season (e.g. Boyce et al., 2007; Chernos et al., 2016; Carrivick et al., 2017a), and others approaching ~10 °C seasonally (e.g. Minowa et al., 2017; Watson et al., 2020). Because water temperature is a key control on subaqueous melt rates (Truffer and Motyka, 2016), the contribution of subaqueous melt to mass loss is likely to vary considerably between lacustrine terminating ice-margins. However, field records of subaqueous melt rates remain sparse due to the challenge of obtaining direct measurements at calving fronts, and thus the absence of an adequately parameterised melt rate equation for lacustrine termini (Haresign and Warren, 2005). One of the most comprehensive existing studies from a lacustrine ice-margin, at LeConte Glacier in Alaska, concluded that, in the late melt season, the volume of mass lost from the terminus via subaqueous melt approximately equalled that lost through calving (Motyka et al., 2003a). In addition, experimental work by Eijpen et al. (2003) indicated that substantial subaqueous melt rates of up to 0.8 m.day<sup>-1</sup> could be achievable at freshwater ice-margins. Other field studies at lacustrine termini have typically inferred subaqueous melt rates indirectly from lake temperatures and/or observations of ice-margin geometry (e.g. the presence/absence of a projecting ice-foot below the waterline), with several studies concluding subaqueous melt to be a negligible component of ablation (e.g. Boyce et al., 2007; Trussel et al., 2013), and others a key driver of mass loss (e.g. Kirkbride and Warren, 1997; Röhl, 2006; Sugiyama et al., 2016). A more comprehensive understanding of subaqueous melt driven mass loss at lacustrine termini is also hindered by

the relatively limited knowledge of circulation patterns, thermal stratification and meltwater upwelling in ice-marginal lakes, in comparison to the documentation of similar phenomena at marine termini (Truffer and Motyka, 2016).

Subaqueous melt rates are also a key control on the propagation of thermo-erosional notches and undercuts at and below the waterline respectively, and therefore the volume of mass lost through undercut-driven calving events. Few measurements of notch or undercut propagation at lacustrine termini exist due to their inherently hazardous nature. However, Diolaiuti et al. (2006) identified notch formation as a significant control on the calving of the Miage Glacier in Italy during the melt season, with mean notch erosion of  $0.2 \text{ m.day}^{-1}$  and cumulative undercutting of 30-35 m annually. Similar rates of notch erosion have also been identified at the Tasman Glacier in New Zealand (Kirkbride, 1993; Röhl, 2006). In addition to water temperature, Röhl (2006) identified lake circulation, lake stage, ice-cliff geometry and debris supply as controls on rates of thermo-erosional notch propagation.

In addition to melt-undercutting, calving losses at lacustrine termini can occur through buoyancy-driven calving, especially where a lake is deep relative to the thickness of the ice-margin. The onset of buoyancy-driven calving is particularly important because the process typically causes higher rates of mass loss than undercut-driven calving, and is therefore associated with enhanced rates of ice-margin recession (Benn et al., 2007). Buoyancy-driven calving frequently occurs following the retreat of glacier termini into overdeepened lake basins and/or the downwasting of ice-margins (e.g. Kirkbride, 1993; Boyce et al., 2007; Larsen et al., 2015; Baurley et al., 2020). For example, the mean recession rate of the Tasman Glacier in New Zealand increased from  $54 \text{ m.a}^{-1}$  between 2000-2006 to  $144 \text{ m.a}^{-1}$  in 2007-2008 in response to enhanced buoyancy driven calving after the glacier retreated into an overdeepening (Dykes and Brook, 2010). Furthermore, the positive correlation between lake depth and buoyancy-driven calving has formed the basis of several empirical calving laws (e.g. Warren et al., 1995a; Warren and Kirkbride, 2003). Consequently, because greater water depths are typically associated with larger lakes (e.g. Huggel et al., 2002), the contemporary expansion of ice-marginal lakes in many glacierised regions (Section 2.1.2) may increase the prevalence of buoyancy-driven calving at lacustrine termini, and thus accelerate rates of mass loss and terminus recession.

Lacustrine glacier termini typically lose mass at a greater rate than their terrestrial counterparts due to the effects of frontal ablation (van der Veen, 2002). In addition, the presence of ice-marginal lakes often initiates a positive feedback on glacier dynamics whereby enhanced rates of mass loss increase local ice-surface gradients, thus promoting further acceleration, thinning and fracture of the ice-margin, which in turn creates favourable conditions for amplified mass losses through ice-cliff failure and buoyancy-driven calving (Carrivick and Tweed, 2013). This feedback has been used to explain the enhanced rates of ice-margin recession, mass loss and dynamic thinning observed at an increasing number of alpine glaciers following ice-marginal lake formation and expansion (e.g. Naruse and Skvarca, 2000; Boyce et al., 2007; Basnett et al., 2013; Trussel et al., 2013; Brun et al., 2019; King et al., 2019; Tsutaki et al., 2019; Liu et al., 2020). Ice-marginal lake formation at glacier termini is of additional significance because the onset of frontal ablation processes causes the partial decoupling of glacier behaviour from exclusively climatic forcing, with topographic and bathymetric controls increasingly modulating the advance and recession of the ice-margin (Warren, 1991; Kirkbride, 1993; Warren and Rivera, 1994).

Calving rates at lacustrine ice-margins can be up to an order of magnitude lower than those at marine ice-margins (Funk and Rothlisberger, 1989; Warren et al., 1995a; van der Veen, 2002). The disparity between lacustrine and marine calving rates may be a result of lower subaqueous melt rates, and thus melt-undercutting, in lacustrine environments (Truffer and Motyka, 2016). Specifically, subaqueous melt rates are thought to be inhibited by the weak circulation characteristic of ice-marginal lakes that arises from negligible thermal stratification and the limited upwelling of glacial meltwater (Eijpen et al., 2003; Warren et al., 1995a; Truffer and Motyka, 2016). However, in contrast to marine ice-margins, there have been relatively few efforts to quantify spatio-temporal variability in water temperatures, and thus subaqueous melt, at lacustrine ice-margins. In addition, whilst calving mechanisms at marine termini have received considerable attention in recent years, through both observational studies (e.g. Chapuis and Tetzlaff, 2014; Murray et al., 2015; Pętllicki et al., 2015; Ryan et al., 2015; How et al., 2019) and novel modelling approaches (e.g. Benn et al., 2017; Todd et al., 2019), a lack of comparable analyses at lake terminating ice-margins has meant that lacustrine calving mechanisms and their associated drivers remain poorly understood (Trussel et al., 2013; Purdie et al., 2016). The sparsity of empirical data concerning frontal ablation processes therefore remains a significant barrier to improving

knowledge of both calving and subaqueous melt at lacustrine termini, and exploring their disparities with comparable processes at marine termini.

### 2.2.3 SUMMARY

Ice-marginal lakes can exert significant influence over ice-margin dynamics through a range of thermo-mechanical controls and positive feedbacks, which typically enhance rates of mass loss, ice-margin recession and dynamic thinning. However, a sparsity of quantitative data means that several important processes associated with mass loss, such as calving and subaqueous melt, remain poorly constrained at lacustrine ice-margins. Furthermore, existing studies of lacustrine ice-margin dynamics have been predominantly conducted at alpine glacier termini in the mid-latitudes (Table 2.1) and typically provide a snapshot of lake – glacier interactions during the melt season only. Consequently, seasonal variability in lacustrine ice-margin dynamics and the influence of ice-marginal lakes on the dynamics of larger ice masses, such as ice caps and ice sheets, remain poorly understood.

## 2.3 REGIONAL SETTING

### 2.3.1 THE GREENLAND ICE SHEET

With an area of 1.74 M km<sup>2</sup> and a volume of 2.6 M km<sup>3</sup> the Greenland Ice Sheet (GrIS) is the largest mass of ice in the northern hemisphere (Williams and Ferrigno, 2012). The ice sheet is of considerable interest because it is a key indicator of climate change (Bhattacharya et al., 2009) and holds sufficient water to increase mean global sea level by up to 7.4 m (Morlighem et al., 2017). Throughout the second half of the 20<sup>th</sup> century, increased temperatures and runoff at the margins of the ice sheet were offset by increases in precipitation, thus resulting in a period of approximate mass balance (Hanna et al., 2008). However, since the 1990s mass loss from the GrIS has accelerated markedly in response to increased atmospheric and oceanic warming (Hanna et al., 2013), albeit with a reduction in the rate of acceleration between 2013 and 2018 due to increased precipitation and cooler atmospheric conditions (Figure 2.2) (Shepherd et al., 2020). To date, the increased mass loss from the ice sheet has been approximately equally partitioned between processes associated with surface mass balance (primarily runoff and precipitation) and ice-dynamics at the ice-margin (primarily calving and subaqueous melt) (van den Broeke et al., 2009; Khan et al., 2015). The GrIS and its peripheral glaciers and ice caps (PGICs) have therefore progressively increased their contributions to global sea level rise since the 1990s, and are now second only to thermal expansion as the largest contributor (Bamber et al., 2018). Furthermore, continuing mass

loss from the GrIS is projected to cause between 5-33 cm of global sea level rise by 2100 (Aschwanden et al., 2019). Constraining and quantifying ice-margin dynamics in Greenland is therefore of particular importance because one of the greatest sources of the uncertainty associated with current sea level rise projections is dynamical change at ice sheet margins (Church et al., 2013).

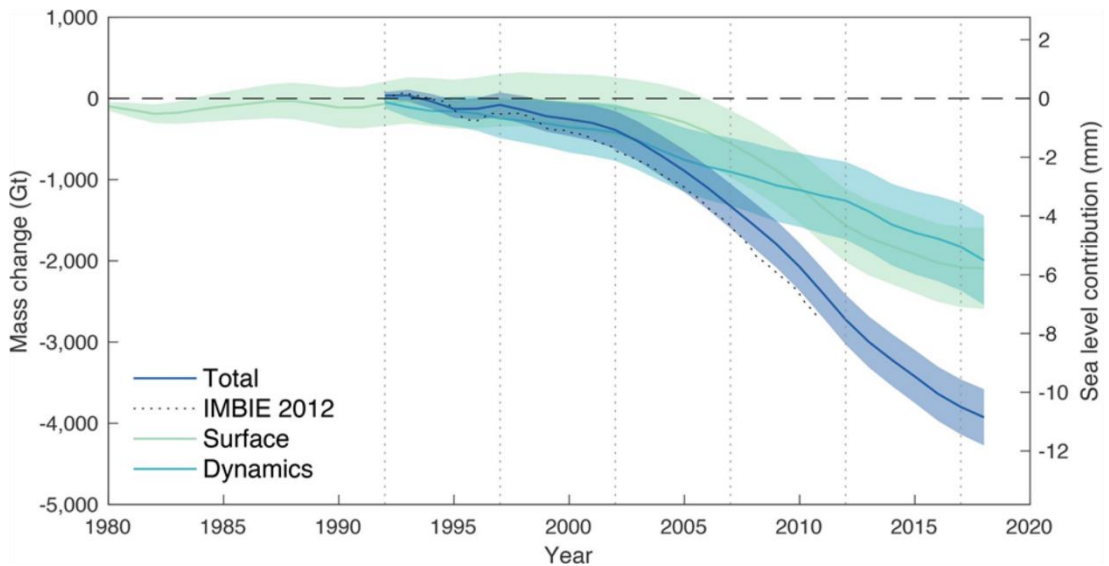


Figure 2.2. Cumulative anomalies in GrIS mass balance and equivalent sea level contribution between 1980 and 2018. Total change (dark blue) can be partitioned into changes associated with surface mass balance (green) and ice dynamics (light blue). Figure from Shepherd et al. (2020).

In common with high mountain environments, ice-marginal lakes are a widespread and increasingly prevalent feature at the margin of the GrIS. Specifically, a Landsat-based analysis of ice-marginal lakes situated along the western margin of the GrIS revealed a net 44% increase in the number of lakes and a net 20% increase in total lake surface area between 1987 and 2010 (Carrivick and Quincey, 2014). The study also noted that the increased variability in lake evolution over the course of the analysis (with many lakes forming, coalescing, draining, or becoming detached from the receding ice-margin) could be indicative of increasing instability in the ice-margin. More recently, a Greenland wide assessment using Sentinel-1 (radar) and Sentinel-2 (optical) imagery identified a total of 3344 ice-marginal lakes at the margins of the GrIS and its PGICs in 2017, with a combined lake area of 3136 km<sup>2</sup> (Mätzler et al., 2019).

In addition to exerting control on local-scale ice-margin dynamics (Section 2.2), the presence of ice-marginal lakes at ice sheet margins has considerable potential to affect regional-scale

ice sheet dynamics via longitudinal coupling. For example, Price et al. (2008) demonstrated that dynamic changes at the margin of the GrIS could propagate dozens of kilometres up-ice, reaching as far inland as the equilibrium line of the ice sheet. However, existing assessments of the impacts of ice-marginal lakes on ice-margin dynamics in Greenland have focused exclusively on the mechanisms of lake drainage events, primarily due to the associated threat posed to downstream hydropower schemes (e.g. Clement, 1984; Higgins, 1970; Mayer and Schuler, 2005). Consequently, a regional-decadal scale analysis of lacustrine ice-margin dynamics has considerable potential to quantify the effects, and thus importance of, ice-marginal lake formation and growth at the margin of the GrIS.

### 2.3.2 RUSSELL GLACIER ICE-DAMMED LAKE

Russell Glacier is a terrestrial outlet of the GrIS, situated in west Greenland approximately 30 km upstream of the head of Søndre Strømfjord and the town of Kangerlussuaq (Figure 2.3). The ice-free region around the glacier comprises sparsely vegetated, rolling gneissic hills reaching approximately 500 m a.s.l. (Hasholt et al., 2013). Following rapid recession from its offshore position at the last glacial maximum, the ice sheet margin in the vicinity of Russell Glacier reached approximately its contemporary extent at ~7,000 cal. yr BP (Carrivick et al. 2018; Lesnek et al., 2020). The proglacial area hosts an extensive geomorphological record of mid- to late-Holocene ice sheet margin activity, including evidence of ice-marginal lake evolution and GLOFs (Carrivick et al., 2017b; 2018). The contemporary local equilibrium line of the ice sheet is ~1500 m a.s.l. (van de Wal et al., 2005; van den Broeke et al., 2008), and the 2012-2019 mean annual air temperature at the PROMICE weather station (KAN\_B) situated ~1 km north of the glacier margin is -4.7 °C (Fausto and van As, 2019). Russell Glacier is one of two outlet glaciers drained by Akuliarusiarsuup Kuua, a primary tributary of the Qinnguata Kuussua (Watson) river (Knight et al., 2000). Meltwater typically begins to flow into Qinnguata Kuussua in April or May, ceasing in September or October (Hasholt et al., 2013).

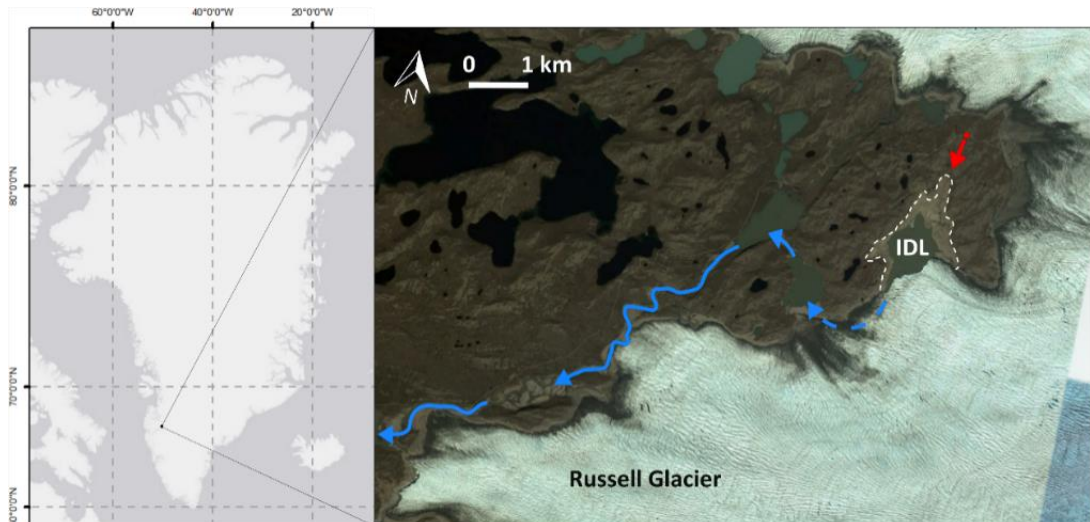


Figure 2.3. Regional setting of Russell Glacier in west Greenland, showing the ice-dammed lake (IDL), and the subglacial (dashed blue line) and subaerial (solid blue line) pathway of outburst floods emanating from sudden lake drainage events. The maximum lake extent is delineated by the dashed white line. The red arrow denotes the position and orientation of the photographs in Figure 2.4. Basemap from Google Earth.

Numerous ice-marginal lakes are situated along the northern margin of Russell Glacier, the largest of which, hereafter referred to as Russell Glacier Ice-Dammed Lake (or IDL), measures  $\sim 1 \text{ km}^2$  and is impounded by a  $\sim 1.5 \text{ km}$  stretch of the glacier margin (Figure 2.3). The volume of the lake can reach  $\sim 40 \text{ M m}^3$ , depending on lake stage and the degree to which the ice-margin encroaches into the lake basin (Russell et al., 2011). The presence of an overflow channel crossing a bedrock col on the western shore of the lake at an altitude of 453.7 m a.s.l. provides a constraint on maximum lake depth. Sedimentary analyses indicate that the Russell Glacier IDL has existed in an ice-marginal form intermittently since  $\sim 4,200 \text{ cal. yr BP}$  (Carrivick et al. 2018). The contemporary lake is particularly notable for quasi-systematic drainage events that generally occur in mid-late summer and last less than 24 hours (Figure 2.4, Table 2.2). Lake drainage is typically initiated by localised flotation of the ice-dam in the southwestern corner of the lake and subsequently sustained by hydraulic jacking and the melt-enlargement of a  $\sim 1 \text{ km}$  long subglacial conduit (Carrivick et al., 2017a). Once the resultant GLOFs have been routed under the ice-dam, they flow subaerially along the northern margin of Russell Glacier for  $\sim 11 \text{ km}$  through a series of outlet lakes and sandurs, before reaching the Qinguata Kuussua river (Figure 2.3). The GLOFs originating from Russell Glacier IDL have been recorded to increase the stage of Qinguata Kuussua in Kangerlussuaq by up to 5.3 m and pose a significant threat to the town's infrastructure and Greenland's principal international airport (Mikkelsen et al., 2013). In addition, the GLOFs have also been recognised as important regulators of both the geomorphology and ecology of the

Kangerlussuaq region due to their role in the transportation and deposition of sediments, organic carbon and nutrients through the Qinguata Kuussua catchment (e.g. Russell, 2007; Anderson et al., 2017).

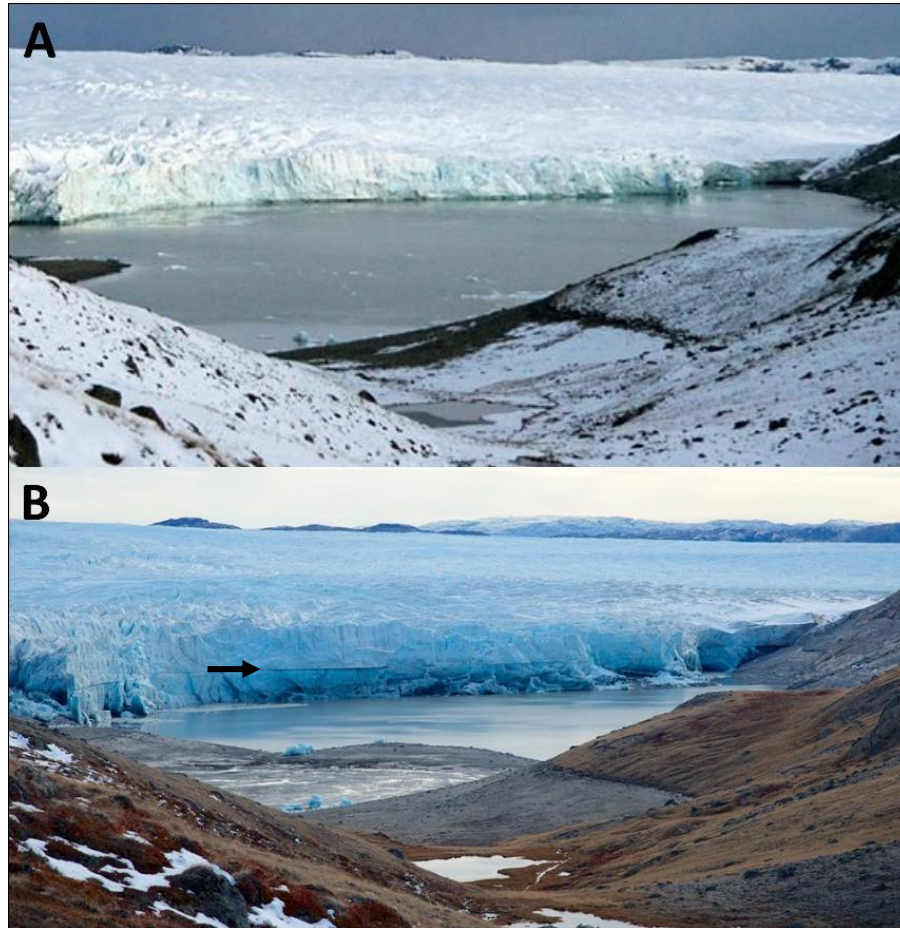


Figure 2.4. Oblique images of Russell Glacier IDL on (a) 14<sup>th</sup> September and (b) 19<sup>th</sup> September 2013, either side of the 15<sup>th</sup> September drainage event. Note in (b) the stranded icebergs and thermo-erosional notch cut at the pre-drainage lake level (denoted by the black arrow). For scale, the freeboard of the ice-cliff following lake drainage is ~60 m. The site and orientation of the photographs is denoted by the red arrow in Figure 2.3. Photographs by Adam Lyberth.

Analysis of changes in downstream channel morphology using photography from sporadic aerial surveys, coupled with intermittent observations of stranded icebergs (cf. Figure 2.4b) and flood debris, has indicated that Russell Glacier IDL drained approximately every 2-3 years between the 1940s and the 1980s (Sugden et al., 1985; Gordon, 1986; Russell, 1989; Russell, 2007). The first directly observed lake drainage event occurred in 1984, however the succeeding event in 1987 marked a temporary halt to the ~50 year drainage cycle. Knight et al. (2000) hypothesised that the lake drainage cycle ceased in response to the wider advance of Russell Glacier between the 1960s and 1990s, causing the ice-margin to advance into the



lake basin to a point where maximum lake depth was insufficient to initiate flotation. The onset of the current drainage cycle in 2007 is therefore a potential response to subsequent ice-margin recession and thinning, thus favouring renewed flotation of the ice-dam (Russell et al., 2011). In addition, lake drainage volumes have progressively decreased since 2010, indicating that the flotation threshold may be reducing in response to ice-surface lowering (Table 2.2) (Carrivick et al., 2017a).

Table 2.2. Dates and available parameters of known Russell Glacier IDL drainage events.

Year	Date	Duration (hours)	Lake level (m a.s.l.)		Lake level change (m)	Lake drainage volume (M m <sup>3</sup> )	References and notes
			Pre-drain	Post-drain			
1984	19th Aug	24	446.7	406.9	39.8	25.2 <sup>1</sup>	Sugden et al., 1985; Russell, 1989
1987	17th July	36	450.8	402.5	48.3	31.3 <sup>1</sup>	Russell, 1989
2007	31st Aug	17	453.7	404.5	49.2	39.1	Russell et al., 2011; Mikkelsen et al., 2013
2008	31st Aug	15	428.3	404.9	23.4	12.9	Russell et al., 2011; Mikkelsen et al., 2013; Carrivick et al., 2013
2010	11th Sept	16	445.7	405.0	40.7	30.7	Mikkelsen et al., 2013; Carrivick et al., 2017a
2011	14th Aug	-	-	-	-	-	Andreas Mikkelsen - pers. comm.
2012	12th Aug	14.5	440.0	405.0	35.0	25.5	Carrivick et al., 2017a
2013	15th Sept	-	-	-	-	-	Adam Lyberth - pers. comm. (see Figure 2.4)
2014	3rd Aug	<41	420.7	405.1	15.6	8.1	This study; Carrivick et al., 2017a
2015	28th July	<44	418.6	405.9	12.7	6.4	This study; Carrivick et al., 2017a
2016	3-12th Sept <sup>2</sup>	-	-	-	-	-	Sentinel-2 & Landsat OLI imagery
2017	27th June-9th July <sup>2</sup>	-	-	-	-	-	Sentinel-2 & Landsat OLI imagery
2018	11th-13th Sept <sup>2</sup>	-	-	-	-	-	Sentinel-2 imagery
2019	3rd-4th Sept <sup>2</sup>	-	-	-	-	-	Sentinel-2 & Landsat OLI imagery

<sup>1</sup> Drainage volumes retrospectively calculated using lake bathymetry from Russell et al. (2011) and lake levels reported in cited papers. <sup>2</sup> Dates constrain the period during which lake drainage event occurred, as derived from comparison of available satellite imagery.

Despite extensive analyses of the lake drainage events originating from Russell Glacier IDL, records of lacustrine ice-margin dynamics at the site are sparse, consisting solely of qualitative descriptions of the ice-margin response to the 1984 and 2007 lake drainage events (Sugden et al., 1985; Russell et al., 2011). Furthermore, there has been no analysis of the impact of sudden lake drainages on ice-margin dynamics regionally, despite increases in the number of both ice-marginal lakes (Carrivick and Quincey, 2014) and ice-marginal lake drainage events (Carrivick and Tweed, 2019) in Greenland. Consequently, the annual drainage cycle of Russell Glacier IDL offers an exceptional opportunity to investigate and quantify the impact of an ice-marginal lake on lacustrine ice-margin dynamics at a local-seasonal scale and across a range of lake volumes.

## Chapter 3

### Methods Overview

#### 3.1 INTRODUCTION

A set of complementary research approaches were devised to investigate the impact of ice-marginal lakes on ice-margin dynamics in west Greenland at multiple spatial and temporal scales. Satellite remote sensing datasets were employed to provide a synoptic perspective of changes at the lacustrine margins of the GrIS on a regional-decadal scale, whereas local-seasonal scale lacustrine ice-margin dynamics were investigated via the installation of a time-lapse camera array at Russell Glacier IDL over the course of three field visits in July 2014, May 2015 and September 2015. This chapter provides a concise rationale for the implementation of both research approaches; specific details of the respective methodologies adopted are provided in chapters 4-6.

#### 3.2 REGIONAL-DECADAL SCALE LACUSTRINE ICE-MARGIN DYNAMICS

Due to the spatial extent of the Greenland and Antarctic ice sheets, satellite remote sensing platforms provide the only viable means for characterising their dynamics at a regional scale. Consequently, as efforts to better constrain the contribution of the major ice sheets to contemporary and projected sea level rise have intensified, recent decades have seen the proliferation of satellite sensors imaging the polar regions at a wide range of spatial, spectral and temporal resolutions (Quincey and Luckman, 2009) (Table 3.1). A variety of optical satellite remote sensing archives were therefore considered for the regional-decadal scale analysis of changes in ice-margin extent along the western margin of the GrIS (Aim 1; Section 1.3). The Landsat image archive was favoured over alternative sensors with finer spatial resolutions, including the Advanced Spaceborne Thermal Emission and Reflection Radiometer (ASTER), Sentinel 2 and the DigitalGlobe satellites, due to the length and uninterrupted nature of its image archive. Specifically, the overlap between the successive Thematic Mapper (TM), Enhanced Thematic Mapper Plus (ETM+) and Operational Land Imager (OLI) sensors afforded the opportunity to quantify changes in ice-margin extent in western Greenland over approximately three decades between the mid-1980s and the mid-2010s (Table 3.1). Extension of the analysis into the 1970s using the Landsat Multispectral Scanner System (MSS) was not pursued due to the comparatively coarse spatial resolution of the sensor and the sparsity of suitable scenes in the image archive in the late 1970s and

early 1980s. In addition, the Landsat archive was preferred over the similarly prolonged Satellite Pour l'Observation de la Terre (SPOT) archive due its wider swath and the open access of the complete image archive.

Table 3.1. Parameters of key optical imaging satellite sensors operating over the Greenland Ice Sheet. Table updated from Quincey and Luckman (2009).

	Sensor	Spatial resolution (m)				Temporal resolution (days)	Scene swath (km)	Archive length	Freely available image archive
		Pan	VNIR	SWIR	TIR/LWIR				
Landsat	MSS	-	79	-	-	16-18	185	1972-1999	✓
	TM	-	30	30	120	16	185	1984-2013	✓
	ETM+	15	30	30	60	16	185	1999-present	✓
	OLI	15	30	30	100	16	185	2013-present	✓
SPOT	1-3	10	20	-	-	1-4	60	1986-2009	✓
	4	10	20	20	-	2-3	60	1998-2013	✓
	5	2.5-5	10	20	-	2-3	60	2002-2015	✓ <sup>1</sup>
	6-7	1.1-1.5	6	-	-	2-3	60	2012-present	✗
DigitalGlobe	Ikonos	0.82-1	3.28-4	-	-	~3	11.3	1999-2015	✓
	Quickbird	0.6	2.4	-	-	1-3.5	18	2001-2014	✗
	GeoEye-1	0.46	1.84	-	-	~3	15.2	2008-present	✗
	WorldView-1	0.5	-	-	-	1.7	17.7	2007-present	✗
	WorldView-2	0.46	1.85	-	-	1.1	16.4	2009-present	✗
	Worldview-3	0.31	1.24	3.74	-	1	13.2	2014-present	✗
	MODIS	-	250-1000	500	1000	1-2	2330	1999-present	✓
	ASTER	-	15	30	90	4-16	60	2000-present <sup>2</sup>	✓
	Sentinel-2	-	10-20	20-60	-	5	290	2015-present	✓

<sup>1</sup> Some imagery freely available if >5 years old. <sup>2</sup> SWIR spectral bands unavailable from 2008.

Classification of ice-marginal lakes and the delineation of the ice sheet margin in west Greenland was achieved using the Normalised Difference Water Index (NDWI) (McFeeters, 1996) and Normalised Difference Snow Index (NDSI) (Hall et al., 1995) band ratio techniques respectively. Both the NDWI and NDSI are widely accepted as robust methods for the corresponding delineation of glacial lakes (e.g. Bolch et al., 2011; Gardelle et al., 2011) and ice-margins (e.g. Silverio and Jaquet, 2005; Andreassen et al., 2008). Furthermore, the adoption of the NDWI facilitated comparison of ice-marginal lake extent with the existing west Greenland lake inventory of Carrivick and Quincey (2014). Although alternative remote sensing techniques are able to yield similar results to band ratio analyses, such as supervised and unsupervised classifications (e.g. Aggarwal et al., 2016), they were discounted due to the notably greater time investment required. Similarly, the adoption of an Object-Based Image Analysis (OBIA) approach can reduce small (pixel-size) ambiguities at glacier and lake margins (e.g. Rastner et al., 2014), but at considerably greater effort for relatively minor

improvements in accuracy. For example, Watson et al. (2016) note that although OBIA approaches can improve the delineation of small (<900 m<sup>2</sup>) supraglacial ponds, the band-ratio analysis of Landsat imagery remains appropriate for the mapping of ice-marginal lakes due to the substantially lower impact of edge effects on larger magnitude water bodies. Further details of the Landsat scene selection and processing are provided in Chapter 4.

### **3.3 LOCAL-SEASONAL SCALE LACUSTRINE ICE-MARGIN DYNAMICS**

Despite their widespread application in the analysis of regional-decadal scale ice-margin dynamics, satellite remote sensing techniques are less suited to the investigation of lacustrine ice-margin dynamics at a local-seasonal scale. Specifically, the inherent trade-off between the spatial resolution and repeat survey frequency of most satellite sensors prevents the acquisition of imagery at the optimal spatial and temporal resolutions to detect small-scale and short-lived lacustrine ice-margin events, such as calving and flotation. Although airborne remote sensing can offer improved spatial resolutions, aerial surveys are typically single or paired measurement campaigns only, and thus more suited to the analysis of infrequent, large-scale and discrete events, such as the calving of tabular icebergs at marine termini (e.g. Ryan et al., 2015; Jouvét et al., 2019), rather than the continuous monitoring of ice-marginal processes. In addition, quantification of volumetric change at ice-margins via the vertical differencing of satellite or airborne derived digital elevation models (DEMs) is unsuited to the investigation of many ice-marginal processes, such as thermo-erosional notch formation, which operate in the horizontal plane normal to the ice-cliff. Consequently, a field-based approach was considered preferable for the investigation of local-seasonal scale ice-margin dynamics at the Russell Glacier IDL field site.

#### **3.3.1 FIELD SURVEYING AND TIME-LAPSE PHOTOGRAPHY**

The aim of acquiring prolonged volumetric records of ice-margin change capable of resolving seasonal variability in lacustrine ice-margin dynamics (Aim 3; Section 1.3) rendered several established field techniques unsuitable at Russell Glacier IDL. For example, the repeat survey of stakes installed on the ice-margin (e.g. Walder et al., 2006; Podrasky et al., 2014) or terrestrial laser scanning (TLS) of the ice-cliff (e.g. Pełlicki et al., 2015; Podgórska et al., 2018) were not viable due to the financial constraints associated with the extended or manifold field seasons necessary for manual data collection. Conversely, although time-lapse photography is a suitable and widely-adopted technique for the extended monitoring of glacier change (e.g. Amundson et al., 2010; Rosenau et al., 2013; Minowa et al., 2018; How

et al., 2019; Vallot et al., 2019), conventional monoscopic (one viewpoint) time-lapse setups were discounted because of their inability to generate volumetric datasets. Furthermore, stereoscopic (two viewpoint) time-lapse setups (e.g. Eiken and Sund, 2012) were also considered unviable, despite their capacity for 3D scene reconstruction, due to their high vulnerability to camera redundancy and a necessity for precise knowledge of camera baselines that would be challenging to accurately establish in a dynamic ice-marginal environment.

### 3.3.2 STRUCTURE-FROM-MOTION AND THE TIME-LAPSE CAMERA ARRAY

Structure-from-Motion (SfM) with Multi-View Stereo (MVS) is a digital photogrammetric and computer vision technique for reconstructing 3D feature geometry from multiple, overlapping digital photographs (Smith et al., 2016a; Eltner et al., 2016). At the outset of research for this thesis in 2012, SfM-MVS was emerging in the geosciences as a novel technique for the completion of rapid, low-cost topographic surveys (e.g. James and Robson, 2012; Westoby et al., 2012) and has since become an established tool for the detection and quantification of geomorphological change (Anderson et al., 2019), particularly in the field of glaciology. For example, recent applications of SfM-MVS in glaciological research include: the measurement of glacier mass balance and surface thinning (e.g. Whitehead et al., 2013; Piermattei et al., 2015; Girod et al., 2018); the derivation of glacier surface velocities (e.g. Immerzeel et al., 2014; Kraaijenbrink et al., 2016; Chudley et al., 2019); the quantification of the aerodynamic roughness of glacier ice (e.g. Smith et al., 2016; Quincey et al., 2017; Chambers et al., 2020); the monitoring and characterisation of dynamic moraine complexes (e.g. Tonkin et al., 2016; Westoby et al., 2016; Bernard et al., 2017); the investigation of discrete marine calving events (e.g. Ryan et al., 2015; Juvet et al., 2019); and the reconstruction of glacier topography from historical image archives (e.g. Mertes et al., 2017; Midgley and Tonkin, 2017; Molg and Bolch, 2017; Girod et al., 2018). However, in conventional applications of SfM-MVS (such as the preceding examples) 3D topographic point clouds are generated from a series of motion-separated photographs that are acquired either by traversing the survey area on foot or through the use of an airborne platform. Consequently, the necessity for manual collection of imagery remains a constraint upon the duration of conventional SfM-MVS surveys and thus the investigation of seasonal variability in glacier dynamics. For the purposes of this research it was therefore hypothesised that the 'motion' between successive images in a typical SfM-MVS survey could instead be simulated by installing a network of identical cameras around the feature of interest and programming

them to acquire imagery concurrently, effectively adopting a multi-sopic time-lapse camera approach, hereafter referred to as the 'time-lapse camera array' (Aim 2; Section 1.3). Despite the considerable potential of such a setup for acquiring extended volumetric records of topographic change, no existing applications of a time-lapse camera array could be identified in the literature. Consequently, a pilot study was designed to assess the viability of such an approach for successfully reconstructing ice-margin topography at Russell Glacier IDL prior to its deployment in the field.

### 3.3.3 MALHAM COVE PILOT STUDY

A considerable diversity of programmable, weatherproof time-lapse camera platforms for environmental monitoring are available on the market for a wide range of budgets. However, the potential for high camera redundancy in Greenland arising from extreme climatic conditions, coupled with improved point cloud quality from larger image sets, favoured a larger camera array populated with affordable cameras, rather than the converse approach. Consequently, an LtL Acorn 5210A 'trail' camera (designed for wildlife photography) was selected for the pilot study due to its relatively high image quality and megapixel count (12 MP extrapolated from 5 MP at acquisition), customisable settings, and affordability. Malham Cove - an 80 m high limestone cliff in North Yorkshire - was selected as an analogue for the ice-margin at Russell Glacier IDL due its similar height, width and prominence over the surrounding topography. The positioning of camera stations in the pilot study was informed by the anticipated semi-circular geometry of the time-lapse camera-array installation at Russell Glacier IDL, which would comprise a network of cameras orientated towards a central point along the lacustrine ice-margin. In such a setup, the presence of the lake would dictate that the majority of cameras were stationed at least 500 m from the focal point of the array (Figure 3.1). Consequently, twelve camera stations falling within 500-1000 m of, but maintaining line-of-sight with, Malham Cove were identified by conducting a viewshed analysis on a DEM of the surrounding area (Figure 3.2). Photographs of the cove were subsequently acquired manually from each of the camera stations over a ~3 hour period using the LtL Acorn 5210A. Additional photographs were acquired concurrently at each site using a 15 MP Sony Nex-5 bridge DSLR camera to provide a baseline for the quality of the point clouds generated from the trail camera imagery.

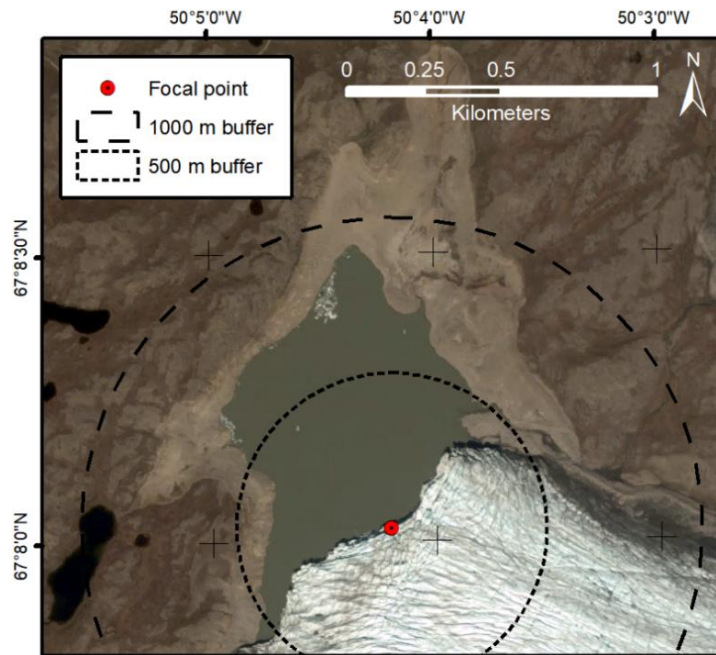


Figure 3.1. Satellite image of Russell Glacier IDL in 2014, illustrating potential sites for trail camera installation between 500 m and 1000 m from the centre of the lacustrine ice-margin. Basemap from Google Earth.

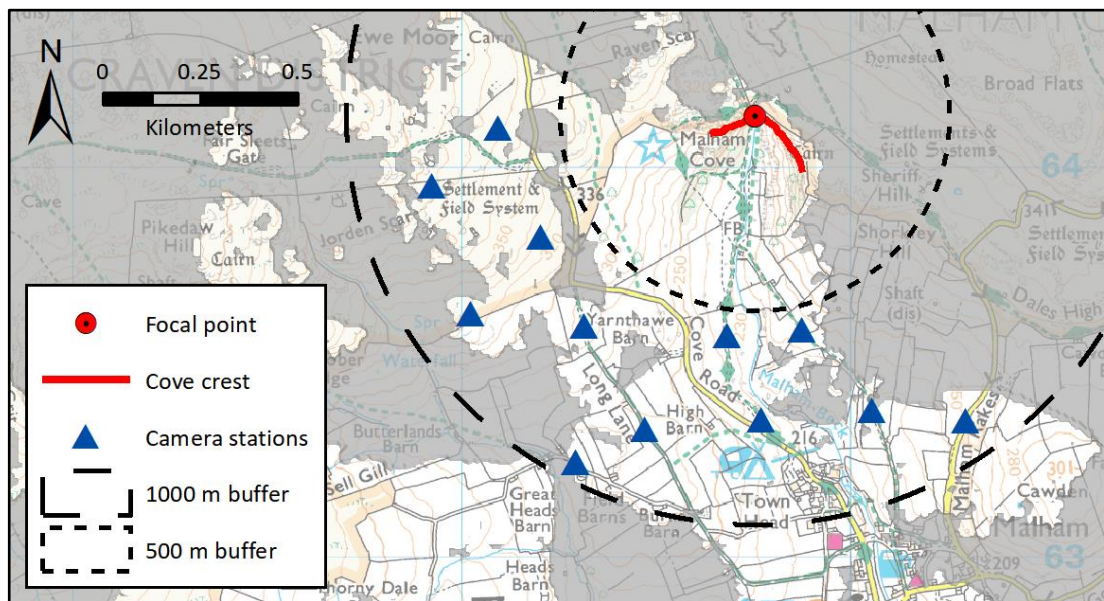


Figure 3.2. Overview of the time-lapse camera-array pilot study at Malham Cove. Grey shading denotes positions with an obscured view of the cove following viewshed analysis. Basemap from Digimap.

Point clouds of Malham Cove’s topography were generated from each image set in Agisoft Photoscan Professional v.1.2.5 using an identical workflow. During the image alignment process only 9 of the 12 trail camera photographs were successfully aligned, in comparison to 11 of the 12 DSLR photographs. However, the spatial coverage of both point clouds remained broadly consistent (Figure 3.3) and the density of the LtL Acorn derived point cloud

(9 pts/m<sup>2</sup>) markedly surpassed that of the DSLR derived point cloud (4 pts/m<sup>2</sup>). Furthermore, although reconstruction of the eastern end and lower altitudes of the cove was limited by dense foliage, both clouds captured small sub-metre topographic features on the main cliff face, including terraces and overhangs. A more detailed comparison of the trail camera and DSLR derived point clouds, including an assessment of point cloud accuracy, was precluded by a lack of high-precision ground control points (GCPs) and an external reference dataset. However, the successful topographic reconstruction of Malham Cove and the favourable point densities of the Ltl 5210A derived point clouds, provided sufficient evidence that a camera array populated with trail cameras would provide a viable platform for the extended acquisition of topographic datasets of the ice-margin at Russell Glacier IDL, and therefore enable the analysis of ice-marginal processes at spatial and temporal scales comparable to those at which they operate. In addition, the successful generation of point clouds, despite the redundancy of some images, indicated that such an approach could be robust to the loss of several cameras within the array. Further evaluation of the time-lapse camera array and its capacity to resolve lacustrine ice-margin dynamics at Russell Glacier IDL is provided in Chapters 5 and 6, alongside detailed summaries of the software and tools employed for point cloud processing and analysis.

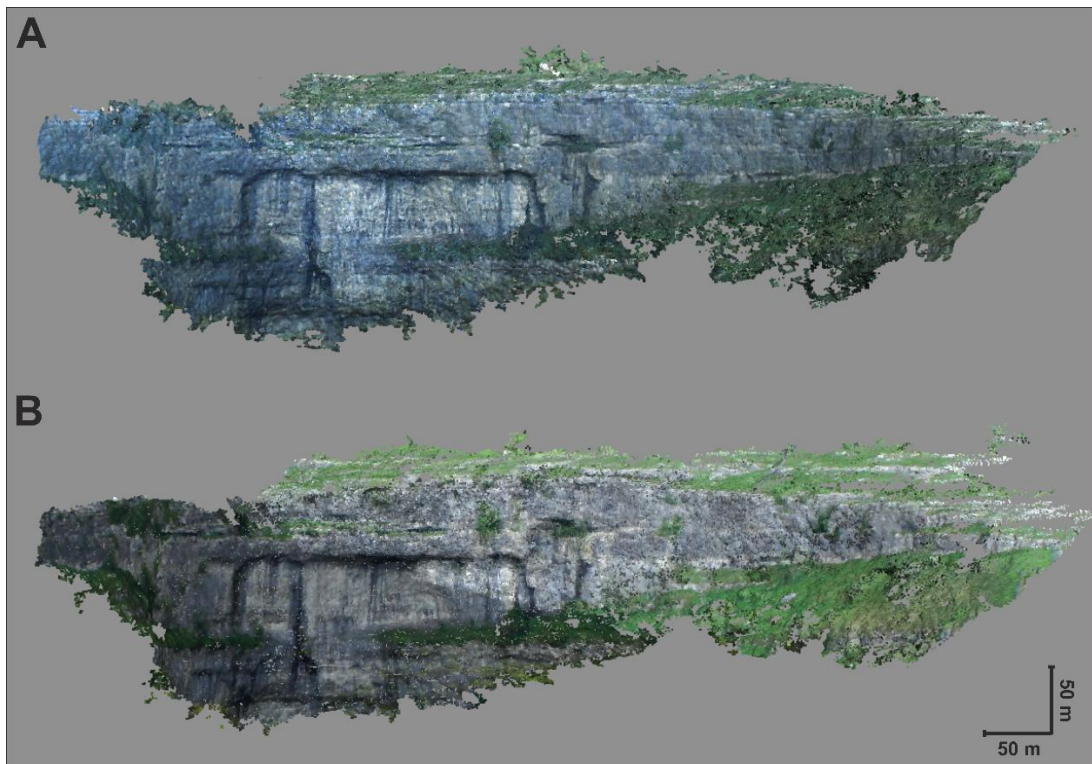


Figure 3.3. Dense point clouds of Malham Cove reconstructed from image sets acquired by (a) the Ltl Acorn 5210A trail camera and (b) the Sony Nex-5 bridge DSLR camera.



### **3.4 SUMMARY**

Having established the viability of the above research approaches for investigating the impact of ice-marginal lakes on ice-margin dynamics in west Greenland at multiple spatial and temporal scales, the following three chapters outline their implementation. Chapter 4 addresses the first aim of the thesis by using the Landsat image archive to perform a regional-decadal scale analysis of changes in ice-margin extent along the western margin of the GrIS. Chapter 5 details the deployment of the time-lapse camera array at Russell Glacier IDL to meet the second aim of the thesis of developing a new methodology for the extended acquisition of fine spatio-temporal resolution datasets of local-seasonal scale ice-margin dynamics. Finally, Chapter 6 presents an analysis of the topographic data acquired by the time-lapse camera array to address the third aim of the thesis of quantifying seasonal variability in calving processes at a lacustrine margin of the GrIS.

## **Chapter 4**

# **A Multi-Decadal Analysis of Lacustrine Ice-Margin Change in West Greenland**

### **AUTHOR CONTRIBUTIONS**

The research presented in this chapter was conceived and designed by Joseph Mallalieu, Jonathan Carrivick and Duncan Quincey. Classification of ice-marginal lakes for the years 1987, 1992, 2000, 2005 and 2010 was performed Duncan Quincey, and for 2015 by Joseph Mallalieu. Delineation of the ice sheet margin and measurements of ice-margin change were completed by Joseph Mallalieu. The statistical analyses were designed and performed by Joseph Mallalieu, with support from Cassandra Raby. The manuscript was written by Joseph Mallalieu, with editorial comments from Jonathan Carrivick and Duncan Quincey.

# **A Multi-Decadal Analysis of Lacustrine Ice-Margin Change in West Greenland**

## **4.1 ABSTRACT**

Enhanced rates of mass loss and meltwater runoff from the Greenland Ice Sheet (GrIS) since the 1990s have coincided with a progressive increase in the number and area of ice-marginal lakes along its western margins. This is of significance because of the capacity of ice-marginal lakes to accelerate mass loss and ice-margin recession through a range of thermo-mechanical controls, including the onset of calving. Such effects have been extensively documented in alpine environments, yet knowledge of how ice-marginal lakes impact ice-margin dynamics in Greenland is limited by a lack of observational data. This study therefore employed the Landsat image archive to conduct a multi-decadal, regional-scale statistical analysis of ice-margin advance and recession along a ~5000 km length of the western margin of the GrIS, incorporating terrestrial, lacustrine and marine ice-margins. The analysis identified an extended and accelerating phase of ice-margin recession in west Greenland from 1992 onwards, irrespective of margin type, but also revealed variability between and within different ice-marginal environments. Although marine margins exhibited the greatest magnitude and variability in ice-margin change, lacustrine termini were notable for a progressive increase in ice-margin recession rates from 1987-2015, which increasingly outpaced those of terrestrial margins. Furthermore, significant relationships were identified between rates of lacustrine margin recession and lake properties, including lake area, latitude, altitude and the length of the lake – ice-margin interface. These results suggest that ice-marginal lakes are becoming increasingly important drivers of mass loss from the GrIS; however further research is necessary to parameterise the causal connections between ice-marginal lake evolution and accelerated ice-margin recession. Overall, a detailed understanding of the influences of ice-marginal lakes on ice-margin dynamics in Greenland is necessary to better constrain the ice sheet's response to ongoing climate change and further refine estimates of sea level rise.

## **4.2 INTRODUCTION**

Since a period of near equilibrium mass balance in the 1980s, rates of mass loss at the Greenland Ice Sheet (GrIS) have generally accelerated in response to increased atmospheric and oceanic warming (Hanna et al., 2013; Shepherd et al., 2020). Over the same time period, enhanced rates of meltwater runoff (Hanna et al., 2008; Trusel et al., 2018) have coincided

with a progressive increase in the number and area of ice-marginal lakes situated along the western margin of the GrIS (Carrivick and Quincey, 2014). The presence of ice-marginal lakes is significant because of their capacity to regulate ice-margin dynamics through a complex range of thermo-mechanical controls, including the onset and promotion of calving (Carrivick and Tweed, 2013). In particular, ice-marginal lake formation and expansion is frequently associated with accelerated rates of mass loss and ice-margin recession (e.g. Kirkbride, 1993; Schomacker, 2010; Basnett et al., 2013; King et al., 2019). Furthermore, on longer timescales, the coalescence of large ice-marginal lakes has been cited as a factor in the rapid collapse of northern hemisphere ice sheets during the last deglaciation (van der Veen, 2002; Stokes and Clark, 2003; Stokes and Clark, 2004; Demidov et al., 2006; Perkins and Brennand, 2015). However, although the effects of ice-marginal lakes on contemporary alpine glacier dynamics have been extensively documented, knowledge of their controls on ice-margin dynamics at the GrIS is limited by a sparsity of data. Consequently, a detailed understanding of the impacts of ice-marginal lakes on ice-margin dynamics in Greenland is increasingly necessary to accurately forecast the response of the ice sheet to ongoing climate change and further refine estimates of sea level rise.

An analysis of GrIS outlet glacier extent by Warren (1991) revealed significant variability in the behaviour of its terrestrial, lacustrine and marine outlets throughout the mid-20<sup>th</sup> century, despite undergoing comparable climatic forcing. Both lacustrine and marine outlets were found to exhibit much greater variability in frontal behaviour than their terrestrial counterparts due to their partial decoupling from climatic forcing and the increased significance of topographic and bathymetric controls on terminus advance and recession. However, subsequent analyses of ice-margin position and character in Greenland have omitted measurements from lacustrine ice-margins, instead focusing on changes at major marine-terminating outlets (e.g. Howat et al., 2008; Howat and Eddy, 2011; Catania et al., 2018), and the terrestrial termini of peripheral glaciers and ice caps (PGICs) (e.g. Citterio et al., 2009; Leclercq et al., 2012; Rastner et al., 2012; Bjork et al., 2018). In addition, the few studies that have incorporated measurements of ice-margin change at terrestrial outlets of the main ice sheet typically include a sparse number of terrestrial data points (e.g. Moon and Joughin, 2008; Carr et al., 2013; Mouginit et al., 2019), or concern a limited footprint in south east Greenland (e.g. Kargel et al., 2012; Mernild et al., 2012). As a consequence, the relative magnitude of recent changes at the lacustrine, terrestrial and marine margins of the GrIS remain unknown.

The long temporal record of the Landsat image archive, now extending into its fourth decade with the launch of Landsat 8 (Roy et al., 2014), provides a unique opportunity to perform a multi-decadal, regional-scale analysis of ice-margin extent for the disparate ice-marginal environments of the GrIS between the 1980s and the present day. Western Greenland is the optimal site for such an analysis because: (i) it has the greatest regional concentration of land-terminating, and thus lacustrine, margins of the GrIS (Figure 4.1); (ii) the region has experienced some of the highest increases in mean annual air temperatures recorded in the Arctic since the 1990s (Carr et al., 2013); and (iii) the region is forecast to undergo some of the greatest rates of ice-margin recession and reductions in ice cover over the next millennium (Aschwanden et al., 2019).

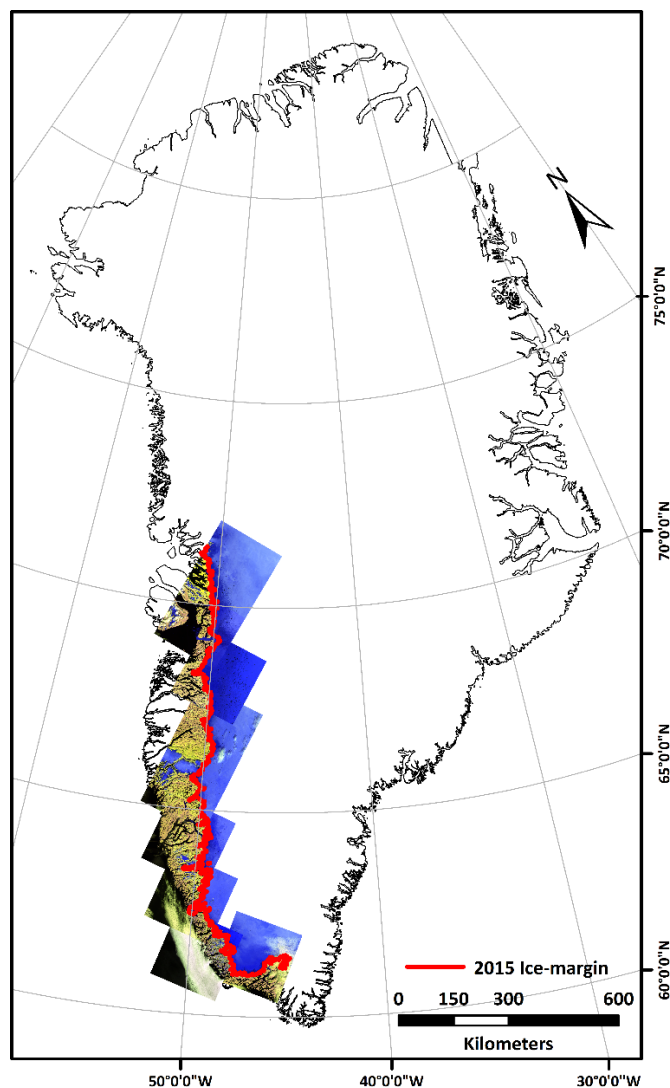


Figure 4.1. Study location in west Greenland. The spatial extent of the analysis is illustrated with false-colour Landsat scenes from 2015 (see Table 4.1).

This study therefore aimed to quantify changes in ice-margin extent at the terrestrial, lacustrine and marine margins of the GrIS in west Greenland between 1987 and 2015, and to investigate how the properties of ice-marginal lakes control rates of ice-margin change. The objectives comprised: (i) the generation of an ice-marginal lake inventory and delineation of the ice sheet margin for 6 epochs at approximately 5-year intervals; (ii) the quantification of ice-margin advance and recession at terrestrial, lacustrine and marine ice-margins between successive epochs; and (iii) a statistical analysis of ice-marginal lake parameters and rates of change at lacustrine ice-margins.

## **4.3 METHODS**

### **4.3.1 LANDSAT SCENE SELECTION**

A total of 58 Landsat Thematic Mapper (TM), Enhanced Thematic Mapper Plus (ETM+) and Operational Land Imager (OLI) scenes were downloaded from the USGS Global Visualisation Viewer to encompass the predominantly terrestrial margins of the GrIS in west Greenland between 1987 and 2015 (Figure 4.1, Table 4.1). All scenes were Level 1TP (radiometrically calibrated and orthorectified) products and possessed a horizontal ground resolution of 30 m. The scenes were selected to coincide with the peak melt season (late June to early September) in order to minimise seasonal variability and reduce the incidence of frozen lakes and snow cover along the ice-margin. Extensive cloud and/or persistent snow cover in some years necessitated a flexible sampling interval for the acquisition of scenes throughout the study period. Consequently, scenes were assigned to one of 6 epochs (1987, 1992, 2000, 2005, 2010 and 2015), with 86% of scenes acquired within  $\pm 1$  year of their respective epoch, and the remaining scenes acquired within  $\pm 2$  years (Table 4.1). Scenes in the 2005 and 2010 epochs were also selected to mitigate the effects of the failed ETM+ Scan Line Corrector (SLC) by utilising the considerable scene overlap within the study area. Where SLC failure induced stripes were unavoidable, gaps were filled via mosaicing with an unaffected scene from the closest viable time period (Figure 4.2a-b). All processing of the Landsat scenes was conducted in ENVI v.5.2 and ArcMap v.10.3.1.

Table 4.1. Attributes of Landsat scenes used in this study.

Epoch	Sensor	Scene ID	Date of acquisition	Path	Row
2015	OLI	LC80010172015227LGN00	15/08/2015	1	17
	OLI	LC80020172015234LGN00	22/08/2015	2	17
	OLI	LC80040172015216LGN00	04/08/2015	4	17
	OLI	LC80050162015255LGN00	12/09/2015	5	16
	OLI	LC80060152015214LGN00	02/08/2015	6	15
	OLI	LC80060162015214LGN01	02/08/2015	6	16
	OLI	LC80070132015237LGN00	25/08/2015	7	13
	OLI	LC80070142015237LGN00	25/08/2015	7	14
	OLI	LC80080122015196LGN00	15/07/2015	8	12
	OLI	LC80100102015210LGN00	29/07/2015	10	10
	OLI	LC80100112015210LGN00	29/07/2015	10	11
2010	ETM+	LE70020172011231EDC00	19/08/2011	2	17
	ETM+	LE70040162009207EDC00	26/07/2009	4	16
	ETM+	LE70040172009207EDC00	26/07/2009	4	17
	ETM+	LE70060152011211ASN00	30/07/2011	6	15
	ETM+	LE70070132010231EDC00	19/08/2010	7	13
	ETM+	LE70070142011234EDC00	22/08/2011	7	14
	ETM+	LE70090112009210EDC00	29/07/2009	9	11
	ETM+	LE70090122010229EDC00	17/08/2010	9	12
	ETM+	LE70100102009217ASN00	05/08/2009	10	10
2005	ETM+	LE70020172004244ASN01	31/08/2004	2	17
	ETM+	LE70040162007202EDC00	21/07/2007	4	16
	ETM+	LE70040172007202EDC00	21/07/2007	4	17
	ETM+	LE70060142007216EDC00	04/08/2007	6	14
	ETM+	LE70060152006245EDC00	02/09/2006	6	15
	ETM+	LE70070132005217EDC00	05/08/2005	7	13
	ETM+	LE70090112007221EDC00	09/08/2007	9	11
	ETM+	LE70090122007221EDC00	09/08/2007	9	12
ETM+	LE70110102005229EDC00	17/08/2005	11	10	
2000	ETM+	LE70020172000217AGS00	04/08/2000	2	17
	ETM+	LE70040161999212EDC01	31/07/1999	4	16
	ETM+	LE70040171999212EDC01	31/07/1999	4	17
	ETM+	LE70060152001215AGS00	03/08/2001	6	15
	ETM+	LE70070132001190EDC00	09/07/2001	7	13
	ETM+	LE70070142001190EDC00	09/07/2001	7	14
	ETM+	LE70090112001188EDC00	07/07/2001	9	11
	ETM+	LE70090122001188EDC00	07/07/2001	9	12
	ETM+	LE70100102000257SGS00	13/09/2000	10	10
ETM+	LE70110102000168EDC00	16/06/2000	11	10	
1992	TM	LT50020171992219PAC00	06/08/1992	2	17
	TM	LT50040161992217PAC00	04/08/1992	4	16
	TM	LT50040171992217PAC00	04/08/1992	4	17
	TM	LT50050161993242PAC00	30/08/1993	5	16
	TM	LT50060141992263PAC00	19/09/1992	6	14
	TM	LT50060151992263PAC00	19/09/1992	6	15
	TM	LT50080121994170KIS00	19/06/1994	8	12
	TM	LT50080131994170PAC00	19/06/1994	8	13
	TM	LT40090111992212XXX02	30/07/1992	9	11
1987	TM	LT50050151987242XXX03	30/08/1987	5	15
	TM	LT50050161987258XXX01	15/09/1987	5	16
	TM	LT50060141987201XXX08	20/07/1987	6	14
	TM	LT50060151987201XXX08	20/07/1987	6	15
	TM	LT50070131987176XXX01	25/06/1987	7	13
	TM	LT40080121988146XXX01	25/05/1988	8	12
	TM	LT50090111985248KIS00	05/09/1985	9	11
	TM	LT40090121988169XXX01	17/06/1988	9	12
	TM	LT50110101987236KIS00	24/08/1987	11	10

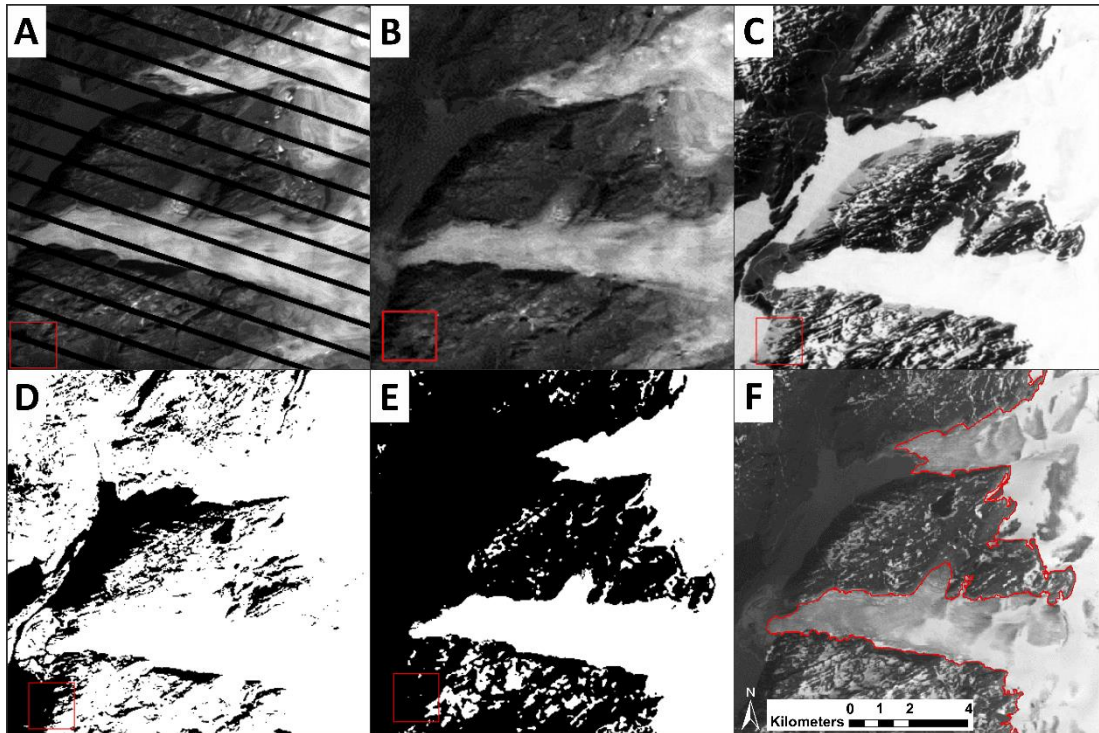


Figure 4.2. Illustration of key stages in ice-margin vector construction: (a) unprocessed Landsat ETM+ band 2 (green) scene affected by SLC failure; (b) mosaiced scene to fill SLC induced gaps; (c) NDSI classification; (d) water mask; (e) application of NDSI threshold and water mask to differentiate snow and ice from land and water; and (f) tidied ice-margin vector.

#### 4.3.2 ICE-MARGINAL LAKE INVENTORY

The ice-marginal lake inventory used in this analysis was derived by refining the 1987-2010 lake dataset mapped in Carrivick and Quincey (2014) and extending the duration of the survey to incorporate Landsat scenes from 2015. Details of the scene processing are fully described and evaluated in Carrivick and Quincey (2014), hence a synopsis is provided here. Scenes were classified by applying the Normalised Difference Water Index (NDWI) (McFeeters, 1996) to the near infrared (NIR) and blue bands of the respective TM, ETM+ and OLI spectral channels, where  $NDWI = ((B_{NIR} - B_{Blue}) / (B_{NIR} + B_{Blue}))$  and  $B$  is the spectral channel. The blue, rather than the more established green, spectral channel was employed because of its improved ability to discriminate water from snow and ice in cold environments (Huggel et al., 2002). An upper NDWI threshold of -0.5 was used to automatically detect lakes and a median filter (3×3 kernel) was used to reduce noise and remove isolated pixels. Classified lakes were exported as vectors for quality assurance in ArcMap, with misclassified areas of cloud and shadow manually corrected through comparison with scenes from adjacent epochs. Manual digitisation was used to delineate several frozen lakes, accounting for ~0.5% of the total lake dataset. The analysis here was subsequently restricted to lakes that: (i)



retained contact with the ice-margin; (ii) were endorheic (with no visible outflow); and (iii) were greater than 25,000 m<sup>2</sup> in area. The ice-contact and endorheic conditions were included to specifically consider the effect of meltwater retention on ice-margin change.

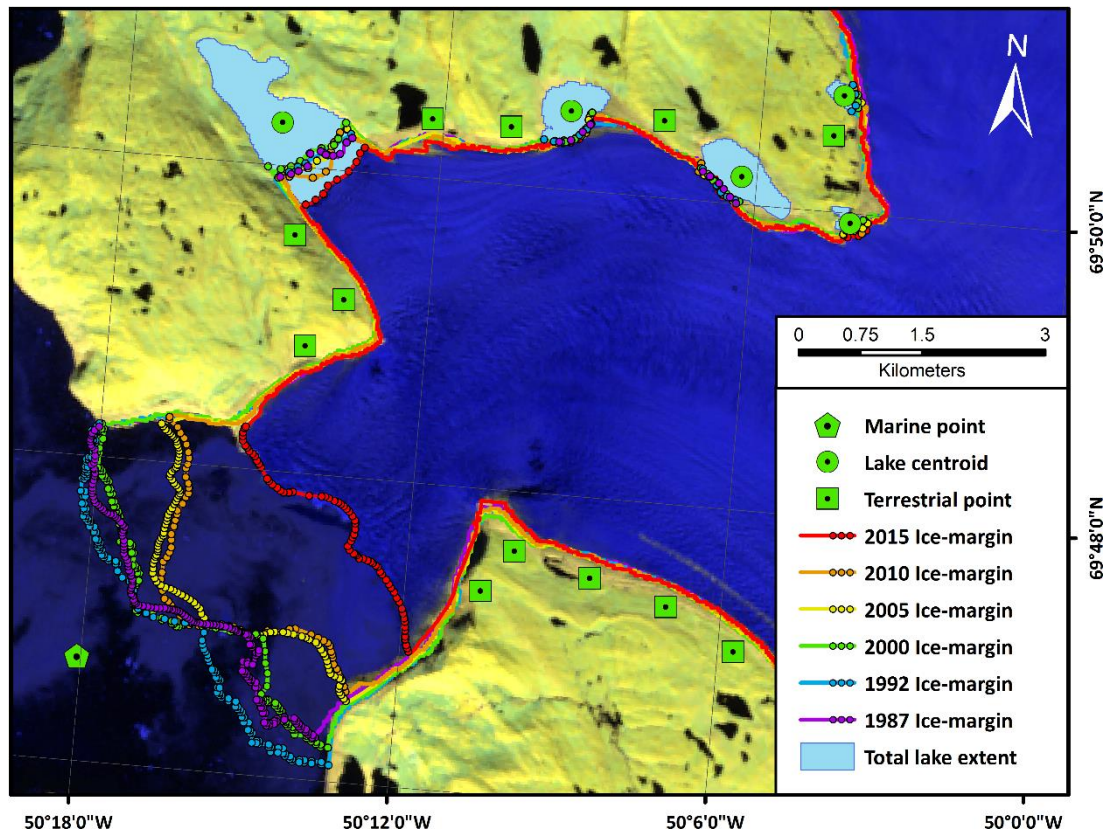


Figure 4.3. Example of dataset, comprising terrestrial, lacustrine and marine ice-margins, and the respective points/centroids used for measurements of ice-margin change. Small circles on marine and lacustrine ice-margins represent the vertices over which distance measurements are averaged. Basemap: 2015 false-colour Landsat OLI scene.

A dataset of lake parameters was established by assigning each lake polygon a consistent identifier throughout the study period by calculating the centroid of the total lake extent (the maximum outline of a given lake across all epochs) (Figure 4.3). The areas of lakes that maintained ice-contact were subsequently calculated within each epoch, but those that lost contact through drainage or ice-margin recession were discounted from the dataset for the respective epoch(s). In the event of a partial lake drainage, only the lake basin that maintained ice-contact was retained in the analysis (e.g. Figure 4.4). In addition, each lake was also assigned a durability score (from 1-6) to indicate its permanence across the 6 epochs. The length of the interface between individual lakes and the ice-margin was measured by using the intersect tool in ArcMap to calculate the geometric intersection of lake polygons and ice-margin vectors to within a tolerance of 30 m (Figure 4.4). Finally, the

latitude and altitude of each lake centroid was extracted from a Digital Elevation Model (DEM) of the GrIS generated from aerial photography acquired in 1985, with a ground resolution of 25 m and horizontal and vertical accuracies of  $\pm 10$  m  $\pm 6$  m respectively (Korsgaard et al., 2016). The delineation of lake extent was assumed to be accurate to within  $\pm 1$  pixel (30 m) of the true lake perimeter. Consequently, the absolute error associated with each area measurement was dependent on lake size and planform, and thus resulted in a declining power law relationship whereby the greatest errors were associated with the smallest lakes. For example, lakes measuring  $0.5 \text{ km}^2$  had an area uncertainty of  $\sim 9\%$ , whilst lakes measuring  $>5 \text{ km}^2$  had an uncertainty of  $<3\%$ .

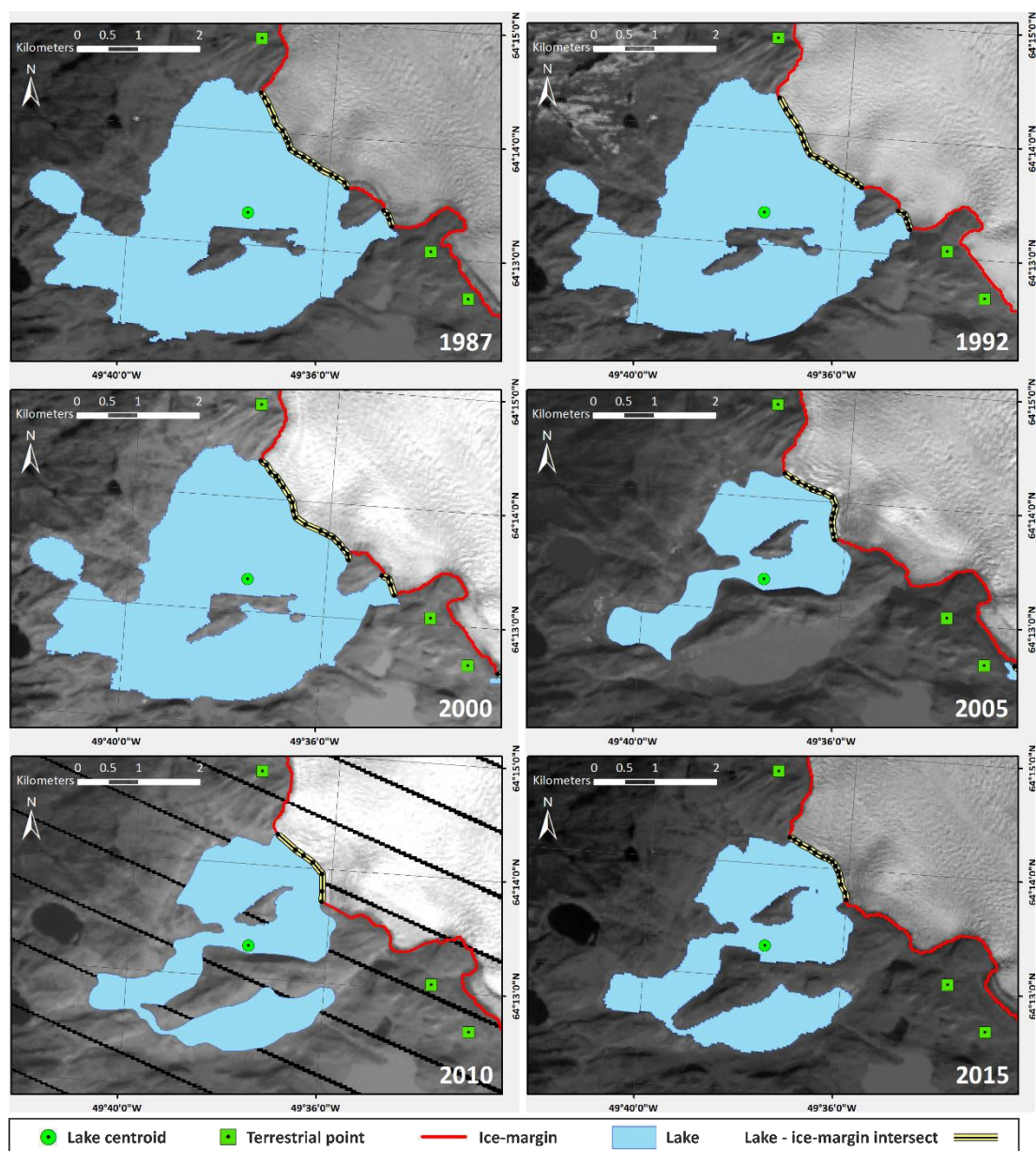


Figure 4.4. Illustration of temporal variation in lake area and lake – ice-margin intersect over the survey period. Note partial lake drainage between 2000-2005, and subsequent refilling.

#### 4.3.3 ICE-MARGIN VECTORS

The GrIS margin was delineated by using the green and shortwave infrared (SWIR) bands of the respective TM, ETM+ and OLI spectral channels to classify scenes using the Normalised Difference Snow Index (NDSI) (Hall et al., 1995), where  $NDSI = ((B_{Green} - B_{SWIR}) / (B_{Green} + B_{SWIR}))$  (Figure 4.2c). An NDSI threshold of  $0.45 \pm 0.1$  was used to classify areas of snow and ice on a scene by scene basis with the aim of minimising the extent of manual post-processing. Due to the similar spectral properties of snow, ice and water in the green and SWIR spectral bands, an additional threshold of 0.45 was applied in the respective NIR band to mask out water bodies in the ice-marginal environment and thus improve the accuracy of ice-margin delineation (Figure 4.2d). Prior to vector conversion, a median filter (3×3 kernel) was applied to reduce noise and remove small snow patches. Manual editing was subsequently employed to tidy the ice-margin vectors in isolated areas affected by shadow, debris cover and late-lying snow. Consistent mapping of the ice-margin was achieved in these regions through consultation with scenes from neighbouring epochs and high resolution DigitalGlobe imagery in Google Earth. Finally, vectors in adjacent scenes were merged to generate a single ice-margin vector for the study region within each epoch (Figures 4.1, 4.4), and subsequently used as the basis for the measurements of ice-margin change detailed in Section 4.3.4. Measurements of total ice-margin vector length, comparable to the length of the lake – ice-margin intersects detailed in Section 4.3.2, were generated by smoothing ice-margin vectors to a tolerance of 30 m using the generalize function in ArcMap. Given that all results presented here are regionally aggregated, it is assumed that any over-estimation of the ice-margin position is cancelled out by an equal and opposite under-estimation, and uncertainty in the ice-margin vector positions is therefore not specifically assessed for these bulk figures.

#### 4.3.4 MEASUREMENTS OF ICE-MARGIN CHANGE

Rates of ice-margin advance and recession between successive epochs were calculated by measuring changes in ice-margin position relative to a series of fixed reference points throughout the study period. Existing techniques for measuring changes in glacier extent have been primarily developed to quantify changes in the position of glacier termini occupying troughs (e.g. Lea et al., 2014), and are thus poorly suited to analysing changes at lacustrine margins which typically occupy a greater diversity of ice-marginal environments, particularly the lateral margins of outlet glaciers (cf. Figure 4.3). For example, techniques that measure change along the centre-line of the glacier (e.g. Bevan et al., 2012; Mernild et al., 2012) are not applicable at the majority of lacustrine margins, and the highly dynamic nature

of many lake – ice-margin interfaces (cf. Figure 4.4) restricts the use of fixed boxes for calculating area averaged advance or recession between successive epochs (e.g. Howat and Eddy, 2011; Hill et al., 2018). Therefore, changes in the extent of lacustrine and marine ice-margins here were measured using the bow method outlined in Bjørk et al. (2012). Lake centroids were used as fixed reference points from which to measure distances to the respective lake – ice-margin intersect within each epoch, with a series of points established on the vertices of each intersect to permit the calculation of a mean centroid – intersect distance (Figure 4.3). Rates of ice-margin advance or recession were then calculated by differencing the mean distance values in successive epochs and dividing by the interval duration. Consequently, rates of change at lacustrine margins were only generated when a lake was present in two or more successive epochs. Changes in the extent of marine margins were measured in the same fashion by establishing fixed marine points in front of each terminus and calculating changes in mean distance between the marine points and respective marine margin vertices in successive epochs (Figure 4.3). Changes at terrestrial margins were calculated by creating a series of fixed points at 1 km intervals along a 250 m buffer of the 1992 ice-margin vector. Distances between the terrestrial points and the ice-margins were measured using the near function in ArcMap and differenced to calculate rates of advance and recession between successive epochs.

#### 4.3.5 STATISTICAL ANALYSES

Data were analysed using multivariate regression methods in R v.3.6.0 (R Core Team, 2019) to: (i) investigate differences in rates of change at lacustrine, terrestrial and marine ice-margins; and (ii) assess the influence of lake parameters on rates of change at lacustrine ice-margins. Two linear mixed-effects models (LMMs) were fitted using the *lme4* package (Bates et al., 2015), with rate of ice-margin change set as the dependent variable in both models. LMMs were the most suitable statistical analyses for the dataset due to the dependent variable being both continuous and unbounded (i.e. both positive and negative), and the need to explore the additive effects of the independent variables on rates of ice-margin change. The LMMs also provided the opportunity to control for the repeated sampling of the same sites across epochs via the inclusion of location as a random effect. One data point from Jakobshavn Isbrae was omitted from the LMMs due to its extreme outlying status (>2 km recession between the 2000 and 2005 epochs). LMM 1 compared rates of change at the disparate margin types, and included: ice-margin type (lacustrine, marine, terrestrial); epoch; and latitude as independent variables, with latitudinal data included to control for

the spatial clustering of particular margin types along the ice-margin. LMM 2 assessed rates of change at lacustrine ice-margins, and included the independent variables: latitude; altitude; lake area; intersect length; durability; and epoch. All independent variables were tested for multicollinearity prior to model fitting; however, lake area and intersect length failed to meet this assumption ( $|r| > 0.7$ ; Dormann et al., 2013). Consequently, two alternate versions of LMM 2 were fitted to accommodate lake area or intersect length.

## 4.4 RESULTS

### 4.4.1 MODEL FIT

Testing of the fitted LMMs for normality and heteroscedasticity revealed that the residuals were heavy-tailed. Because cubed and hyperbolic transformations of the dependent variable were unable to reduce the Akaike Information Criterion (AIC) of the LMMs, additional Robust LMMs were constructed to assess the impact of outliers on model fit using the *robustlmm* package (Koller, 2006). The resultant similarity of the respective LMM and Robust LMM coefficients (Table 4.2) indicated that the outliers had a limited effect on the fit of the models, therefore the outputs of the initial LMMs are presented henceforth.

Table 4.2. LMM and Robust LMM variables and coefficients.

Ind. variables	LMM 1*		Ind. variables	LMM 2(a)		Ind. variables	LMM 2(b)	
	LMM	Robust LMM		LMM	Robust LMM		LMM	Robust LMM
Epoch	-0.120	-0.081	Latitude	0.065	0.051	Latitude	0.068	0.049
Type:Marine	-2.637	-0.612	Altitude	0.132	0.074	Altitude	0.132	0.073
Type:Terrestrial	0.215	0.100	Lake area	-0.191	-0.074	Intersect length	-0.223	-0.095
Latitude	0.020	0.012	Epoch	-0.157	-0.142	Epoch	-0.153	-0.142
			Durability	0.030	0.021	Durability	0.094	0.049

\* NB. Reference values for categorical variables 'Type' in LMM 1 are Lacustrine.

### 4.4.2 ICE-MARGIN CHANGE AT LACUSTRINE, TERRESTRIAL AND MARINE MARGINS

The ice-margin vectors generated in this study delineate a ~5000 km length of the western margin of the GrIS. Cumulative totals of ice-margin type remained broadly consistent between 1987 and 2015, with ~89% of the ice-margin in the study area terminating in a terrestrial setting, ~8% in a lacustrine setting and ~3% in a marine setting (Table 4.3). The number of measurements of ice-margin change between successive epochs was substantial throughout the study period, with each period incorporating measurements from between

22-35 marine margins, 353-439 lacustrine margins and 2469-3325 terrestrial margins (Table 4.4). From 1992 onwards, mean annual change at all margin types was negative, signifying an extended duration of ice-margin recession in western Greenland. However, positive values of mean change between 1987 and 1992 indicate an earlier period of ice-margin advance at both terrestrial and marine margins, although lacustrine margins remained in recession (Table 4.4).

Table 4.3. Summary statistics of ice-margin composition throughout the study period.

Epoch	Total ice-margin length		Terrestrial ice-margin length		Lacustrine ice-margin length		Marine ice-margin length	
	km	% of total	km	% of total	km	% of total	km	% of total
1987	3722*	100.00	3306	88.82	319	8.56	98	2.63
1992	5029	100.00	4500	89.47	398	7.91	132	2.62
2000	5019	100.00	4466	88.98	421	8.38	132	2.64
2005	4916	100.00	4377	89.04	405	8.24	133	2.71
2010	4966	100.00	4429	89.19	402	8.10	135	2.71
2015	4932	100.00	4345	88.10	434	8.80	153	3.10

\* The reduced length of the 1987 ice-margin is due to the unavailability of Landsat TM scenes from the southern end of the study area in the years 1985-1988.

Table 4.4. Summary statistics of ice-margin change throughout the study period.

Period	Terrestrial ice-margins			Lacustrine ice-margins			Marine ice-margins		
	n	Mean change (m)	Annual change (m)	n	Mean change (m)	Annual change (m)	n	Mean change (m)	Annual change (m)
1987-1992	2469	5.8	1.2	353	-5.3	-1.1	22	96.3	19.3
1992-2000	3325	-1.4	-0.2	439	-13.0	-1.6	35	-250.6	-31.3
2000-2005	3325	-24.0	-4.8	414	-28.3	-5.7	35	-640.3	-69.7
2005-2010	3325	-15.3	-3.1	401	-32.2	-6.4	35	-197.6	-39.5
2010-2015	3325	-13.8	-2.8	374	-57.3	-11.5	35	-417.8	-83.6

LMM 1 identified a significant negative trend between rate of ice-margin change and epoch ( $p < 0.001$ ), signifying increasing rates of ice-margin recession in western Greenland between 1987 and 2015, irrespective of margin type (Table 4.5). The model also identified significant differences between rates of change at lacustrine and marine margins ( $p < 0.001$ ), and lacustrine and terrestrial margins ( $p < 0.001$ ) (Table 4.5). Marine margins exhibited both the greatest mean rates of ice-margin recession and the greatest variability in frontal behaviour throughout the study period, with rates of advance and recession at several termini exceeding 100 m per year (Table 4.4, Figure 4.5a). The magnitude and variability of changes

at terrestrial and lacustrine margins were more comparable, although changes at lacustrine margins were less clustered around the median and typically more negative than their terrestrial counterparts (Figure 4.5b, Table 4.4). Notably, although rates of recession increased at both terrestrial and lacustrine ice-margins between 1987 and 2015, recession at lacustrine margins increasingly outpaced that of terrestrial margins towards the end of the study (Figure 4.6).

Table 4.5. LMM results. Significant relationships are highlighted in bold.

LMM No.	Ind. Variables	Estimate	Std. Error	t value	95% Confidence intervals		p value
					lower	upper	
1	(Intercept)	-0.167	0.024	-6.975	-0.214	-0.120	3.52 ×10 <sup>-12</sup>
	<b>Epoch</b>	-0.120	0.007	-17.360	-0.134	-0.107	<b>&lt;2.00 ×10<sup>-16</sup></b>
	<b>Type:Marine*</b>	-2.637	0.088	-29.907	-2.809	-2.464	<b>&lt;2.00 ×10<sup>-16</sup></b>
	<b>Type:Terrestrial*</b>	0.215	0.025	8.466	0.165	0.265	<b>&lt;2.00 ×10<sup>-16</sup></b>
	<b>Latitude</b>	0.020	0.008	2.453	0.004	0.036	<b>0.014</b>
2(a)	(Intercept)	-0.039	0.040	-0.986	-0.117	0.039	0.324
	<b>Latitude</b>	0.065	0.026	2.438	0.013	0.116	<b>0.015</b>
	<b>Altitude</b>	0.132	0.025	5.241	0.083	0.181	<b>1.77 ×10<sup>-7</sup></b>
	<b>Area</b>	-0.191	0.022	-8.687	-0.234	-0.148	<b>&lt;2.00 ×10<sup>-16</sup></b>
	<b>Epoch</b>	-0.157	0.022	-7.215	-0.200	-0.114	<b>7.68 ×10<sup>-13</sup></b>
	Durability	0.030	0.103	0.293	-0.171	0.231	0.770
2(b)	(Intercept)	-0.072	0.040	-1.796	-0.150	0.006	0.073
	<b>Latitude</b>	0.068	0.026	2.576	0.016	0.119	<b>0.010</b>
	<b>Altitude</b>	0.132	0.025	5.299	0.084	0.181	<b>1.30 ×10<sup>-7</sup></b>
	<b>Intersect length</b>	-0.223	0.022	-10.026	-0.267	-0.180	<b>&lt;2.00 ×10<sup>-16</sup></b>
	<b>Epoch</b>	-0.153	0.022	-7.085	-0.196	-0.111	<b>1.92 ×10<sup>-12</sup></b>
	Durability	0.094	0.103	0.917	-0.107	0.295	0.359

\* NB. Reference values for categorical variables 'Type' are Lacustrine.

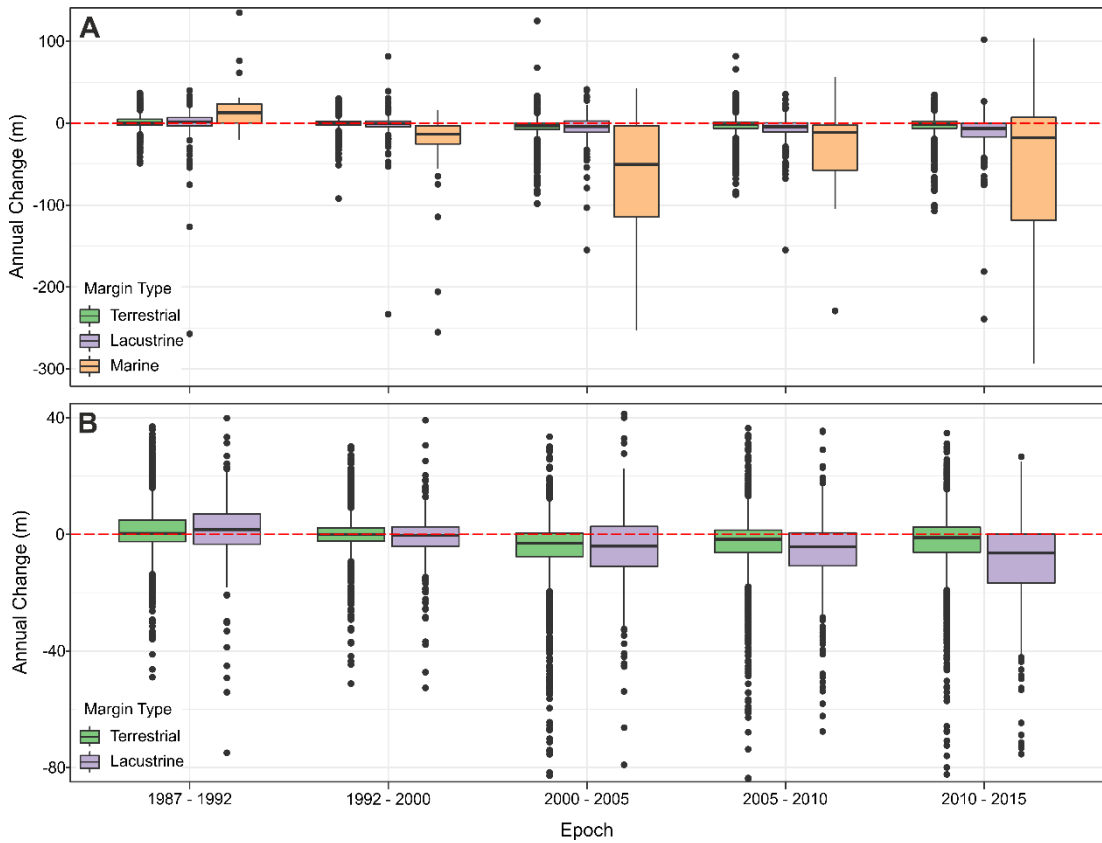


Figure 4.5. Box plots of ice-margin change throughout the study period at: (a) terrestrial, lacustrine and marine margins; and (b) terrestrial and lacustrine margins only. To improve clarity, 7 and 21 outlying data points have been cropped from (a) and (b) respectively.

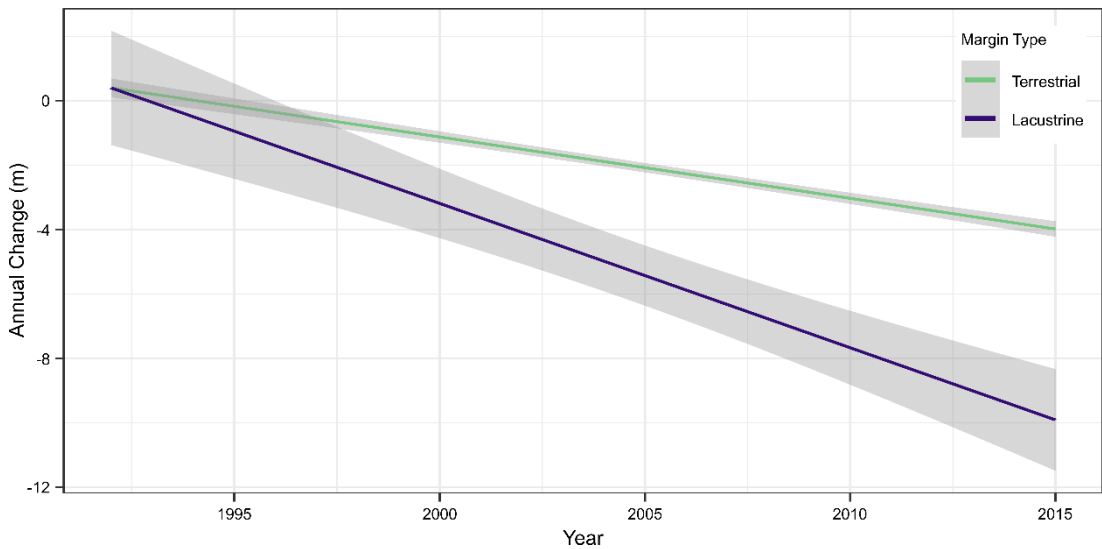


Figure 4.6. Linear regression of annual change and year, showing trends in ice-margin recession at terrestrial and lacustrine margins. The final year of each epoch has been used to plot the linear relationship. Grey shading represents the 95% confidence interval. Individual data points have been removed to improve clarity.



#### 4.4.3 CONTROLS ON LACUSTRINE ICE-MARGIN CHANGE

Both variants of LMM 2 identified a number of significant relationships between lake parameters and rates of change at lacustrine ice-margins (Table 4.5). The significant positive relationship between latitude and rate of change ( $p < 0.05$ ) indicates that ice-margin recession was accentuated at lower latitudes (Figure 4.7a). Altitude was also found to act as a control on ice-margin change ( $p < 0.001$ ), with increased rates of recession at lower altitudes (Figure 4.7b). Both lake area ( $p < 0.001$ ) and intersect length ( $p < 0.001$ ) possessed a similar significant negative relationship with rate of change, demonstrating that increased rates of ice-margin recession are associated with larger lakes and longer lake – ice-margin interfaces (Figures 4.7c, 4.7d). Finally, there was a significant negative relationship between epoch and rate of change ( $p < 0.001$ ), signifying that rates of recession at lacustrine margins increased throughout the duration of the study (Figure 4.7e). No significant relationship was found between durability and rate of ice-margin change.

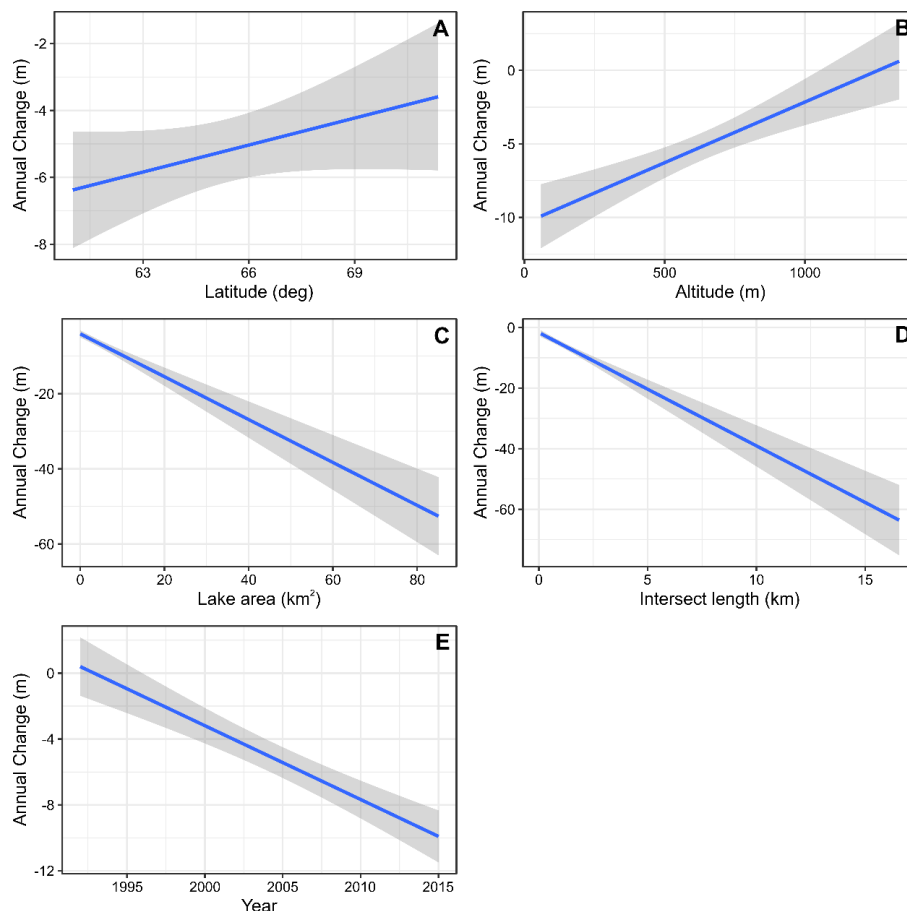


Figure 4.7. Linear regressions of annual change at lacustrine ice-margins and lake parameters, comprising: (a) latitude; (b) altitude; (c) lake area; (d) intersect length; and (e) year. NB. The final year of each epoch has been used to plot the linear relationship in (e). Grey shading represents the 95% confidence interval. Individual data points have been removed to improve clarity.

## 4.5 DISCUSSION

### 4.5.1 ICE-MARGIN CHANGE IN WEST GREENLAND

The temporal patterns of ice-margin advance and recession observed in west Greenland broadly reflect documented changes in ice sheet mass balance over the study period. In particular, the mean advance of terrestrial and marine margins, and concurrent minima of lacustrine margin recession in 1987-1992, coincide with observed advances of outlet glaciers and general ice sheet expansion in the southern and western GrIS during the 1980s (e.g. Weidick, 1991; Zwally, 1989; Van Tatenhove et al., 1995; Knight et al., 2000), following a period of net mass gain in the preceding decade (Mouginot et al., 2019) (Table 4.4). Similarly, the subsequent period of ice-margin recession between 1992-2015 occurs following a transition to net mass loss at the GrIS in the 1980s (Mouginot et al., 2019) and is sustained through a further fivefold increase in the rate of mass loss between the 1990s and 2010 (Shepherd et al., 2020). However, the statistically significant differences between rates of change at the disparate margin types (Tables 4.4, 4.5) and considerable differences in variability of frontal behaviour (Figure 4.5) are indicative of heterogeneous responses at the respective lacustrine, terrestrial and marine margins of the GrIS, despite undergoing comparable climatic forcing over the survey duration.

The relative magnitude and variability of changes at the disparate ice-marginal environments in this study are similar to those observed at the western margins of the GrIS in the mid-20<sup>th</sup> century by Warren (1991), whereby marine margins exhibited the greatest magnitude and variability in frontal behaviour, and terrestrial margins the least. Because terrestrial termini lack oceanic or lacustrine forcing, changes in ice-margin extent are typically a delayed response to regional climatic forcing, with inter-glacier variability arising from glacier-specific factors, including glacier geometry, hypsometry, debris-cover and local climatic conditions (e.g. Pelto and Hedlund, 2001; Scherler et al., 2011; Davies et al., 2012; Sakai and Fujita, 2017; Lovell et al., 2019). Consequently, the relatively limited variability in frontal behaviour at the terrestrial margins, in comparison to the marine margins, of the GrIS is expected (Figure 4.5a), and has been similarly observed in analyses of outlet glacier and PGIC extent in south-eastern Greenland over the same period (Mernild et al., 2012). Furthermore, the low magnitude of the changes observed at terrestrial margins compares favourably with existing records of terrestrial frontal behaviour in western Greenland in the 1990s and 2000s (e.g. Moon and Joughin, 2008; Carr et al., 2013).

In comparison to terrestrial margins, marine termini demonstrated considerably greater magnitude and variability in frontal behaviour over the duration of the study, with a mean annual advance of  $19 \text{ m.a}^{-1}$  in 1987-1992, succeeded by mean annual recessions exceeding  $31 \text{ m.a}^{-1}$  in all remaining periods (Table 4.4). In addition, the mean changes masked considerable complexity in the behaviour of individual marine terminating glaciers, with advances and recessions in the order of 10s and 100s of  $\text{m.a}^{-1}$  respectively becoming increasingly prevalent from 2000-2005 onwards (Figure 4.5a). Isolating the exact drivers of change at marine ice-margins is challenging due to the complexities and interactions of both atmospheric and oceanic forcings, as well as glacier-specific controls including terminus geometry and bathymetry (McFadden et al., 2011; Porter et al., 2018). However, oceanic forcing is increasingly recognised as a key control on the dynamics of the marine outlets of the GrIS (Seale et al., 2011; Straneo and Heimbach, 2013). Accordingly, the observed transition from mean terminus advance to mean terminus recession at marine margins in 1992-2000 coincides with recorded increases in subsurface ocean temperatures along the west coast of Greenland in the mid-1990s (Myers et al., 2007; Holland et al., 2008), which are hypothesised to have triggered both the collapse of several floating termini and the ensuing phase of regional marine ice-margin recession in response to debuttressing (e.g. Joughin et al., 2012). A further increase in marine ice-margin recession observed in this study in the early 2000s also concurs with similar observations over the same time period from marine terminating outlets in south-eastern Greenland (Mernild et al., 2012) and across the wider ice sheet (Moon and Joughin, 2008; Howat and Eddy, 2011).

Despite mean changes in marine ice-margin extent being approximately an order of magnitude greater than those recorded at terrestrial and lacustrine ice-margins between 1987-2015, caution is necessary when interpreting and comparing the frontal behaviour of the disparate ice-marginal environments of the GrIS. In particular, marine ice-margins constitute by far the smallest component of the overall dataset ( $n = 22-35$ ), and also exhibit seasonal variations in terminus advance and recession that are challenging to control for using multi-annual snapshots of terminus position (Schild and Hamilton, 2013). Furthermore, the relatively similar magnitudes of change observed at terrestrial and lacustrine termini distracts from a notable divergence in the behaviour of the respective margin types over the duration of the study. In particular, the persistently negative values of mean changes at lacustrine margins, coupled with a linear increase in their magnitude and their increased outpacing of change at terrestrial margins (Table 4.4, Figure 4.6), could be indicative of

amplified lacustrine forcing and mass loss at the lake terminating margins of the GrIS between 1987 and 2015.

#### 4.5.2 LACUSTRINE ICE-MARGIN RECESSION

The observed dissimilarities in the frontal behaviour of the terrestrial and lake terminating margins of the GrIS over the course of the study can be explained by the impact of lacustrine forcing on ice-margin dynamics. In particular, lake formation has significant implications for processes and rates of mass loss at ice-margins through the onset of both calving (Kirkbride, 1993; Motyka et al., 2003b) and subaqueous melt (Eijpen et al., 2003; Haresign and Warren, 2005; Truffer and Motyka, 2016). Furthermore, ice-marginal lake formation can destabilise and perturb wider ice-margin dynamics through the initiation of a positive feedback whereby enhanced rates of mass loss increase local ice-surface gradients, thus promoting acceleration, thinning and fracture of the ice-margin, which in turn creates favourable conditions for amplified calving losses (Benn et al., 2007; Carrivick and Tweed, 2013). This feedback has been invoked as the cause of the rapid ice-margin recession observed at an increasing number of alpine glaciers (Naruse and Skvarca, 2000; Boyce et al., 2007; Trussell et al., 2013).

The correlations between increased rates of ice-margin recession and greater lake area and intersect length respectively (Figure 4.7c-d, Table 4.5), can be taken to suggest that lake size exerts a control on rates of mass loss at lacustrine margins. Although the augmented rates of ice-margin recession at larger lakes can be hypothesised to arise from the combined effects of calving and subaqueous melt occurring over a greater length of the ice-margin, it is likely that the greater water depths typically associated with larger lakes (e.g. Huggel et al., 2002) are also a key driver of ice-margin recession. In particular, several empirical relationships have linked increased calving rates to greater lake depths (Warren et al., 1995a; Warren and Kirkbride, 2003), whilst accelerated rates of lacustrine ice-margin recession have been observed following the retreat of termini into glacial overdeepenings (e.g. Kirkbride, 1993; Boyce et al., 2007; Larsen et al., 2015; Baurley et al., 2020). In addition, the increased buoyancy and reduced effective pressure apparent at ice-margins terminating in deeper water favour the positive feedback between mass loss and terminus recession outlined previously.

Increases in lake area and depth could also explain the progressive growth in mean annual lacustrine ice-margin recession rates by an order of magnitude throughout the study, from 1.1 m.a<sup>-1</sup> between 1987-1992 to 11.5 m.a<sup>-1</sup> between 2010-2015 (Table 4.4, Figure 4.7e). A behavioural analysis of the lake dataset in Carrivick and Quincey (2014) revealed that ~45% of all ice-marginal lakes in west Greenland formed or increased in size between 1987-2010, in contrast to only ~30% of lakes decreasing in size or draining over the same period. Furthermore, the inverse bed slope along much of the ice sheet margin in western Greenland creates favourable conditions for ongoing lake expansion in response to ice-margin recession (Carrivick et al., 2017b).

An additional cause of enhanced rates of recession at lacustrine ice-margins could be a lengthening of the season over which lacustrine processes, including subaqueous melt and calving, are able to promote mass loss. For example, analyses of non ice-contact lakes in the Arctic have identified an earlier break-up of winter ice cover and increase in ice-free days in response to atmospheric warming over recent decades (Duguay et al., 2006; Smejkalova et al., 2016; Surdu et al., 2016). Similar changes to the ice cover regimes of ice-marginal lakes in western Greenland could therefore have amplified ice-margin recession via the prolonged operation of lacustrine processes associated with higher rates of mass loss, such as melt-undercutting (Mallalieu et al., 2020). Notably, mean annual lacustrine margin recession rates increased following the switch to a negative phase of the North Atlantic Oscillation in the mid-1990s (Table 4.4), which is typically associated with enhanced summertime warming in west Greenland (Hanna et al., 2008; Bevis et al., 2019). In addition, further evidence of climatic control on rates of lacustrine margin recession is also provided by the significant positive correlations between ice-margin change and latitude and altitude respectively (Figure 4.7a-b, Table 4.5), which highlight a strong association between high rates of lacustrine recession and the warmer climatic conditions typically associated with lower latitudes and altitudes. Consequently, the relationships identified here between latitude, altitude and rates of lacustrine margin change, could be considered as tentative indicators of the future response of lacustrine ice-margins to anticipated increases in atmospheric forcing in western Greenland (Bevis et al., 2019).

#### 4.5.3 IMPLICATIONS AND FUTURE RESEARCH

In addition to enhancing local rates of ice-margin recession, the presence of lakes at the margin of the GrIS has profound implications for wider ice sheet dynamics and stability. For

example, Price et al. (2008) demonstrated that dynamic changes at the margins of the GrIS can propagate dozens of kilometres up-ice via longitudinal coupling. Therefore enhanced recession at lacustrine ice-margins and resultant increases in surface gradients have significant potential to amplify surface velocities and promote dynamic thinning up-ice of lacustrine termini of the GrIS, particularly where lakes are large and deep relative to the thickness of the ice-margin. Similar responses to lake formation and growth have been extensively documented in the Himalaya, where lacustrine terminating glaciers account for an increasingly disproportionate share of regional mass loss (Basnett et al., 2013; King et al., 2018; Brun et al., 2019; King et al., 2019). Currently 434 km (~9%) of the ice sheet margin in west Greenland terminates in a lacustrine setting, in contrast to 153 km (~3%) in a marine setting (Table 4.3). However, thinning at the margins of the ice sheet (Krabill et al., 2004; Pritchard et al., 2009), coupled with continued atmospheric warming (Pattyn et al., 2018; Bevis et al., 2019) and the recession of the ice-margin over an inverse bed slope (Carrivick et al., 2017b), will create favourable conditions for enhanced ice-marginal lake formation and growth in west Greenland in coming decades. Consequently, it can be hypothesised that ice-marginal lakes will play an increasingly important role in rates and patterns of deglaciation in Greenland, and that continued lake expansion will amplify future mass loss from the western margin of the GrIS. Furthermore, inadequate consideration of the impacts of lacustrine forcing at the margin of the GrIS could lead to increasing error in projections of the ice sheet's response to climate change, and its contribution to future sea level rise.

A more advanced understanding of the impact of lacustrine forcing on the margin of the GrIS could be developed by focusing future research efforts in three main areas. Firstly, sections of the ice-margin susceptible to lake formation and growth could be determined through the development of morphometric and dynamic criteria, similar to those employed to forecast ice-marginal lake formation in the Himalaya (Reynolds, 2000; Quincey et al., 2007), particularly if integrated with recent high-resolution mapping of GrIS bed topography (e.g. Morlighem et al., 2017). In addition, knowledge of basal topography and ice thickness can facilitate predictions of lake area and depth, which are significant controls on rates of recession at lacustrine ice-margins (Figure 4.7). Secondly, regional-scale analyses of changes in velocity, structure and ice-surface elevation up-ice of the lacustrine termini of the GrIS are necessary to determine the magnitude of the dynamic response of the ice sheet to lake formation and thus refine estimates of mass loss and sea level rise from lacustrine ice-margins. Finally, local-scale analyses of lacustrine ice-margin dynamics are required to

improve knowledge of the mechanisms driving accelerated ice-margin recession. In particular, calving processes and rates of subaqueous melt remain poorly constrained for lacustrine ice-margins, and seasonal variability in these processes remains unquantified.

#### **4.6 CONCLUSIONS**

This study has presented the first systematic analysis of changes in the extent of the terrestrial, lacustrine and marine margins of the GrIS in western Greenland between 1987 and 2015. The analysis has revealed an extended and accelerating phase of ice-margin recession from 1992 onwards, irrespective of ice-margin type. However, statistically significant differences in the rates of ice-margin change have also indicated a divergent response at the respective ice-marginal environments of the GrIS to comparable climatic forcing over the duration of the survey. Marine terminating ice-margins exhibited the greatest magnitude and variability in ice-margin change, with rapid ice-margin recession becoming pervasive after 1992. Although the magnitudes of ice-margin change at terrestrial and lacustrine margins were more comparable, mean annual recession rates at lacustrine margins increased by an order of magnitude over the duration of the survey and increasingly outpaced recession at terrestrial margins. In addition, significant relationships between rates of lacustrine ice-margin recession and several lake properties were also identified, including lake area, latitude, altitude and the length of the lake – ice-margin interface. The progressive increase in rates of lacustrine ice-margin recession over the duration of the study is hypothesised to have arisen from increases in lake size and a lengthening of the season in which calving and subaqueous melt processes can promote mass loss at lacustrine ice-margins. These results suggest that ice-marginal lakes are becoming increasingly important drivers of mass loss from the GrIS and will continue to be so in coming decades in response to enhanced atmospheric warming in western Greenland. Further research is therefore necessary to refine the contribution of mass loss from lacustrine ice-margins of the GrIS to sea level rise projections and better parameterise the causal connections between ice-marginal lake evolution and accelerated ice-margin recession in west Greenland at both a regional and a local scale.

## Chapter 5

### An Integrated Structure-from-Motion and Time-Lapse Technique for Quantifying Ice-Margin Dynamics

#### AUTHOR CONTRIBUTIONS

The work presented in this chapter has appeared in the following publications:

- Mallalieu J., Carrivick J.L., Quincey D.J., Smith M.W. and James W.H.M. 2017. An integrated Structure-from-Motion and time-lapse technique for quantifying ice-margin dynamics. *Journal of Glaciology*. **63**, pp.937-949.
- Mallalieu J., 2016. Case Study: The application of an automated camera array to generate ice-margin feature geometry in west Greenland. In: Carrivick J.L., Smith M.S., and Quincey D.J. eds. *Structure from Motion in the Geosciences*. Chichester, Wiley Blackwell, pp.166-169.

The research presented in this chapter and the above publications was conceived and designed by Mallalieu, Carrivick, Quincey and Smith. Funding for the research was secured by Mallalieu and Quincey. Fieldwork was completed by Mallalieu, Carrivick, Quincey and James. Data processing and analysis was performed by Mallalieu, with support from Smith. The manuscripts were written by Mallalieu with editorial comments from Carrivick, Quincey and Smith.



# **An Integrated Structure-from-Motion and Time-Lapse Technique for Quantifying Ice-Margin Dynamics**

## **5.1 ABSTRACT**

Fine resolution topographic data derived from methods such as Structure-from-Motion (SfM) and Multi-View Stereo (MVS) have the potential to provide detailed observations of geomorphological change, but have thus far been limited by the logistical constraints of conducting repeat surveys in the field. This study therefore presented the results from an automated time-lapse camera array, deployed around an ice-marginal lake on the western margin of the Greenland Ice Sheet. Fifteen cameras acquired imagery three-times per day over a 426 day period, yielding a dataset of approximately 19,000 images. From these data, eighteen point clouds of the ice-margin were derived across a range of seasons and used to successfully detect calving events (ranging from 234 to 1,475 m<sup>2</sup> in area and 815 to 8,725 m<sup>3</sup> in volume), induced by ice-cliff undercutting at the waterline and the collapse of spalling flakes. Low ambient light levels, locally reflective surfaces and the large survey range hindered the analysis of smaller scale ice-margin dynamics. Nevertheless, this research demonstrates that an integrated SfM-MVS and time-lapse approach can be employed to generate long-term 3D topographic datasets and thus quantify ice-margin dynamics at a fine spatio-temporal scale. This approach provides a template for future studies of geomorphological change.

## **5.2 INTRODUCTION**

The number and area of ice-marginal lakes are increasing globally in response to contemporary deglaciation (Carrivick and Tweed, 2013). Ice-marginal lakes can influence the dynamics of glaciers via a series of thermo-mechanical controls, including: enhanced basal water pressure, buoyancy and sliding (e.g. Anderson et al., 2005; Riesen et al., 2010; Tsutaki et al., 2011); terminus flotation (e.g. Naruse and Skvarca, 2000; Mayer et al., 2008; Tsutaki et al., 2013); and perhaps most importantly, the initiation of calving (Warren et al., 2001; van der Veen, 2002). Their development often leads to the formation of a positive feedback whereby ice-margin recession promotes lake expansion, which further accelerates glacier mass loss (e.g. Kirkbride, 1993; Warren et al., 1995a; Boyce et al., 2007; Trussel et al., 2013). However, the effects of ice-marginal lakes on glacier dynamics remain poorly understood and tend to be omitted from mechanistic models of glacier change and sea level rise because of a scarcity of quantitative field data from calving ice-margins (Benn et al., 2007).

Existing satellite and airborne remote sensing approaches are generally unable to capture the high spatio-temporal variability of physical changes at lacustrine ice-margins. Satellite-based techniques have been used extensively to study ice-margin dynamics, structure and extent (Quincey and Luckman, 2009), but the trade-off between spatial resolution and frequency of repeat survey can prevent the acquisition of imagery at the optimal spatial and temporal scales for the investigation of ice-marginal processes. Airborne remote sensing can provide imagery at much finer spatial, spectral and temporal resolutions (Abdalati et al., 2001), but the expense of repeat overflights often precludes acquiring a dense dataset of observations. Similarly, many field-based techniques encounter spatial and temporal limitations. For example, repeat optical or dGPS surveys of stakes installed on glacier termini are commonly employed to measure changes in ice-margin extent, elevation and velocity (e.g. Anderson et al., 2005; Sugiyama et al., 2007; Tsutaki et al., 2011). However, such surveys necessarily possess a coarse spatial resolution and may only be resurveyed weekly or seasonally. Where frequent (i.e. sub-daily) resurveys of stakes have been reported these surveys are rarely sustained beyond several weeks (e.g. Walder et al., 2006; Podrasky et al., 2014). In addition, the spatial coverage of physical surveys at ice-margins is often restricted by zones of deep crevassing and extensive calving activity.

Ground-based remote sensing techniques provide an alternative approach for the collection of high-resolution topographic data from inaccessible and dangerous locations. Most notably, the advent of terrestrial laser scanning (TLS) has enabled the rapid generation of high-accuracy topographic datasets, with fine (sub-metre) spatial resolution, broad spatial coverage and sub-daily temporal capability. Recent applications of TLS in glaciology include the monitoring of glacier surface melt (Gabbud et al., 2015), mass balance (Fischer et al., 2016), thermo-erosional notch propagation (Pętllicki et al., 2015), and the quantification of aerodynamic surface roughness (Smith et al., 2016b). However, the necessity for manual on-site operation of TLS limits its suitability for capturing ice-marginal lake – glacier interactions, particularly calving activity (the timing of which is largely unpredictable), or for generating fine temporal resolution datasets of ice-margin dynamics across an entire season. Besides the considerable expense of the equipment and its associated software, the application of TLS in ice-marginal environments is further constrained by significant reductions in point density and point accuracy caused by poor laser reflection within near-infrared wavelengths from wet or melting surfaces (e.g. Deems et al., 2013; Gabbud et al., 2015; Pętllicki et al., 2015).

In recent years advances in Structure-from-Motion (SfM) and Multi-View Stereo (MVS) techniques have enabled the generation of topographic datasets with spatial resolutions and accuracies comparable to, and in many cases surpassing, those generated via traditional photogrammetry, ground-based TLS and airborne Light Detection and Ranging (LiDAR) (Westoby et al., 2012; Fonstad et al., 2013; Smith et al., 2016a). Key advantages of the SfM-MVS approach are its affordability, fast data processing times and ease of data acquisition – requiring only a consumer grade digital camera or mobile phone (Micheletti et al., 2015). SfM-MVS techniques have recently been used to measure seasonal changes in glacier dynamics (e.g. Whitehead et al., 2013; Immerzeel et al., 2014) and to investigate discrete marine calving events (Ryan et al., 2015). However, in common with TLS surveys, glacial SfM-MVS based studies are limited by the logistical constraints of collecting repeat surveys in the field and thus typically comprise week-long to month-long datasets at best. Furthermore, the infrequent acquisition of data can increase the superimposition and coalescence of geomorphological events (e.g. Abellán et al., 2014) and is therefore a major obstacle to identifying and isolating mechanistic drivers and triggers of geomorphological change.

Time-lapse photography has been extensively employed in glaciology to generate long-term (seasonal – annual) datasets of glacier change (e.g. Amundson et al., 2010; Danielson and Sharp, 2013; Murray et al., 2015; Pełlicki et al., 2015) and can facilitate the acquisition of imagery at fine-temporal resolutions. Consequently, the integration of SfM-MVS and time-lapse techniques has remarkable potential for generating long-term 3D topographic datasets, and hence revealing mechanistic drivers and triggers of geomorphological change. However, to date a combined approach remains relatively unexplored, in part due to the perceived difficulties of establishing and maintaining an automated camera network capable of acquiring the necessary image datasets (e.g. Eltner et al., 2016).

This study therefore aimed to demonstrate how an integrated SfM-MVS and time-lapse approach could be employed to acquire and analyse fine spatio-temporal resolution datasets of ice-margin dynamics. The technique was deployed at a dynamic lacustrine-terminating margin of the Greenland Ice Sheet (GrIS) to assess its viability in a hostile and challenging environment.

### 5.3 STUDY SITE

The study focused on an ice-marginal lake (67°08'10" N, 50°04'25" W) adjacent to the northern margin of Russell Glacier, which is a predominantly land-terminating outlet glacier in western Greenland (Figure 5.1). The ~1 km<sup>2</sup> lake, hereafter referred to as Russell Glacier Ice-Dammed Lake (or IDL), is impounded by a 1.5 km long ice-dam, and is notable for a series of well-documented drainage events in the summer months (e.g. Sugden et al., 1985; Russell, 1989; Mernild and Hasholt, 2009; Russell et al., 2011; Mikkelsen et al., 2013). The freeboard of the ice-margin ranges from 10 m to 60 m depending on the elevation of the lake surface. Analysis of satellite radar interferometry indicates ice-surface velocities in the vicinity of the ice-dammed lake are ~30 m.a<sup>-1</sup> (Rignot and Mouginot, 2012), while field surveys of basal ice velocities along the northern margin of Russell Glacier are in the range of 20 m.a<sup>-1</sup> to 43 m.a<sup>-1</sup> (Chandler et al., 2005).

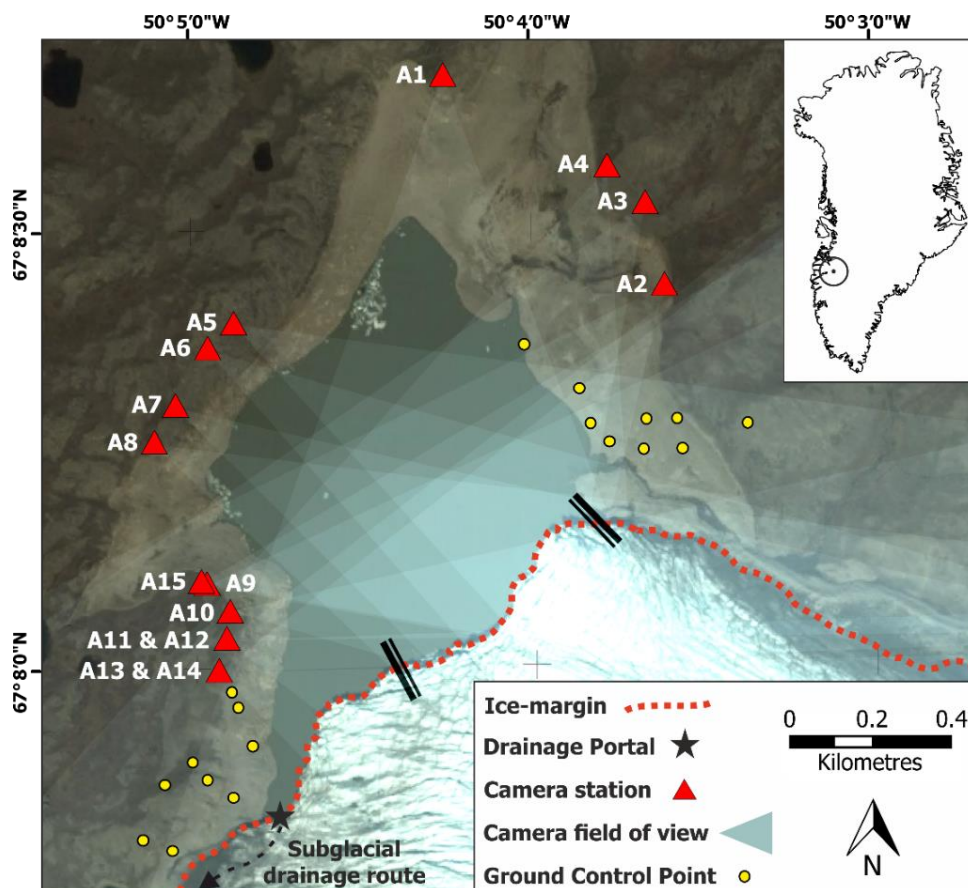


Figure 5.1. Study location on the northern margin of Russell Glacier, western Greenland (inset) and camera array geometry. Heavier blue shading represents increased camera overlap.

## 5.4 METHODS

SfM-MVS employs digital photogrammetric and computer vision methods to simultaneously resolve camera position and three-dimensional feature geometry using multiple digital photos as the primary input (Snavely et al., 2006; Fonstad et al., 2013). The output of the technique is a point cloud, comprising identifiable features from the image dataset, which can be scaled and georeferenced using ground control points (GCPs) situated within the survey area or by using measurements of camera positions during image acquisition. Comprehensive reviews of the underlying principles of SfM-MVS, and its recent applications in geographical research are presented in Smith et al. (2016a), Eltner et al. (2016) and Carrivick et al. (2016). Typically, image acquisition for SfM-MVS is performed manually using a single camera carried around the survey reach on foot or mounted to an airborne platform (e.g. unmanned aerial vehicle, kite, gyrocopter). Consequently, the scheduling and duration of field seasons acts as an arbitrary constraint on image acquisition and therefore data collection. Additionally, James and Robson (2014a) noted that single camera SfM-MVS image acquisition is impractical for capturing rapid, dynamic events, where high rates of change instead necessitate continuous, simultaneous image collection from multiple cameras.

### 5.4.1 TIME-LAPSE CAMERA ARRAY SETUP

In an effort to extend the duration of image acquisition indefinitely an automated time-lapse 'camera array' was devised and subsequently installed at Russell Glacier IDL. The aim of the array was to develop an autonomous, affordable and low-maintenance technique for prolonged high-frequency SfM-MVS image acquisition, capable of withstanding the extremes of the Greenland climate. The array was populated with fifteen LtL Acorn 5210A 12 MP (interpolated from 5 MP) trail cameras with a 6 mm focal length and 52° angle of view. The camera model was selected for its programmability, high image quality, multiple power sources, and – given the high number of cameras required – affordability (costing ~£120 each). Power was supplied internally using 8 disposable lithium AA batteries, which were favoured because of their low self-discharge and capacity to remain operative in temperatures as low as -40 °C. Photovoltaic cells were discounted as a power source due to the minimal midwinter daylight at 67° north and the high likelihood of burial by snow. Fluctuations in ambient lighting conditions and shadows during conventional SfM-MVS surveys can interfere with the keypoint matching stage of the SfM process (James and Robson, 2012; Bemis et al., 2014). Consequently, camera clocks were synchronised manually to an external handheld GPS receiver and programmed to trigger simultaneously at 09:00,

13:00 and 17:00 hours daily. The timing of image acquisition was designed to minimise battery use (thereby extending the operational longevity of the camera array) and make optimal use of the available daylight during the winter months.

The camera array was installed along the shore of Russell Glacier IDL in the summer of 2014, with a range of orthogonal (side looking) and oblique (front looking) viewpoints employed to maximise coverage of the ice-margin and mitigate the ‘doming’ effect associated with near parallel view orientations (James and Robson, 2014b) (Figure 5.1). The positions of some cameras were adjusted in response to quality control of the setup, which was performed in the field by downloading the preliminary imagery to a laptop running SfM-MVS software and generating test point clouds. A more even distribution of cameras around the lake was not possible because the orientation and dip of local topography diminished viewsheds of the ice-margin along sections of the shore. However, each camera was individually orientated towards the ice-margin so that its field of view possessed at least 30% overlap with that of another camera. The average viewing distance of the cameras to the active ice-front was 765 m (Table 5.1). In contrast to other static camera installations this setup did not use tripods, camera mounts or enclosures to stabilise or protect the cameras (cf. Rivera et al., 2012; Danielson and Sharp, 2013; Rosenau et al., 2013). Instead the cameras were stationed on the ground and buttressed laterally and overhead with boulders to minimise movement and offer protection from the weather and wildlife (Figure 5.2). The camera array operated continuously for a total of 426 days, extending from 27 July 2014 to 24 September 2015. The only maintenance performed during the operating period occurred between 22-23 May 2015 and comprised the download of existing imagery, replacement of batteries and the reset of one camera which had been dislodged from its station.



Figure 5.2. Example of a trail camera installation at the lake shore.

Table 5.1. Survey range between the cameras and ice-margin.

Camera No.	Distance to proximal ice-front (m)	Distance to distal ice-front (m)	Mean distance (m)
A1	984	1,321	1,153
A2	523	1,073	798
A3	687	1,197	942
A4	755	1,229	992
A5	800	897	849
A6	782	924	853
A7	720	948	834
A8	690	974	832
A9	410	858	634
A10	338	819	579
A11	320	842	581
A12	320	842	581
A13	318	879	599
A14	318	879	599
A15	422	868	645
Mean	559	970	765

#### 5.4.2 GROUND CONTROL POINTS

A network of eighteen GCPs, consisting of stable landscape features (e.g. large boulders, exposed bedrock bluffs) located immediately either side of the ice-margin was surveyed using a Leica System 500 dGPS in July 2014 to enable georeferencing of the point clouds derived from the image dataset. The position of a temporary base station mounted approximately 5 km from the lake was obtained by post-processing 10 hours of observations recorded at 1 minute intervals against the Kellyville International Geodetic System network continuous receiver, yielding a 3D accuracy of  $\pm 0.01$  m. GCPs around the lake margin were then surveyed in real-time static mode (using the geometric mean of 120 static readings) and post-processed against the base-station, yielding an overall 3D accuracy of  $\pm 0.05$  m. Owing to the dynamic nature of the field site GCPs could not be located on the ice-margin itself, and dynamic lighting conditions dictated that in many surveys only a subset of GCPs could be identified in the camera imagery.

#### 5.4.3 POINT CLOUD PROCESSING

Following recovery of the cameras in September 2015 the image dataset was used to generate point clouds of ice-margin topography using the commercial software Agisoft Photoscan Professional v.1.2.5 (available from [www.agisoft.com](http://www.agisoft.com)), with further analysis

performed in the open source software CloudCompare v.2.7 (CloudCompare 2016). Owing to the limited GCP coverage across the ice-front, pre-calibration of camera parameters was undertaken using a calibrated target. Focal length, principal point and three radial distortion parameters were included in the final camera model. Camera calibration parameters and imagery were imported into Agisoft Photoscan where the lake and sky were masked from the remaining workflow prior to the running of bundle adjustment algorithms to construct the sparse point clouds. Reprojection filters were then applied to remove the ~10% of points with the lowest localisation accuracies (as determined by the least squares minimisation of errors within the bundle adjustment process). Reconstruction uncertainty filters were also used to identify noise in the clouds induced by the relatively small baselines between some neighbouring cameras, resulting in a further ~10% of points being removed. The sparse clouds were then scaled and georeferenced by importing GCP coordinates and marking visible GCPs in the camera imagery, before running MVS algorithms to generate the final dense point clouds. In this application, GCPs were used only to scale and georeference the cloud and were not used to refine camera models and determine cloud shape (so-called 'optimization' within Agisoft Photoscan).

To demonstrate the potential of the approach, eighteen point clouds were chosen to reflect different seasons (and thus weather and ambient lighting conditions), GCP distributions (which were also largely a function of illumination) and periods of ice-front activity and inactivity (Table 5.2). Initial analysis of the point clouds indicated significant daily variability in point cloud parameters, particularly point cloud density and GCP visibility. Point clouds derived from 13:00 images were selected for all subsequent analyses as they returned both high point densities and high GCP visibility. Image sets were paired and categorised as being 'active' i.e. some change in ice-front morphology was observed, and 'inactive' i.e. no change in morphology was observed. Distances between cloud pairs were subsequently computed in CloudCompare using the multi-scale model-to-model cloud comparison (M3C2) algorithm developed by Lague et al. (2013). The M3C2 tool was used to determine surface normals along the ice-front and subsequently calculate distances between core points subsampled from the input clouds. Normal and projection scales of 40 m and 6 m respectively were applied to minimise the influence of local surface roughness along the ice-front (which produced highly complex normals at lower scales) whilst maintaining the efficiency of the calculation. Provisional differencing of the inactive point cloud pairs revealed significant regions of change in peripheral survey areas, notably the stable lake shores (Figure 5.3).



Analysis of the camera array geometry indicated that the observed changes corresponded with low camera overlap (Figure 5.4); consequently, all point clouds were trimmed to the sector of ice-front possessing greatest camera coverage prior to further analysis.

Table 5.2. Seasonal variations in point cloud parameters.

	Date (DOY)	Time	No. of aligned cameras	No. of GCPs visible in image dataset	No. of points in cloud	Mean point density (pts/m <sup>2</sup> )	Geo-referencing RMSE (m)	Weather conditions
Daily variation	25 July 2014 (206)	09:00	15	17	602,899	14	12.2	Sunny, no cloud cover
	25 July 2014 (206)	13:00	15	17	678,246	18	9.3	Sunny, no cloud cover
	25 July 2014 (206)	17:00	15	13	712,023	20	6.1	Sunny, no cloud cover
Inactive point cloud pairs	25 July 2014 (206)	13:00	15	17	678,246	18	9.3	Sunny, no cloud cover
	26 July 2014 (207)	13:00	15	17	676,861	18	6.7	Sunny, light cloud cover
	19 Dec. 2014 (353)	13:00	12	6	657,324	18	7.3	Medium cloud cover, very low ambient light
	20 Dec. 2014 (356)	13:00	12	6	664,275	18	8	Heavy cloud cover, very low ambient light
	6 May 2015 (126)	13:00	14	9	830,870	15	18.2	Sunny, no cloud cover, some haze
	7 May 2015 (127)	13:00	14	9	848,910	17	18.7	Sunny, no cloud cover
	29 Aug. 2015 (241)	13:00	14	13	765,333	21	5.5	Heavy cloud cover
	30 Aug. 2015 (242)	13:00	14	13	781,817	21	5.7	Heavy cloud cover
	20 Aug. 2014 (232)	13:00	14	12	833,345	19	2.5	Heavy cloud cover
	21 Aug. 2014 (233)	13:00	14	12	866,157	19	2.5	Heavy cloud cover
Active point cloud pairs	19 Feb. 2015 (50)	13:00	11	6	771,630	21	2.8	Light cloud cover, low ambient light
	20 Feb. 2015 (51)	13:00	11	6	763,057	24	3.4	Light cloud cover, low ambient light
	12 June 2015 (163)	13:00	15	16	861,816	19	10.7	Sunny, light cloud cover
	13 June 2015 (164)	13:00	15	16	871,928	20	9.9	Sunny, no cloud cover
	10 Aug. 2015 (222)	13:00	15	13	838,136	20	5.6	Heavy cloud cover
	11 Aug. 2015 (223)	13:00	15	13	832,414	21	5.6	Heavy cloud cover
Mean values			14	12	769,836	19	7.8	

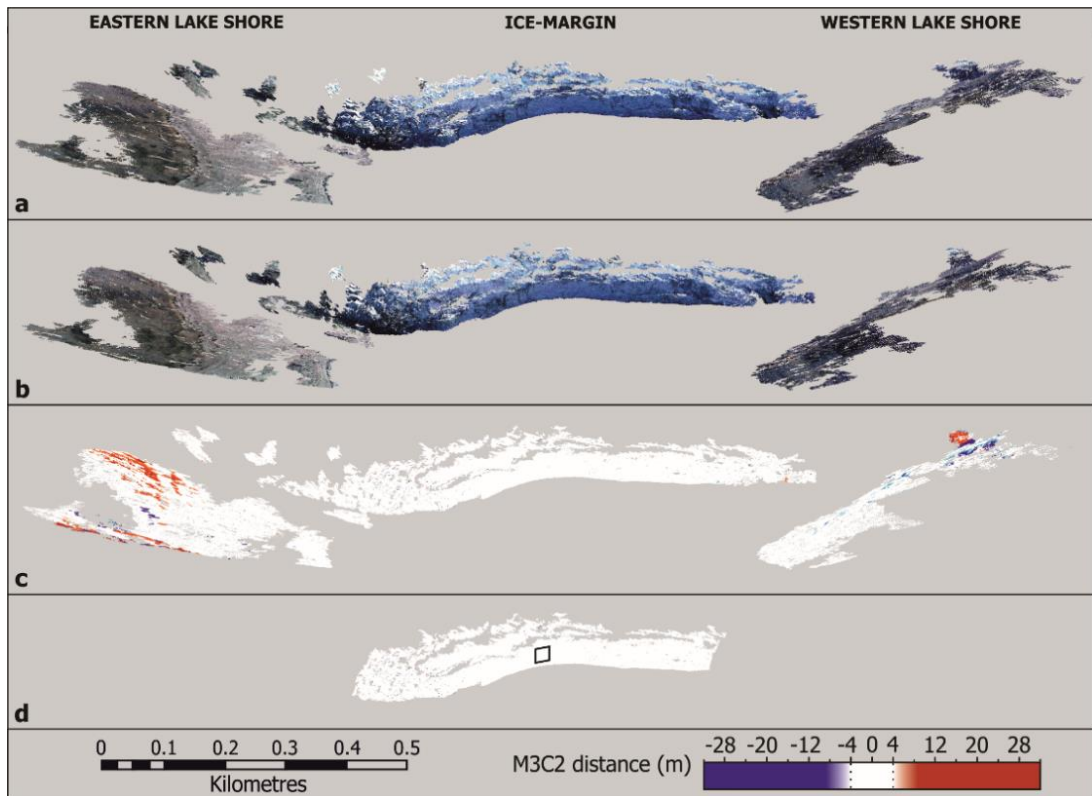


Figure 5.3. Schematic of point cloud differencing workflow: (a & b) Point clouds from 13:00 on 25 and 26 July 2014 respectively; (c) the resultant output of the M3C2 cloud differencing algorithm; and (d) the M3C2 output trimmed to the sector of ice-front possessing greatest camera coverage (note the black square denotes the location of 30 m<sup>2</sup> patch). The differencing of inactive cloud pairs provides a measure of internal consistency in cloud geometry. The changes detected on the stable lake shores are indicative of poor camera coverage in peripheral survey areas.

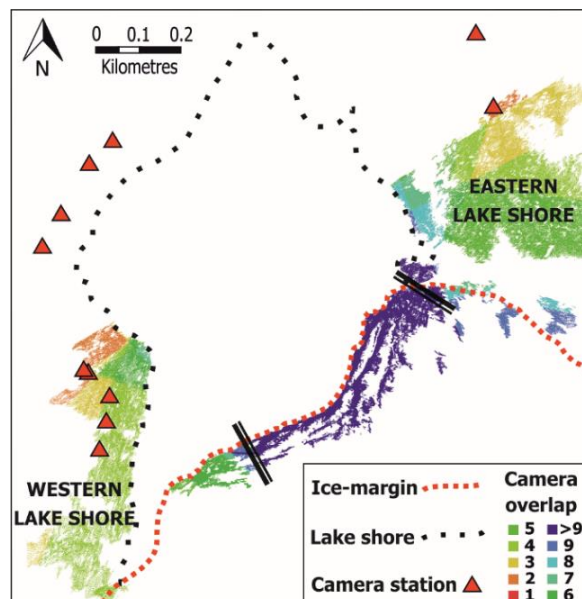


Figure 5.4. Aerial view of dense point cloud derived from imagery acquired at 13:00 on 25 July 2014, illustrating the spatial extent of cloud reconstruction and camera overlap. Black bars delineate the trimmed section of ice-margin used for analysis.

The real-world accuracy of point clouds is conventionally measured against an independently derived reference dataset. However, an assessment of cloud accuracy is not a necessity for this technique, because differences between clouds can still be measured provided there is internal consistency in cloud geometry. To provide an assessment of cloud consistency the means and standard deviations of distances between inactive point cloud pairs were measured along the trimmed ice-margin (Figure 5.3d). Analysis of the data showed that in the worst case scenario 95% ( $\pm 2$  standard deviations) of distances between inactive point cloud pairs were within 3.72 m of the mean recorded change (Table 5.3). Consequently, a threshold of 4 m was adopted to distinguish statistically significant changes from noise when differencing the active point cloud pairs. This cautious approach is commensurate with the scale of change that this SfM survey is designed to detect, as even relatively minor lacustrine calving events are typically tens to hundreds of cubic metres in volume. Further standard deviation measurements were taken from a 30 m<sup>2</sup> patch in the centre of the ice-front (Figure 5.3d), revealing that a detection threshold of  $\sim 2$  m could be viable for the sections of the point cloud with greatest camera coverage (Table 5.3). The 2.5D Volume tool in CloudCompare was subsequently used to calculate the volumes of any changes lying beyond the respective 2 m and 4 m error thresholds. Volumes were computed by cropping the respective cloud pairs to the region of change, orienting them to an arbitrary plane and projecting a grid (with a cell size of 1 m<sup>2</sup>) through a rasterised copy of the cropped clouds.

Table 5.3. Standard deviations and mean changes for inactive point cloud pairs.

Cloud dates	Entire ice-margin			Central 30 m <sup>2</sup> patch		
	Mean change (m)	SD of change	4 * SD	Mean change (m)	SD of change	4 * SD
25-26 July 2014	-0.19	0.89	3.56	0.57	0.36	1.44
19-20 December 2014	-0.38	0.93	3.72	-0.69	0.51	2.04
6-7 May 2015	0.13	0.72	2.88	-0.16	0.50	2.00
29-30 August 2015	-0.38	0.74	2.96	-0.29	0.31	1.24

## 5.5 RESULTS

### 5.5.1 CAMERA ARRAY VIABILITY AND POINT CLOUD CONSTRUCTION

Analysis of the image dataset illustrates the capacity of the automated camera array setup for capturing long-term (>annual) records of ice-margin change. The cameras recorded  $\sim 19,000$  images of the ice-margin over a 426 day period and remained fully operative despite repeated burial by snow and local temperatures reaching  $-33$  °C in February 2015. The cameras remained in position for the duration of the study, with the exception of camera A2

which was dislodged from its position in the late summer of both 2014 and 2015, most likely by wildlife. Relatively minor drifts in camera orientation were also observed over the study period in response to freezing and thawing ground ice. The availability of cameras and GCPs for point cloud generation fluctuated in the winter months in response to snowfall (Table 5.2). Cameras were able to continue capturing viable imagery in the aftermath of moderate snowfall (<10 cm depth), though light snowfalls were often sufficient to prevent the identification of GCPs in the camera imagery. To a lesser extent some GCPs were also obscured in the spring and summer months by vegetation growth immediately in the foreground of some camera stations.

The construction of ice-margin point clouds was viable at least once per day for 93.5% (398 days) of the study period, with burial by snow or poor weather conditions (including mist, rain and snowfall) obscuring the ice-margin on the remaining days. The longest period with no viable images for point cloud generation occurred between 23-29 of December 2014. The relatively small number of images employed in the SfM-MVS analysis expedited data processing, with ~2.5 hours required to complete the Agisoft Photoscan workflow for each point cloud (using 8 GB of RAM and an Intel i5 quad-core processor operating at 3.2 GHz). The most time consuming stage of the workflow was the manual identification of GCPs in the camera imagery, without which dense point cloud construction would have been possible on a sub-hour timescale. The spatial extent of the generated point clouds comprised the majority of the lacustrine ice-margin and terrain immediately adjacent to the eastern and western lake shores (Figures 5.4, 5.5). Reconstruction of the westernmost section of the lacustrine ice-margin was prohibited by poor camera coverage, which may explain the relatively high georeferencing errors given that GCPs were also located at the edges of the survey area (Table 5.2). Generation of the ice-surface topography was limited by extensive crevassing along the ice-margin (Figures 5.3, 5.5).

#### 5.5.2 POINT CLOUD PARAMETERS

Point cloud parameters exhibited notable variance throughout the study, with the number of points in each ice-front ranging from ~600,000 to ~870,000 and ice-front point densities falling between 14 to 24 points per m<sup>2</sup> (Table 5.2). Ambient lighting, weather conditions and the elevation of the lake surface all acted as controls on point cloud size and density. Smaller point clouds, with lower point densities were generally associated with low ambient light availability (particularly in midwinter) or elevated lake levels thereby minimising the

subaerial portion of the ice-margin. Larger point clouds and point densities were generally associated with brighter conditions and/or low lake levels. The impact of ambient light levels on point cloud alignment was investigated by superimposing successive point clouds sharing identical processing parameters and weather conditions, and with no visible changes in ice-front position or morphology. Overlaying all three clouds from 25 July 2014 revealed close alignment between the 13:00 and 17:00 clouds (mean change 0.48 m), however the 09:00 cloud was misaligned with the 13:00 and 17:00 clouds by a mean distance of -5.71 and -5.15 m respectively. The sole difference in the image datasets used to derive the three clouds was the illumination of the ice-margin, which was in full sun at 17:00, partially shaded at 13:00 and both heavily shaded and exhibiting strong glare from the lake surface at 09:00 (cf. imagery in Figure 5.6a). Analysis of the feature matches detected during sparse point cloud construction demonstrated that poor illumination of the ice-margin corresponded with fewer accepted feature matches (Figure 5.6). Additionally, contrasting weather conditions (and thus light levels) were also observed to cause poor alignment between point cloud pairs. Consequently, measurements of ice-margin change via point cloud differencing were limited to point cloud pairs exhibiting consistent weather conditions and ambient lighting.

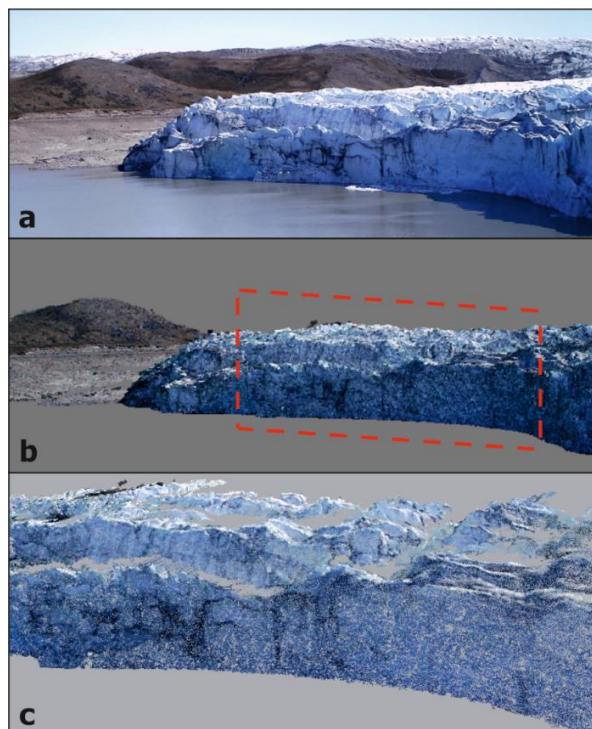


Figure 5.5. (a) Cropped image of ice-margin recorded at 13:00 on 25 July 2014 from camera A12; (b) corresponding view of the derived dense-point cloud; (c) enlargement of area bounded by dashed line in panel b, with detail illustrating the effect of crevasse peaks on point cloud reconstruction of the ice sheet surface. Note for scale the vertical height of the ice-margin is  $\sim 50$  m.

In the absence of an independently derived reference dataset, analysis of the georeferencing root-mean-square error (RMSE) (the error metric generated by the scaling and georeferencing of a point cloud) can be used as an approximate gauge of model quality. Table 5.2 illustrates that georeferencing RMSEs varied substantially across the study, with values for individual point clouds ranging from 2.5 to 18.7 m. The data show no significant relationship between georeferencing RMSE and the number of aligned cameras, or the number of visible GCPs. Instead, higher RMSEs generally correspond with bright, clear weather conditions, whereas low RMSEs are associated with lower ambient light levels caused by heavy cloud cover or the low elevation of the winter sun (Table 5.2).

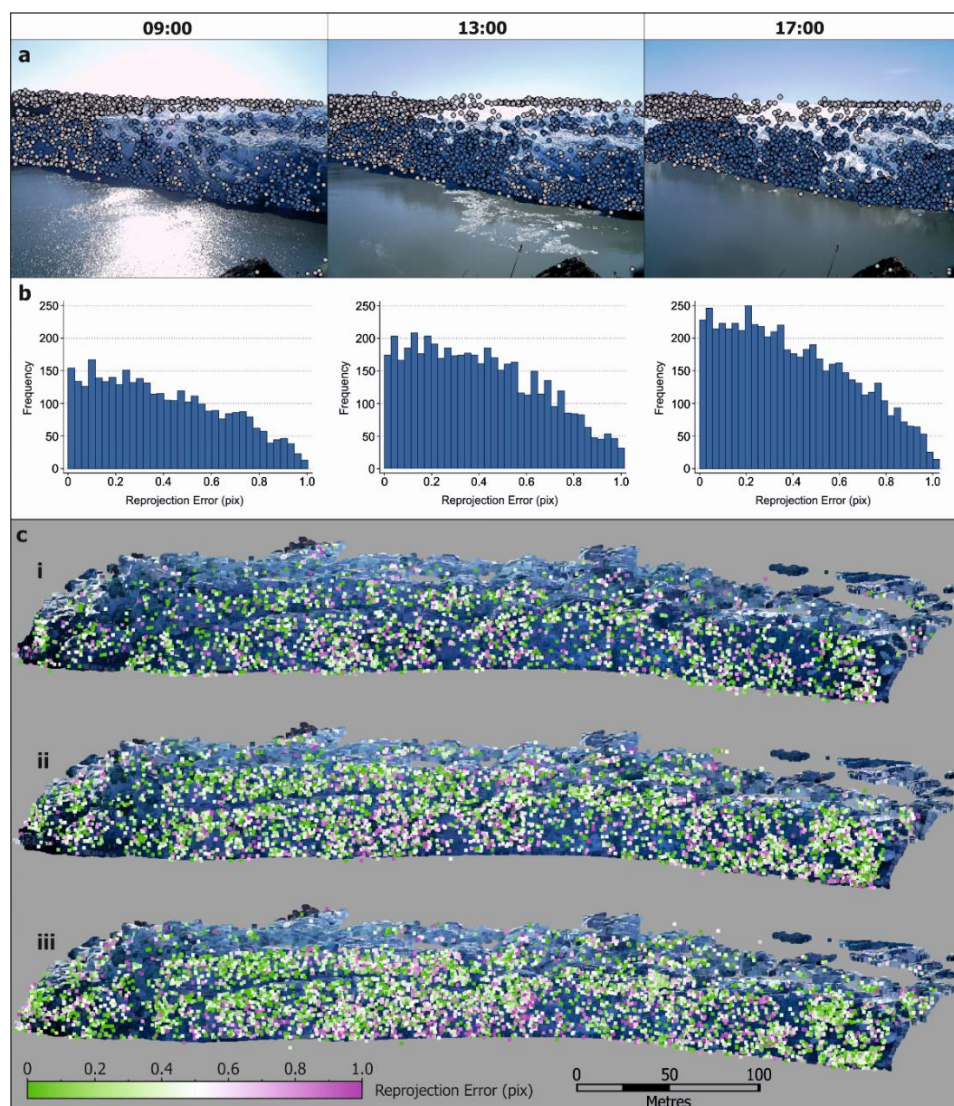


Figure 5.6. (a) Images recorded by camera A11 on 25 July 2014 showing daily variation in lighting conditions and accepted and rejected feature matches (blue and white circles respectively); (b) corresponding histograms of reprojection error for accepted feature matches; (c) reprojection error for individual points in the sparse point clouds derived from the (i) 09:00, (ii) 13:00, and (iii) 17:00 imagery.

### 5.5.3 QUANTIFICATION OF ICE-MARGIN DYNAMICS

The differencing of active point cloud pairs effectively identified examples of ice-margin change throughout the operation of the camera array, including calving events induced by ice-cliff undercutting at the waterline (Figure 5.7a), the collapse of spalling flakes along the ice-front (Figure 5.7b-d), and the resultant accumulation of ice debris on the frozen lake surface (Figure 5.7b-c). The detection of smaller magnitude ice-margin dynamics (e.g. advance/recession of the ice-front) was prohibited by the relatively large magnitude of the detection threshold and the short periods between image acquisition. The 2 m threshold was sufficient to closely delineate most calving activity, whereas the higher 4 m threshold omitted thin sections of ice peripheral to some calving events, and in one case, an event in its entirety (e.g. Figure 5.7a i). Analysis of the point clouds derived from midwinter imagery (Figure 5.7b) indicated that the lower 2 m threshold may lie beyond the margin of error when ambient light levels are low and/or the number of cameras available for alignment is limited (Table 5.2). Observed calving events at the 2 m threshold ranged from 234 to 1,475 m<sup>2</sup> in area and 815 to 8,725 m<sup>3</sup> in volume (Table 5.4). Calving area measurements were more sensitive than volume measurements to changes in the detection threshold, with an increase in threshold to 4 m prompting mean reductions in calving area and volume of ~60% and ~25% respectively.

Table 5.4. Area and volume calculations for calving events displayed in Figure 5.7. Note ‘i’ and ‘ii’ denote distinct calving events detected in the same active point cloud pair (see Figure 5.7).

Calving event dates	2 m Detection Threshold		4 m Detection Threshold	
	Calving area (m <sup>2</sup> )	Calving volume (m <sup>3</sup> )	Calving area (m <sup>2</sup> )	Calving volume (m <sup>3</sup> )
20-21 August 2014 i.	234	815	-	-
20-21 August 2014 ii.	760	4,358	553	3,726
19-20 February 2015	794	7,191	553	5,629
12-13 June 2015 i.	414	2,752	208	2,260
12-13 June 2015 ii.	538	3,995	334	3,314
10-11 August 2015	1,475	8,725	970	7,006

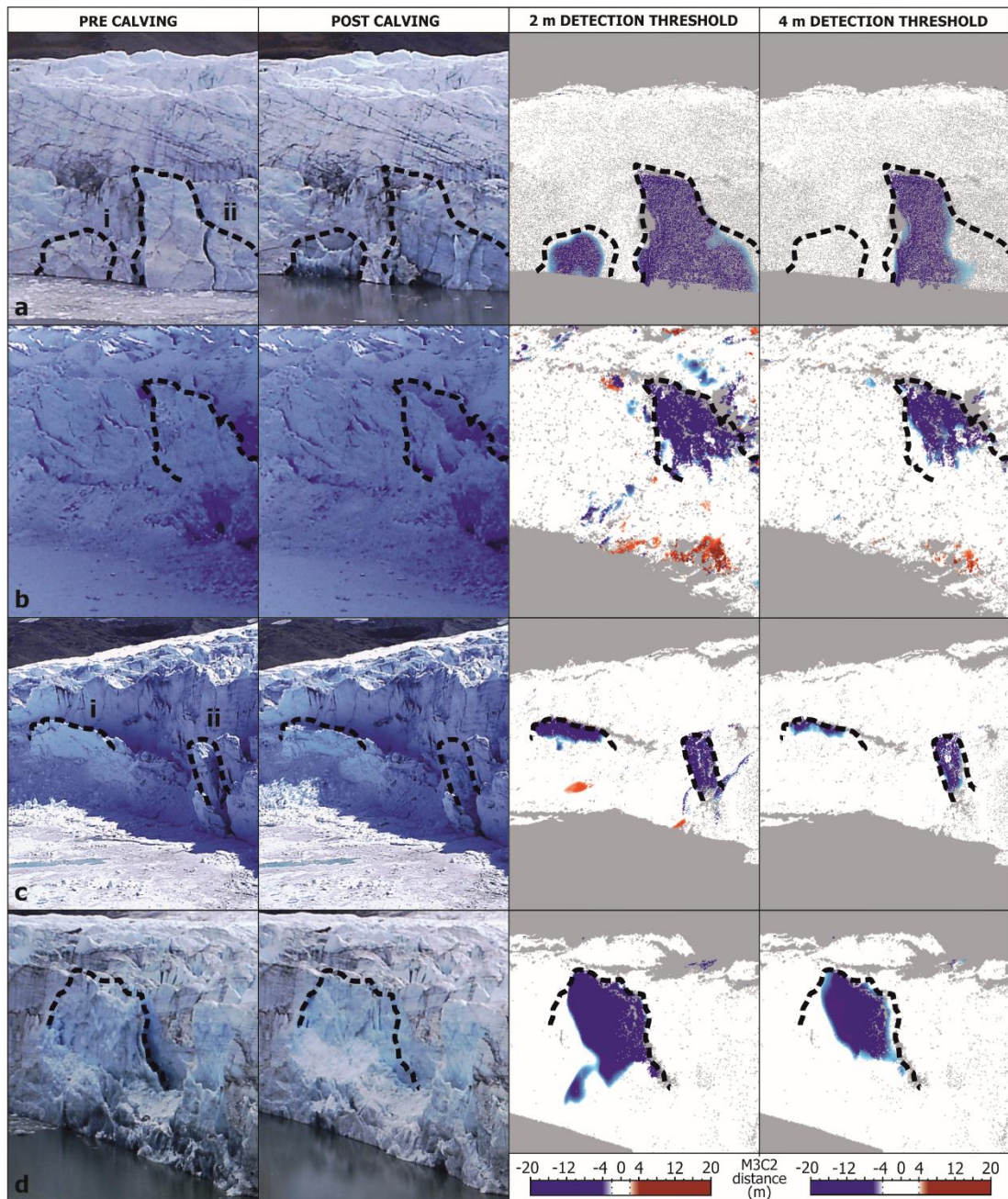


Figure 5.7. Camera imagery and M3C2 outputs for calving events identified in the active point cloud pairs. Events are dated: (a) 20-21 August 2014; (b) 19-20 February 2015; (c) 12-13 June 2015; and (d) 10-11 August 2015. Note for scale the vertical height of the ice-margin is ~50 m.

## 5.6 DISCUSSION

The above data effectively indicate that an integrated SfM-MVS and time-lapse approach can be used to analyse ice-margin dynamics at a hitherto unprecedented spatio-temporal resolution. However, there are significant challenges associated with generating prolonged 3D topographic records of ice-margins in the High Arctic. The parameters that influence point cloud coverage, density and accuracy are explored here, along with some strategies for improving point cloud quality.



### 5.6.1 CAMERA ARRAY GEOMETRY

At the most fundamental level, the geometry of the camera array clearly exerts considerable control over point cloud accuracy, coverage and density. A limited number of camera stations with poor distribution can cause distortions and gaps in point clouds (Bemis et al., 2014), while parallel image orientations can induce a systematic doming effect (James and Robson, 2014b). Good spatial coverage and convergent image geometries (where cameras are orientated towards the feature of interest) are necessary to mitigate against such systematic errors, though the angle of convergence is critical because angles of  $>25^\circ$  between adjacent camera stations can prevent the identification of keypoint correspondences because of apparent dissimilarities in surface texture (Bemis et al., 2014; Smith et al., 2016a). The setup of the camera array at Russell Glacier IDL facilitated convergent image acquisition, with the majority of cameras orientated towards the centre of the ice-margin (Figure 5.1). However, local topography prevented a uniform distribution of camera stations along the lake shore. Instead cameras were stationed in three primary groups (A1-A4, A5-A8 and A9-A15), which had low intra-group angular changes between camera stations, but necessarily possessed significant inter-group angular changes, most notably between groups A1-A4 and A5-A8 (Figure 5.1). Consequently, analysis of the keypoint matching stage of the workflow revealed that cameras A1-A4 contributed relatively few matches to the final point cloud, a problem later exacerbated by the loss of camera A2. The use of camera arrays therefore requires careful consideration of camera station distribution in order to minimise angles between neighbouring cameras; in some cases it may be preferable to limit the desired area of coverage, rather than deploy an isolated camera or group of cameras. In addition, the refinement of camera array geometry can be facilitated prior to its automation by the production of test point clouds in the field and careful analysis of the keypoint matches returned by each camera in the setup.

### 5.6.2 AMBIENT LIGHTING EFFECTS

The poor alignment of point cloud pairs in response to divergent ambient lighting or weather conditions was expected. Shadows are well documented to reduce key point matching in affected areas (Gienko and Terry, 2014; Bemis et al., 2014) and increase absolute error in point clouds (Gómez-Gutiérrez et al., 2014). In addition to shadows, glare and high-contrast imagery are also unfavourable for point cloud accuracy and density (Figure 5.6). Illumination of the feature of interest is therefore of particular importance to time-lapse SfM-MVS studies, where complications arise due to variable weather conditions and solar elevation.

This challenge is exacerbated by the highly reflective surfaces (ice and water) typical in glacial environments, particularly when the sun is low. Consequently, prolonged time-lapse studies in glacial environments will frequently contend with unfavourable lighting for image acquisition, therefore the setup of camera stations should follow careful consideration of: (i) the orientation of the cameras in relation to the feature of interest; (ii) the influence of local topography on shading; (iii) the path of the sun (daily and seasonally); (iv) prevailing weather conditions; and (v) locally reflective surfaces. One method to mitigate unfavourable conditions would be to factor redundancy into the timings for image acquisition by deliberately oversampling (e.g. collecting images at twice the rate desired); though it is important to consider the resultant impact on camera battery life and memory capacity.

It should also be noted that achieving all the desired qualities of a point cloud (e.g. good spatial coverage, high point density and low georeferencing RMSE) is likely to be a significant challenge for surveys of this nature. For example, these data tentatively indicate that low georeferencing RMSEs are achieved under lower ambient light levels, whereas larger clouds with greater point densities are associated with brighter conditions. Prioritising which of these qualities takes precedence should be determined by the objectives of the survey. For example, the minimisation of georeferencing RMSEs should take precedence where the real-world accuracy of a point cloud is paramount, whereas point cloud size and density can be prioritised in situations where the quantification of relative changes between successive clouds (generated from the same survey setup) is the primary objective.

### 5.6.3 POINT CLOUD ERROR

Isolation of individual error sources in SfM-MVS point clouds is challenging due to the number of confounding variables which determine accuracy (Smith et al., 2016a), relating to both survey design and underlying photogrammetric methods (James et al., 2017). The error inherent in topographic reconstruction is closely related to the distance between the feature of interest and the sensor, with conventional SfM-MVS surveys demonstrating a linear degradation of precision with increased survey range. Smith and Vericat (2015) analysed 50 extant SfM-MVS datasets and identified a relative precision ratio of 1:650 for SfM-MVS surveys, indicating model error of  $\sim 1$  m at survey ranges of  $\sim 650$  m (which in itself is sub-optimal, as James and Robson (2012) suggest that measurement precisions of 1:1,000 of the survey range should be achievable). Survey ranges in this study varied between 318 and 1,321 m, with a mean range of 765 m (Table 5.1). While external validation data were

unavailable for this study, this broadly compares with the distribution of errors observed when comparing two point clouds over an 'inactive' interval (Table 5.3). The poor projection accuracy of GCPs that were located at the periphery of the survey, and thus were observed in relatively few images, would explain why errors are higher than expected (Table 5.2).

#### 5.6.4 GROUND CONTROL POINT DISTRIBUTION

The dynamism and, in many cases, inaccessibility of ice-margins poses a challenge for the distribution of GCPs, which are conventionally stationed throughout the entirety of a survey area (James and Robson, 2012; Smith et al., 2016a). In addition, surveys that extend beyond the confines of GCP stations often exhibit increased point cloud error (Javemick et al., 2014; Smith et al., 2016a). Consequently, future implementations of this camera array approach should aim to improve the distribution of GCP stations where possible. The two GCP clusters employed in this study were necessarily peripheral to the survey area, being located >500 m from the centre of the ice-margin and, like the lake shores themselves, possessing relatively poor camera coverage (Figure 5.4). Accordingly, georeferencing RMSEs in similar setups are likely to be several orders of magnitude greater than conventional surveys where optimal GCP distribution and camera overlap can be achieved. The scale of the survey range also requires sizable GCP targets which increase the likelihood of misidentifying the exact reference point, which can be further exacerbated by fluctuating light levels. Stable landscape features are the most viable option for establishing a GCP network at long survey ranges (>1 km), where dedicated GCP targets are likely to be impracticable. For example, with this setup it is estimated that dedicated targets would need to be >1 m in diameter to be resolvable in the camera imagery. In addition, any such markers would need be sufficiently sturdy to withstand Arctic winter weather and the attentions of local wildlife (e.g. musk-ox, arctic fox).

Possible methods to mitigate the impact of peripheral GCPs on cloud accuracy would be to supplement the GCP network with multiple telemetric dGPS units stationed on the ice itself, or to survey and incorporate the positions of the camera stations in the bundle adjustment. Low-budget, high-precision dGPS units have become increasingly available in recent years (Völksen and Mayer, 2015; Jones et al., 2016) and could facilitate concurrent measurements of 3D ice motion. However, their successful application would again require that the dGPS units (or their associated targets) were accurately resolvable in the camera imagery.

#### 5.6.5 CAMERA CLOCKS AND WORKFLOW AUTOMATION

Despite their low-cost, the cameras were remarkably resilient to the cold and harsh conditions of the study site. Upon their retrieval internal camera clocks were assessed against a handheld GPS clock to determine the presence of any clock drift. The comparison revealed that all the camera clocks had drifted from their original synchronisation; with the final set of images (scheduled for 13:00 on the 24/09/15) acquired over a period of 27 minutes between 13:21 and 13:48. Although the period of image acquisition remained within the 30 minute survey duration recommended by Bemis et al. (2014) (to mitigate complications caused by changes to shadow length, weather and surface albedo), clock drift could be a significant barrier to the acquisition of topographic data sets from highly dynamic environments where data is required on a minute-by-minute basis, such as the lava flows observed in James and Robson (2014a). Methods for improving camera clock calibration and mitigating clock drift are outlined in Welty et al. (2013), although it should be noted that the necessary integration of cameras and GPS receivers would increase the power requirements of any prospective camera array setup. It is anticipated that the analysis of high-temporal resolution topographic data sets could be expedited by automation of the processing workflow and use of batch processing capabilities, although variable image quality is likely to provide a barrier to full automation. Rigorous testing of camera performance and provisional analytical workflows are therefore recommended before automation of a camera array in the field.

#### 5.6.6 DETECTION OF ICE-MARGIN DYNAMICS

As evidenced in this study the types of ice-margin dynamics that are resolvable using the time-lapse camera array approach will be determined by point cloud accuracy and survey interval. For example, while point clouds with relatively low accuracies ( $>2$  m) are likely to be sufficient for capturing calving events, higher accuracies ( $<1$  m) are required to capture small scale glacier changes, such as ice-cliff advance/retreat, ice-surface thinning/thickening, crevasse and ice fall serac dynamics or, perhaps in the context of water-terminating ice-margins, flexure, fracture and flotation. When compared to existing approaches for quantifying ice-margin changes, the differencing of 3D point clouds is advantageous because any topographic change can be calculated along the normal direction of the cliff face, thereby avoiding the amalgamation of 3D topographic change (resulting from melt and horizontal and vertical motion) that exists in vertical Digital Elevation Model (DEM) differencing (e.g. Thompson et al., 2016). In addition, mechanisms controlling any ice-margin topographic

change can be evaluated in 3D, revealing hitherto hard-to-detect phenomena such as thermo-erosional undercutting by ice-marginal lake water. Consequently, the deployment of camera arrays at ice-margins could afford considerable potential for improving knowledge of ice-marginal processes, including the spatial and seasonal distribution of calving events, the contribution of calving (e.g. total volume) to mass balance, and calving responses to external drivers including weather, water temperature and water level.

#### 5.6.7 APPRAISAL AGAINST TERRESTRIAL LASER SCANNING

These data suggest that the camera array presents an effective alternative to TLS for the acquisition of topographic datasets in glacial environments. The point clouds generated in this study possessed similar point densities to those derived via glacial TLS investigations at comparable scales (e.g. Gabbud et al., 2015); however, the camera array technique offers several further advantages over TLS. Most notably the cost of a TLS system (>£40,000) greatly exceeds that of a camera array (in this case ~£1,800), even when accounting for software licenses (e.g. Agisoft Photoscan Professional ~£3,000 for commercial purposes). Additionally, complex glacier geometries are likely to require multiple scanning stations which increases the complexity and duration of both TLS setup and post-processing. Finally, the automation of the camera array facilitates prolonged data acquisition well beyond the financial and climatic constraints of manual TLS operation.

### 5.7 CONCLUSIONS AND RECOMMENDATIONS

This study has presented the first set-up, operation and analysis of data from a time-lapse camera array to generate multi-temporal topographic surveys of a lacustrine-terminating ice-margin. These instruments and methods have been shown to be far more practical than field-based measurements, such as ablation stake monitoring, and of far greater spatio-temporal resolution than airborne or ground-based remote sensing. They therefore have significant potential for revealing mechanistic drivers and triggers of geomorphological change, not only for lacustrine ice-margins, but also for other rapidly-changing glacial environments such as ice-falls and, with due consideration of the baseline distances involved, marine ice-margins.

The following recommendations for the deployment of time-lapse camera arrays to acquire topographic datasets recognise that these instruments and methods are very much still in development and face considerable challenges, particularly in glaciological applications.

However, the practical guidance below should improve the setup, and therefore data quality, of future camera array based investigations:

- The types of ice-margin and other glacier dynamics that are resolvable using this approach will be determined by point cloud accuracy and survey interval. Consequently, the setup of the camera array and survey frequency must be tailored to the specific aims of any investigation.
- Ambient light levels determine both image quality and GCP visibility, therefore the positioning of camera and GCP stations should follow careful consideration of: (i) the orientation of the cameras in relation to the feature of interest; (ii) the influence of local topography on shading; (iii) the path of the sun (daily and seasonally); (iv) prevailing weather conditions; and (v) locally reflective surfaces, particularly ice, snow and water.
- The likelihood of camera failure or disturbance will increase with prolonged operation, consequently camera arrays should be designed to allow some redundancy in operative cameras whilst still maintaining sufficient image overlap for point cloud generation.
- Similarly, redundancy of GCPs should also be factored into the setup to account for dynamic lighting and variable ground conditions, including snowfall and vegetation growth.
- The sub-optimal distribution of GCPs in similar camera array setups is likely to produce georeferencing RMSEs several orders of magnitude greater than conventional SfM-MVS surveys. However, where access and survey range permit, this problem could be addressed by distributing multiple telemetric dGPS units (and associated targets) within the survey area.
- Quality control of the camera array setup should be performed in the field prior to full automation by downloading preliminary imagery to a laptop running SfM-MVS software and generating test point clouds, with particular attention given to the number of keypoint matches returned by individual cameras.
- Increasing the rate of image acquisition (i.e. oversampling) can mitigate the effect of changing weather conditions on image quality and limit the superimposition of geomorphological processes. However, the frequency of image acquisition must also reflect memory capacity and power availability, particularly when a finite power source is used, or where prevailing weather conditions, snowfall or daylight hours curtail the efficacy of photovoltaic cells.

Further opportunities for the development and scope of camera array based glaciological investigations will be facilitated by rapid advances in the technical specifications of time-lapse cameras and an increased affordability. Notably, camera models are increasingly equipped with MMS or Wi-Fi connectivity, enabling the immediate transmission of imagery from connected locations. Integration with a fully automated workflow for data analysis could therefore permit real-time analysis of geomorphological change. The incorporation of sensors into a camera array network could also facilitate the operation of cameras in response to external triggers (for example using seismic or motion sensors to activate the array during large calving events). Finally, the rapid development of software is also likely to further increase the range of variables that can be derived from camera array based investigations; for example James et al. (2016) present open access software capable of quantifying the horizontal and vertical ice velocity components of a glacier from an oblique terrestrial time-lapse image sequence.

## Chapter 6

### Seasonal Variability in Calving Processes at a Lacustrine Margin of the Greenland Ice Sheet

#### AUTHOR CONTRIBUTIONS

The work presented in this chapter has appeared in the following publication:

- Mallalieu, J., Carrivick, J.L., Quincey, D.J. and Smith, M.W. 2020. Calving Seasonality Associated With Melt-Undercutting and Lake Ice Cover. *Geophysical Research Letters*. **47**, GL086561.

The research presented in this chapter and the above publication was conceived and designed by Mallalieu, Carrivick, Quincey and Smith. Data processing and analysis was performed by Mallalieu. The manuscripts were written by Mallalieu with editorial comments from Carrivick, Quincey and Smith.



# Seasonal Variability in Calving Processes at a Lacustrine Margin of the Greenland Ice Sheet

## 6.1 ABSTRACT

A detailed understanding of calving processes at the lacustrine margins of the Greenland Ice Sheet is necessary for accurately forecasting its dynamic response to ongoing climate change. However, existing datasets of lacustrine calving are limited to summer seasons and to alpine glaciers. This study adopted an integrated time-lapse and SfM-MVS approach to generate the first continuous year-round volumetric record of calving processes at a lacustrine ice sheet margin. The resulting dataset revealed two distinct calving regimes that are associated with melt-undercutting and lake ice cover. The study also found that calving rates responded rapidly to sudden lake drainage. Given that lake temperature, lake ice cover and sudden lake drainages are controlled by air temperature and by ice-margin thinning, these results suggest that climate change, manifest in lengthening summer seasons, will accelerate rates of mass loss and terminus recession at lacustrine ice-margins in Greenland.

## 6.2 INTRODUCTION

The Greenland Ice Sheet (GrIS) has lost mass at an accelerated rate since the late 1990s and is one of the largest individual contributors to current and predicted sea level rise (Velicogna, 2009; Jiang et al., 2010; Gillet-Chaulet et al., 2012; Hanna et al., 2013; Kjeldsen et al., 2015; van den Broeke et al., 2016). Approximately half of the mass lost from the GrIS occurs at water-terminating margins and can be attributed to a combination of calving and subaqueous melt, which together comprise frontal ablation (van den Broeke et al., 2009; Khan et al., 2015). Existing efforts to quantify calving dynamics in Greenland have focused on several large, marine-terminating outlet glaciers responsible for draining the ice sheet interior (e.g. Ryan et al., 2015; Murray et al., 2015; Rignot et al., 2015; Medrzycka et al., 2016). However, the lacustrine calving margins of the GrIS have received comparatively little attention, despite: (i) ~8% of the western margin of the GrIS terminating in a lake (Chapter 4); (ii) a substantial increase in the number and area of ice-marginal lakes over the last three decades (Carrivick and Quincey, 2014); and (iii) an expectation that they will continue to expand into the future (Carrivick and Tweed, 2019). Specifically, the growth of ice-marginal lakes at the GrIS margin is significant in the short term because of their propensity to accelerate rates of mass loss and ice-margin recession through a range of thermo-mechanical controls, including the onset and promotion of calving (Carrivick and Tweed, 2013). These

effects on glacier dynamics have been extensively documented in alpine environments, including: Alaska (Boyce et al., 2007; Trussel et al., 2013); Patagonia (Naruse and Skvarca, 2000; Willis et al., 2012); the Himalaya (Basnett et al., 2013; King et al., 2018); Tien Shan (Mayer et al., 2008; Engel et al., 2012); Iceland (Schomacker, 2010; Dell et al., 2019); the European Alps (Tsutaki et al., 2011); and the Southern Alps of New Zealand (Kirkbride, 1993; Quincey and Glasser, 2009). On longer timescales, the relative importance of lacustrine controls on ice-margin dynamics in Greenland will increase as marine termini recede onto land (e.g. Joughin et al., 2010; Nick et al., 2013), whilst the growth and coalescence of ice-marginal lakes has also been identified as a key factor controlling ice stream initiation and rapid ice sheet collapse (Stokes and Clark, 2003; Stokes and Clark, 2004; Demidov et al., 2006; Perkins and Brennand, 2015). Consequently, a detailed understanding of the lacustrine margins of the GrIS is necessary to accurately forecast its dynamic response to ongoing climate change.

Lacustrine calving rates are typically an order of magnitude lower than those from marine environments (Benn et al., 2007; Truffer and Motyka, 2016). However, a sparsity of quantitative data means that calving processes and their associated drivers at lacustrine ice-margins remain poorly understood (Trussel et al., 2013; Purdie et al., 2016). Consequently, the relative importance of lacustrine calving to ice-margin dynamics remains challenging to assess. The scarcity of lacustrine calving datasets stems partially from the methodological challenges associated with acquiring long-term quantitative records of calving in highly dynamic and hazardous environments (Purdie et al., 2016; Mallalieu et al., 2017). In particular, the climatic and financial constraints of fieldwork in glacierised regions restricts most calving studies to the melt season, thus neglecting important seasonal variations in calving rates and processes. Where extended records of calving do exist, for example via the use of time-lapse photography, they typically lack the volumetric data necessary to link calving event magnitude to mechanisms and drivers of change (e.g. Amundson et al., 2010). Recently, integration of time-lapse photography with Structure-from-Motion (SfM) and Multi-View Stereo (MVS) techniques (e.g. Eltner et al., 2017; Mallalieu et al., 2017) has facilitated the long-term investigation of geomorphological change through the acquisition and analysis of multi-temporal topographic point clouds at fine spatio-temporal resolutions. These methods offer great potential for the characterisation and quantification of the complex calving processes driving mass loss at water-terminating ice-margins over extended durations.

This study employed an integrated time-lapse and SfM-MVS approach to quantify calving processes at a lacustrine margin of the GrIS using multi-temporal point clouds. Specifically the study aimed to: (i) present the first extended (>1 yr) volumetric record of calving from a lacustrine ice-margin; (ii) analyse spatial and temporal patterns in calving event frequency, volume and mechanism throughout the survey duration; and (iii) opportunistically explore the effects of two discrete lake drainage events on calving processes and ice-margin stability.

## **6.3 DATA AND METHODOLOGY**

### **6.3.1 STUDY SITE**

This research presents a record of calving from a  $\sim 1 \text{ km}^2$  ice-dammed lake ( $67^\circ 08' 10'' \text{ N}$ ,  $50^\circ 04' 25'' \text{ W}$ ) situated on the northern margin of Russell Glacier, which is a terrestrial outlet of the GrIS in western Greenland (Figure 5.1). The lake, hereafter referred to as Russell Glacier Ice-Dammed Lake (or IDL), is notable in the literature for annual sudden and extremely rapid drainage events via a subglacial conduit situated in its southwestern corner (Mernild and Hasholt, 2009; Russell et al., 2011). Following gauging of lake drainage events in 2010 and 2012, Carrivick et al. (2017a) invoked localised flotation of the ice-dam as the mechanism initiating sudden lake drainage, based on: (i) water depths exceeding 40 m and a maximum ice-dam thickness in the southwestern corner of the lake of  $\sim 50 \text{ m}$ ; and (ii) a numerical model demonstrating that the extremely rapid water egress could not be fully explained by thermo-erosion and conduit melt-widening. Since 2010 there has been a progressive reduction in drainage volumes and a trend of drainages occurring earlier in the melt season in response to ice-surface lowering and thus a reduced flotation threshold (Carrivick et al., 2017a). Ice-surface velocities in the vicinity of Russell Glacier IDL are  $\sim 30 \text{ m.a}^{-1}$  (Rignot and Mouginot, 2012).

### **6.3.2 IMAGE ACQUISITION AND POINT CLOUD GENERATION**

Point clouds of ice-margin geometry were generated using the integrated time-lapse and SfM-MVS approach described and evaluated in detail in Chapter 5 and Mallalieu et al. (2017). Consequently, a reduced synopsis is provided here. The primary dataset comprised an image archive of ice-margin dynamics spanning 426 days between 27 July 2014 and 20 September 2015, acquired via the installation of an array of fifteen trail cameras around the lake shore (Figure 5.1). The extensive image overlap afforded by the cameras was exploited using SfM-MVS processing in Agisoft PhotoScan Professional v.1.4.2 to construct dense point clouds of ice-margin geometry from discrete image sets. Point clouds were georeferenced and scaled

using a network of 18 ground control points (GCPs) established on stable landscape features adjacent to the ice-margin, and subsequently cropped to the area of greatest camera overlap to maintain high point densities. The resulting point clouds consistently captured the geometry of a ~550 m wide stretch of the calving margin, accounting for ~60% of the total lake – ice interface (Figure 5.4).

### 6.3.3 POINT CLOUD ANALYSIS

In order to perform a seasonal analysis of calving processes, point clouds were generated at 7 ( $\pm 1$ ) day intervals throughout the bulk of the survey period, with sampling frequency reduced to 28 ( $\pm 2$ ) day intervals between November 2014 and April 2015 to reflect decreased activity at the ice-margin (Table 6.1). The minor variations in sampling interval were caused by inclement weather conditions preventing the acquisition of viable imagery for SfM-MVS processing. In addition to the seasonal calving analysis, extra point clouds were generated with enhanced frequency around lake drainage events on 3 August 2014 and 28 July 2015 to investigate their effect on calving processes (Table 6.1).

A volumetric record of calving losses throughout the survey duration was established via the differencing and analysis of 56 successive point clouds of ice-margin geometry in CloudCompare v.2.9.1. A complete list of the tools and associated parameters employed in the analysis are included in Table 6.2 and illustrated in Figure 6.1. Initially, point clouds paired for analysis were co-registered using an iterative closest point algorithm to remove the effects of ice-margin advection or ablation, and thus isolate mechanical calving losses over the survey interval. The distances between co-registered clouds were subsequently calculated along the horizontal plane using the multi-scale model-to-model cloud comparison (M3C2) tool developed by Lague et al. (2013).

Table 6.1. Attributes of point clouds employed in calving analysis and associated lake measurements.

Cloud group	Date (DOY)	Time	Days between successive clouds	No. of aligned images	No. of visible GCPs	Georef. RMSE (m)	No. of points in cloud	Mean point density (pts/m <sup>2</sup> )	Lake status	Lake surface elevation (m a.s.l.)	Lake volume (10 <sup>6</sup> m <sup>3</sup> )
Drainage 2014	27 July 2014 (208)	16:00	-	15	11	5.91	1313255	19	Unfrozen	419.18	7.28
	30 July 2014 (211)	16:00	3	15	10	4.61	1341912	21	Unfrozen	420.38	8.03
	1 Aug. 2014 (213)	16:00	2	15	11	5.16	1265529	24	Unfrozen	420.55	8.14
	2 Aug. 2014 (214)	16:00	1	15	10	5.21	1381255	23	Unfrozen	420.65	8.20
	4 Aug. 2014 (216)	09:00	1.71	15	10	3.84	1746084	19	Unfrozen	405.05	0.15
	5 Aug. 2014 (217)	09:00	1	15	14	2.77	1498097	18	Unfrozen	405.12	0.18
	7 Aug. 2014 (219)	09:00	2	15	18	3.07	1483333	19	Unfrozen	405.25	0.23
10 Aug. 2014 (222)	09:00	3	15	12	1.48	1363129	22	Unfrozen	406.79	0.86	
Drainage 2015	22 July 2015 (203)	13:00	-	15	15	3.62	1197404	21	Unfrozen	418.31	6.74
	25 July 2015 (206)	13:00	3	15	13	5.08	1169522	21	Unfrozen	418.35	6.77
	27 July 2015 (208)	13:00	2	15	12	4.65	1167678	21	Unfrozen	418.45	6.83
	28 July 2015 (209)	13:00	1	15	11	3.89	1004842	21	Unfrozen	418.59	6.92
	30 July 2014 (211)	09:00	1.83	15	15	4.29	1395024	21	Unfrozen	405.94	0.51
	31 July 2015 (212)	09:00	1	15	15	4.79	1418010	19	Unfrozen	405.59	0.37
	2 Aug. 2015 (214)	09:00	2	15	14	4.14	1228995	25	Unfrozen	405.61	0.37
5 Aug. 2015 (217)	09:00	3	15	13	4.89	1502659	20	Unfrozen	406.12	0.58	
Seasonal	27 July 2014 (208)	13:00	-	15	11	3.76	1009558	24	Unfrozen	419.16	7.27
	3 Aug. 2014 (215)	13:00	7	15	13	4.38	1434794	24	Unfrozen	413.19	3.87
	10 Aug. 2014 (222)	13:00	7	15	13	5.23	1647595	24	Unfrozen	406.80	0.86
	17 Aug. 2014 (229)	13:00	7	15	11	4.31	1642565	24	Unfrozen	408.41	1.56
	24 Aug. 2014 (236)	13:00	7	14	10	4.18	1429112	21	Unfrozen	408.09	1.41
	31 Aug. 2014 (243)	13:00	7	14	7	2.49	1536645	22	Unfrozen	408.12	1.43
	7 Sept. 2014 (250)	13:00	7	14	8	2.95	1456360	21	Unfrozen	408.15	1.44
	15 Sept. 2014 (258)	13:00	8	14	10	4.51	1494638	21	Unfrozen	408.00	1.38
	21 Sept. 2014 (264)	13:00	6	14	8	5.59	1257575	18	Unfrozen	407.99	1.37
	29 Sept. 2014 (272)	13:00	8	7	3	17.92	1189879	31	Partial freeze	-	-
	6 Oct. 2014 (279)	13:00	7	7	3	11.62	1080670	37	Partial freeze	-	-
	12 Oct. 2014 (285)	13:00	6	14	4	3.51	1485558	24	Partial freeze	-	-
	19 Oct. 2014 (292)	13:00	7	14	10	4.82	1524638	24	Partial freeze	-	-
	16 Nov. 2014 (320)	13:00	28	14	6	4.90	1507726	21	Full Freeze	-	-
	12 Dec. 2014 (346)	13:00	26	11	6	3.14	1171866	28	Full Freeze	-	-
	10 Jan. 2015 (10)	13:00	29	12	4	4.14	848618	32	Full Freeze	-	-
	6 Feb. 2015 (37)	13:00	27	13	6	1.63	1164584	27	Full Freeze	-	-
	8 March 2015 (67)	13:00	30	12	5	1.52	1047770	25	Full Freeze	-	-
	5 April 2015 (95)	13:00	28	11	6	3.41	1191073	26	Full Freeze	-	-
	4 May 2015 (124)	13:00	29	14	7	4.85	1340645	23	Full Freeze	-	-
	11 May 2015 (131)	13:00	7	14	5	3.03	1454672	22	Partial freeze	-	-
	18 May 2015 (138)	13:00	7	11	6	5.74	1413511	25	Partial freeze	-	-
	24 May 2015 (144)	13:00	6	15	10	4.28	1475218	19	Partial freeze	-	-
	31 May 2015 (151)	13:00	7	15	14	4.08	1445646	24	Partial freeze	408.45	1.58
	7 June 2015 (158)	13:00	7	15	12	4.40	1309307	18	Partial freeze	408.57	1.63
	14 June 2015 (165)	13:00	7	15	10	5.67	1323112	20	Partial freeze	408.90	1.78
	21 June 2015 (172)	13:00	7	15	12	5.01	1424221	21	Partial freeze	410.97	2.75
	28 June 2015 (179)	13:00	7	15	12	3.29	1251347	21	Unfrozen	413.13	3.84
	5 July 2015 (186)	13:00	7	15	13	3.84	1228497	22	Unfrozen	414.19	4.40
	12 July 2015 (193)	13:00	7	15	8	4.79	856361	27	Unfrozen	416.18	5.50
19 July 2015 (200)	13:00	7	15	13	4.16	1133325	18	Unfrozen	418.19	6.67	
26 July 2015 (207)	13:00	7	14	7	3.00	860713	25	Unfrozen	418.43	6.82	
2 Aug. 2015 (214)	13:00	7	15	12	2.65	1506472	21	Unfrozen	405.60	0.37	
9 Aug. 2015 (221)	13:00	7	15	10	2.58	1465134	26	Unfrozen	406.86	0.89	
16 Aug. 2015 (228)	13:00	7	15	9	3.13	1281491	22	Unfrozen	408.31	1.51	
23 Aug. 2015 (235)	13:00	7	14	7	3.07	1382910	24	Unfrozen	408.70	1.69	
30 Aug. 2015 (242)	13:00	7	14	9	5.39	1299372	26	Unfrozen	409.50	2.05	
6 Sept. 2015 (249)	13:00	7	14	11	4.87	1156505	26	Unfrozen	410.22	2.39	
13 Sept. 2015 (256)	13:00	7	14	10	3.45	924709	25	Unfrozen	410.76	2.65	
20 Sept. 2015 (263)	13:00	7	14	8	2.59	1189637	24	Unfrozen	411.18	2.85	

Table 6.2. Tools and associated values employed for point cloud analysis in CloudCompare. Where parameters are absent from the table default settings were adopted. Note that all clouds were transformed so that the ice-cliff was normal to the Y axis prior to analysis.

Tool/Plugin	Parameter	Value
Fine registration (ICP)	Aligned	Cloud n+1
	Reference	Cloud n
	RMS difference	1.0e-8
	Final overlap	50%
	Random sampling limit	100000
M3C2 distance	Cloud #1	Cloud n
	Cloud #2	Cloud n+1
	Normals	40
	Projection	6
	Max depth	100
	Subsample cloud #1	0.1
	Preferred orientation	-Y
Filter points by value	Range: min	-100
	Range: max	-1.0 OR -0.5
SOR filter	Number of points for distance estimation	200
	Standard deviation multiplier threshold	2
Label connected components	Octree level	10 (grid step = ~0.5)
	Min. points per component	200
2.5D volume	Ground: Source	Cloud n+1
	Ground: Empty cells	Interpolate
	Ceil: Source	Segmented calving component
	Ceil: Empty cells	Leave empty
	Grid step	0.5
	Projection direction	Y
	Cell height	Average height

Conventional methods for measuring point cloud error and determining a level of detection (e.g. Brasington et al., 2003) are challenging to apply to camera array setups at glacial margins due to the suboptimal distribution of GCPs and sparsity of stable landscape features (Chapter 5; Mallalieu et al., 2017). Consequently, a threshold for detecting significant changes in ice-margin geometry was determined by measuring the standard deviations of distances between pairs of point clouds selected to be representative of the range of sampling intervals employed in the analysis (24 hour, 7 day, and 28 day intervals) and seasonal variability in image quality and GCP visibility. Distances were measured using the M3C2 tool at vertical 30 m<sup>2</sup> subsections of the ice-margin where a visual inspection of the image dataset determined there to be no structural changes over the survey interval. Analysis of the data found that 95% ( $\pm 2$  standard deviations) of distances between point cloud pairs at 24 hour and 7 day intervals were within the range of 0.22 m to 0.42 m; whilst distances between point cloud pairs at 28 day intervals were within 0.46 m to 0.66 m (Table

6.3). Thus conservative detection thresholds of  $\pm 0.5$  m and  $\pm 1.0$  m were adopted to distinguish statistically significant changes in ice-margin geometry from noise for successive point cloud pairs at 24 hour and 7 day intervals, and 28 day intervals respectively. The robustness of this approach for accurately delineating calving events is demonstrated through visual comparison with events resolvable in the image dataset (cf. Figure 6.2).

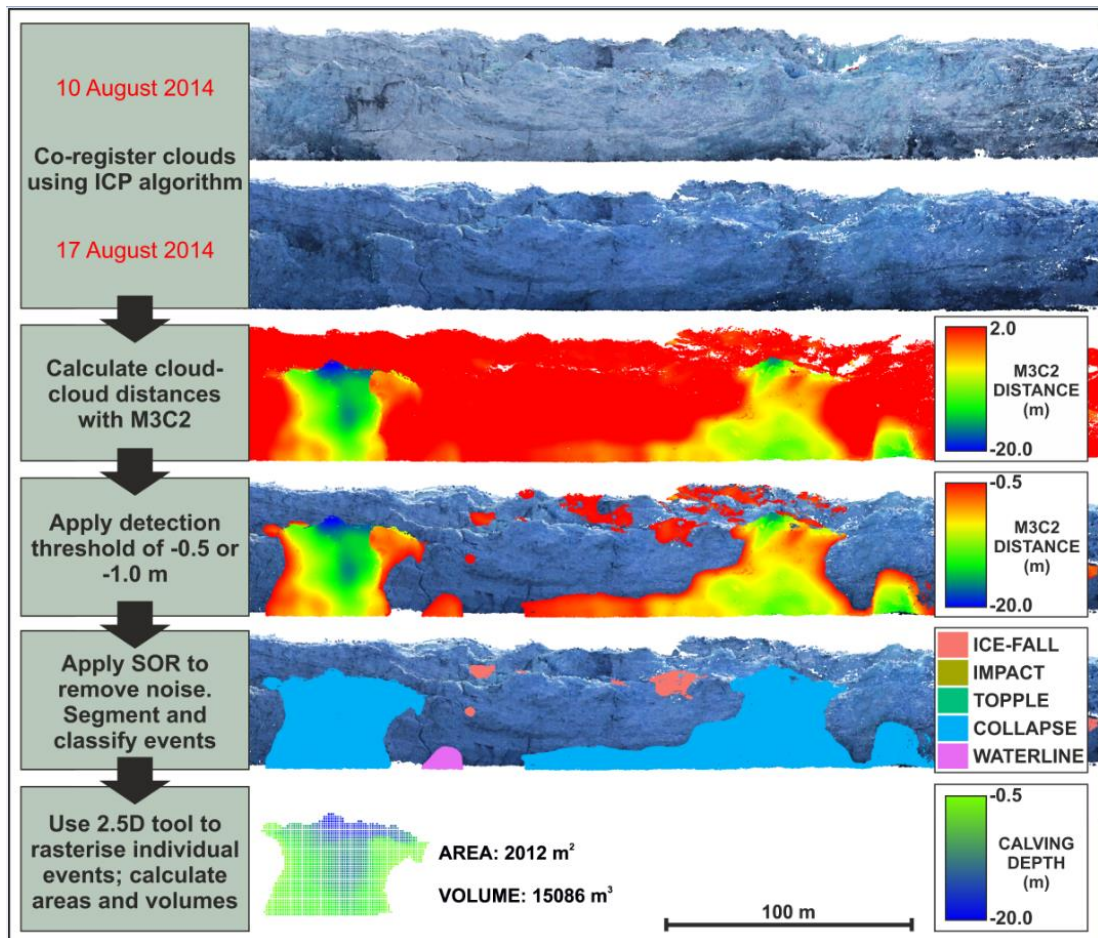


Figure 6.1. Schematic of workflow for point cloud analysis and derivation of calving data.

After differenced point clouds had been cropped to their respective detection threshold, they were cleaned using a statistical outlier removal tool to delete isolated points (accounting for  $<0.01\%$  of total points), and subsequently segmented into individual events using connected-component analysis. Finally, areas and volumes were calculated for each calving event by rasterising the segmented M3C2 components using the 2.5D volume tool (Figure 6.1). Calving rates were calculated by dividing the total calving volume between successive point clouds by the respective survey interval.

Table 6.3. Standard deviations of M3C2 distances measured between vertical 30 m<sup>2</sup> subsections of the ice-margin lacking structural changes.

Cloud group	Cloud 1: date (DOY)	Cloud 2: date (DOY)	Survey interval (days)	Mean change (m)	SD of change	2 x SD
Drainage 2014	1 August 2014 (213)	2 August 2014 (214)	1	0.01	0.13	0.26
	4 August 2014 (216)	5 August 2014 (217)	1	0.06	0.12	0.24
Drainage 2015	26 July 2015 (207)	27 July 2015 (208)	1	0.04	0.21	0.42
	30 July 2015 (211)	31 July 2015 (212)	1	-0.07	0.11	0.22
Seasonal (weekly)	10 August 2014 (222)	17 August 2014 (229)	7	-0.02	0.18	0.36
	29 September 2014 (272)	6 October 2014 (279)	7	-0.09	0.17	0.34
	28 June 2015 (179)	5 July 2015 (186)	7	-0.02	0.11	0.22
	12 July 2015 (193)	19 July 2015 (200)	7	0.03	0.16	0.32
Seasonal (monthly)	16 November 2014 (320)	12 December 2014 (346)	28	-0.02	0.31	0.62
	10 January 2015 (10)	6 February 2015 (37)	29	-0.03	0.23	0.46
	8 March 2015 (67)	5 April 2015 (95)	30	-0.10	0.24	0.48
	5 April 2015 (95)	4 May 2015 (124)	28	0.08	0.33	0.66

#### 6.3.4 CALVING CLASSIFICATION

Attempts to characterise calving processes in theoretical and mathematical models have proved challenging because individual events are controlled by a complex range of interacting processes (Benn et al., 2007). Recent advances in discrete element modelling have identified three broad mechanisms associated with calving: ice-cliff failure, undercut calving and buoyancy-driven calving (Åström et al., 2013; Benn et al., 2017). However, associated calving criteria remain untested due to a lack of quantitative observational records. In this study, a classification system for determining the mechanism of individual calving events was developed by assessing the nature of resultant geometric changes at the ice-margin and refining existing calving categorisations, principally those of Minowa et al. (2018) and How et al. (2019). Particular attention was paid to whether events: (i) occurred at or above the waterline; (ii) extended the full height of the ice-cliff; and (iii) demonstrated outward rotation from the ice-cliff prior to failure. Events were subsequently categorised into five classes: ice-falls, topples, impact events, waterline events, and collapses (Figure 6.2). The characteristics of key mechanisms are presented in Figure 6.3 using multi-temporal 2D profiles of the ice-cliff. No evidence of subaqueous calving was observed over the duration of the study.





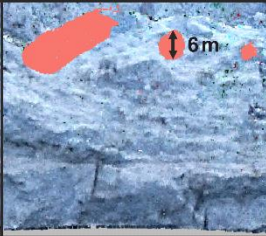


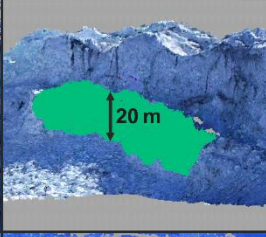
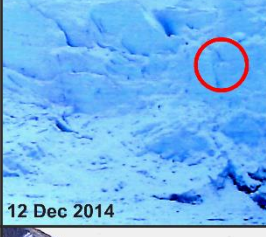
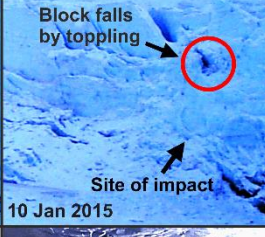



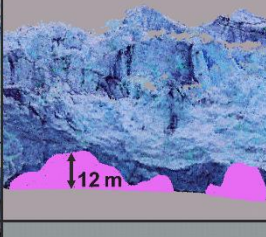


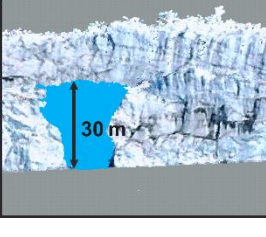
Classification	Pre-calving imagery	Post-calving imagery	Differenced point cloud
<b>Ice-fall:</b> Small-medium size events. Blocks of ice fall from ice-cliff, typically from higher-elevations. Triggered by structural weaknesses within the ice and/or undercutting at the waterline.	 17 Aug 2014	 24 Aug 2014	 6 m
<b>Topple:</b> Medium-large events. Outward toppling of sheets and stacks of ice, indicative of outward force imbalance at ice-cliff. Failure does not propagate down to water level.	 7 June 2015	 14 June 2015	 20 m
<b>Impact:</b> Small events triggered by impact of falling ice from higher elevations. Typically found on relaxed gradients below vertical or overhanging faces. Associated with Fall and Topple events.	 12 Dec 2014	 10 Jan 2015	 9 m
<b>Waterline:</b> Small-medium events. Blocks of ice detach at the waterline. Typically associated with undercutting by a thermo-erosional notch.	 15 Sept 2014	 21 Sept 2014	 12 m
<b>Collapse:</b> Medium-large events. Collapse of sheets and stacks of ice spanning the full height of the ice-cliff. Likely to be facilitated by both undercutting and outward force imbalance.	 1 Aug 2014	 2 Aug 2014	 30 m

Figure 6.2. Classification of the five calving mechanisms observed at Russell Glacier IDL, based on geometric changes at the ice-margin (determined via point cloud differencing), interpretation of camera imagery pre- and post-calving, and existing calving categorisations. Approximate calving event magnitudes are indicated by the scale bars on the differenced point clouds.

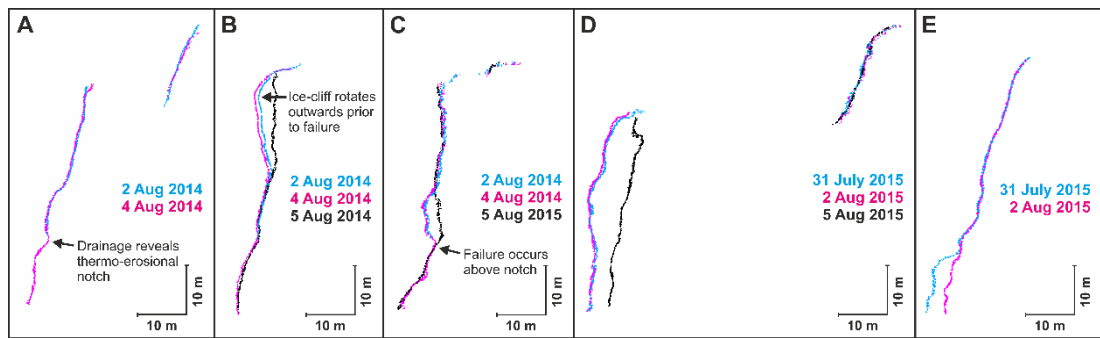


Figure 6.3. 2D profiles illustrating topographic changes at the ice-cliff associated with the 2014 and 2015 lake drainage events, including characteristics of key calving mechanisms. The positions of the 2D profiles along the ice-cliff are delineated by transects A-E in Figure 6.7. (a) ~1 m deep thermo-erosional notch at the waterline revealed by lake drainage; (b) outward toppling of ice-cliff at higher elevations prior to failure; (c) ice-fall above notch, reflecting undercutting and structural weaknesses in the ice-cliff; (d) collapse spanning full height of the ice-cliff; (e) failure at the waterline, likely to reflect undercutting by a thermo-erosional notch.

### 6.3.5 LAKE VOLUME AND METEOROLOGICAL DATA

Meteorological data, including mean daily temperature and wind speed, were logged by an automated weather station situated 1 km northeast of the lake at Point 660. Direct measurements of lake stage and temperature were impeded by the loss of a pressure transducer stationed on the lake bed. Consequently, a record of lake surface elevation was reconstructed indirectly from the ice-margin point clouds by using distinct debris features at the foot of the ice-cliff to manually position 5 tie-points at lake level for each image set in Agisoft PhotoScan. The elevations of the lake stages were determined using a trimmed mean of the tie-point elevations and subsequently converted to a volume using a stage-volume relationship derived from lake bathymetry in Russell et al. (2011) (Table 6.1). The presence of lake ice restricted the application of this technique to periods when at least some open water was visible at the foot of the ice-cliff. Existing records of lake temperature from 2010 and 2012 (from Carrivick et al., 2017a) are included to illustrate the typical lake temperature regime in the melt season. A qualitative record of ice-margin advection and recession relative to adjacent stable landscape features was determined by inspecting the imagery acquired by orthogonal (side-looking) trail cameras over the survey duration. Relationships between calving and environmental variables were tested using a Spearman's rank correlation matrix due to the non-normal distribution of the dataset.

## 6.4 RESULTS

### 6.4.1 CALVING EVENT ATTRIBUTES

Over the course of the survey duration 216 calving events were detected, amounting to total calving losses of 1.05 M m<sup>3</sup> (Table 6.4). Individual calving events ranged from 4 to 12,719 m<sup>2</sup> in area, with a mean of 808 m<sup>2</sup>; whilst event volumes ranged from 3 to 80,148 m<sup>3</sup>, with a mean of 4,888 m<sup>3</sup>. The volume-area ratio of calving events was approximately 1:1 for small magnitude events, but rose to 10:1 for the largest events, suggesting that large magnitude events possessed a proportionally greater depth than their smaller counterparts (Figure 6.4). Magnitude-frequency analysis of event volume indicated that total calving losses over the survey duration were dominated by infrequent, but high magnitude events, with the largest 10 events cumulatively accounting for 52% of total mass lost, whereas the smallest 100 events accounted for <1% of the total volume. Ice-fall was the most frequent calving mechanism, accounting for 38% of all events, followed by waterline events (26%), topples (19%), collapses (13%) and impact events (4%). In total, calving mechanisms operative above the waterline (ice-fall, topples and impact events) accounted for 61% of all events, whilst mechanisms associated with undercutting and notch formation (waterline and collapse) accounted for the remaining 39% of events. Calving mechanisms were also typified by disparities in event volume, with collapses possessing the largest mean volume (23,512 m<sup>3</sup>), followed by topples (7,013 m<sup>3</sup>), waterline events (1,078 m<sup>3</sup>) and the notably smaller ice-fall (305 m<sup>3</sup>) and impact events (284 m<sup>3</sup>) (Table 6.4, Figure 6.4). Consequently, collapses and topples were the dominant calving mechanisms over the survey duration, accounting for 63% and 29% respectively of total mass lost, with the remaining 8% of losses attributed to waterline, ice-fall and impact events (Table 6.4).

Table 6.4. Summary statistics of calving mechanisms, areas and volumes for events detected between 27 July 2014 and 20 September 2015 at Russell Glacier IDL.

Calving classification	Frequency		Event area (m <sup>2</sup> )			Event volume (m <sup>3</sup> )			Total calving volume	
	(#)	(%)	Mean	Max.	Min.	Mean	Max.	Min.	(m <sup>3</sup> )	(% of total calving loss)
Ice-fall	83	38.4	95	1453	5	305	8330	3	25249	2.4
Topple	42	19.4	971	8064	16	7013	76653	11	306053	29.1
Impact	8	3.7	102	428	9	284	1381	6	2270	0.2
Waterline	55	25.5	272	2846	4	1078	11025	4	59293	5.6
Collapse	28	13.0	3892	12719	441	23512	80148	2468	658332	62.6
Total	216	100							1051197	100

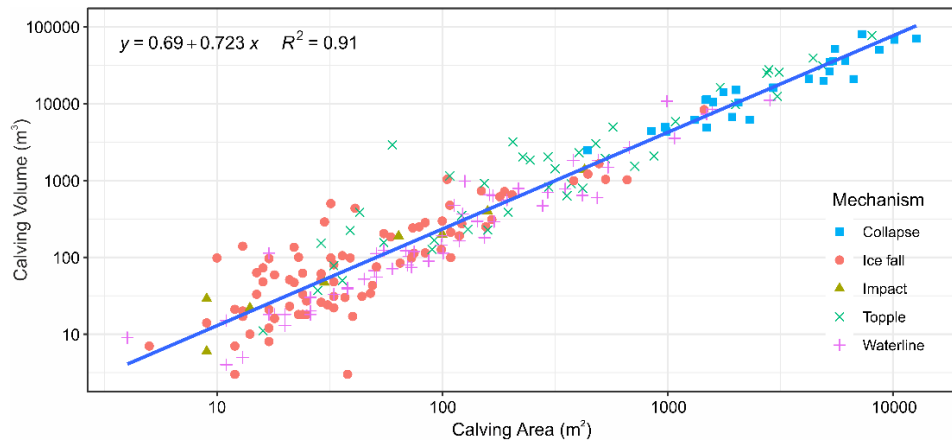


Figure 6.4. Area-volume relationship for calving events recorded at Russell Glacier IDL.

#### 6.4.2 SEASONAL VARIABILITY IN CALVING DYNAMICS

Temporal analysis of the seasonal dataset identified distinct cycles in calving properties (Figure 6.5). The highest calving rates and monthly calving volumes were typically associated with the months of August and September, whilst low calving rates characterised the period between December and July (Figures 6.5d, 6.5e). Perhaps unexpectedly, calving rates remained relatively high throughout October and November, despite the onset of lake freeze in late September (Figure 6.5c). Conversely, calving rates remained low throughout July even after the full thawing of the lake in late June. Calving event frequency followed a similar seasonal cycle, with the exception of June 2015 when a high number of ice-falls coincided with the return of positive air temperatures (Figures 6.5a, 6.5g). The onset of lake freezing and thawing coincided with notable changes in both the number of calving events and the contribution of each mechanism to the total calving volume (Figures 6.5c, 6.5f). In the months of August and September the collapse mechanism accounted for the vast majority of calving losses, whereas topples became the dominant driver of mass loss from October until the end of June. The only outlier occurred in July when waterline events contributed the majority of mass loss.

The seasonal cycle of ice-margin advance and recession was broadly synchronous with changes in calving rate, whereby ice-margin recession was associated with high calving rates in summer, and advection occurred when calving rates were minimal in winter (Figure 6.5). The sustained advance of the ice-margin into the lake basin between December 2014 and July 2015 was also evidenced by the development and growth of a large pressure ridge on the frozen lake surface running parallel to the ice-cliff. For the period in which the lake remained frozen a significant positive correlation ( $p < 0.05$ ) was identified between air temperature and calving event frequency. Whilst the lake remained unfrozen, significant

negative correlations ( $p < 0.05$ ) were identified between calving rate and lake volume, and calving rate and the rate of lake volume change (Figure 6.6).

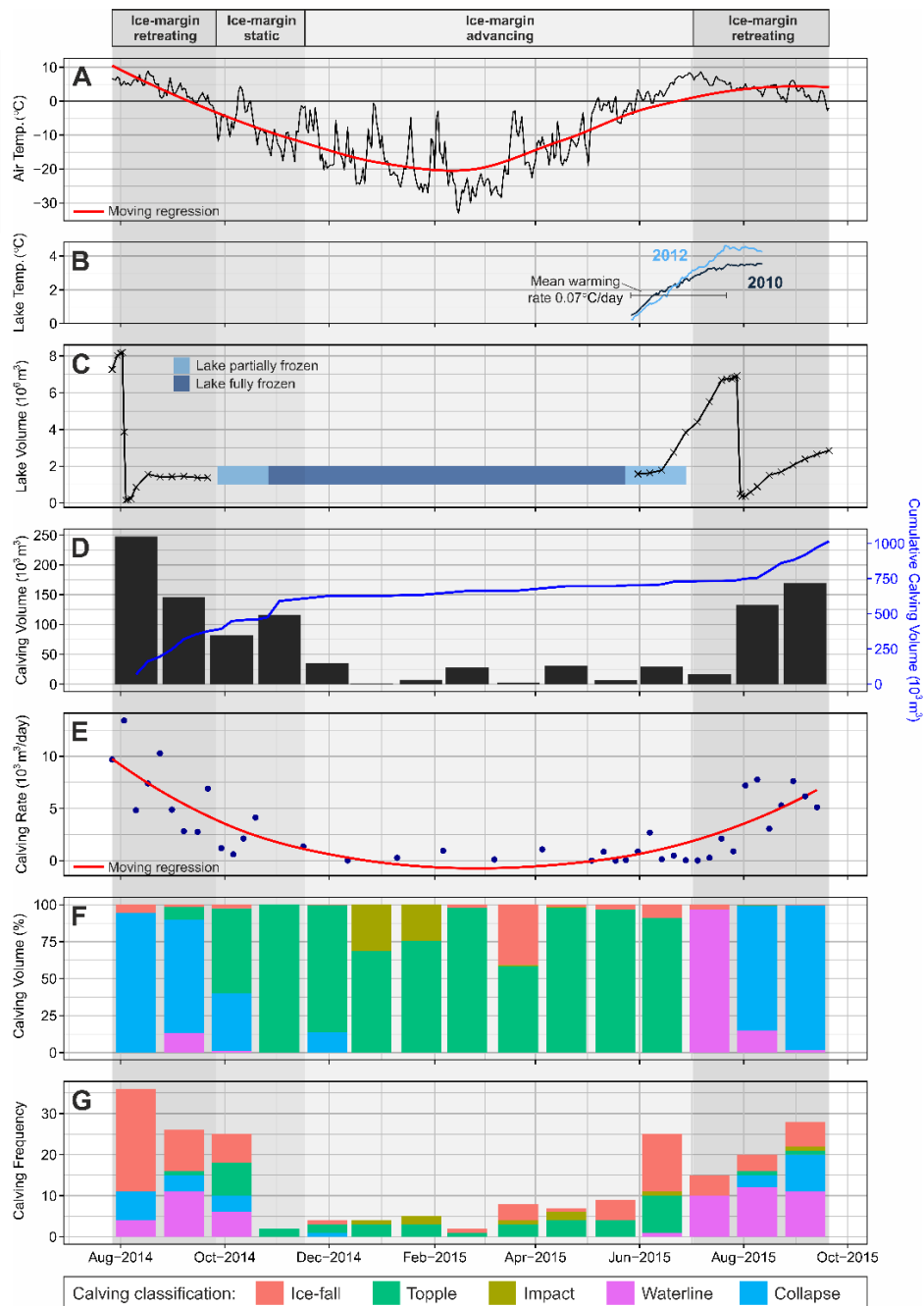


Figure 6.5. Seasonal record of calving, lake and meteorological activity at Russell Glacier IDL between 27 July 2014 and 20 September 2015. (a) Mean daily air temperature; (b) mean daily lake temperature from spring 2010 and 2012 (from Carrivick et al., 2017a); (c) lake volume, indicating onset of lake freeze/thaw and occurrence of drainage events on 3 August 2014 and 28 July 2015; (d) calving volume and cumulative calving volume over the survey duration; (e) calving rate; (f) calving volume by mechanism (%); (g) calving frequency by mechanism. Note that calving data were measured at  $7 (\pm 1)$  day intervals from 27 July to 19 Oct 2014 and 11 May to 20 Sept 2015, but are aggregated and plotted here at 28 day intervals to maintain a consistent sampling interval across the survey.

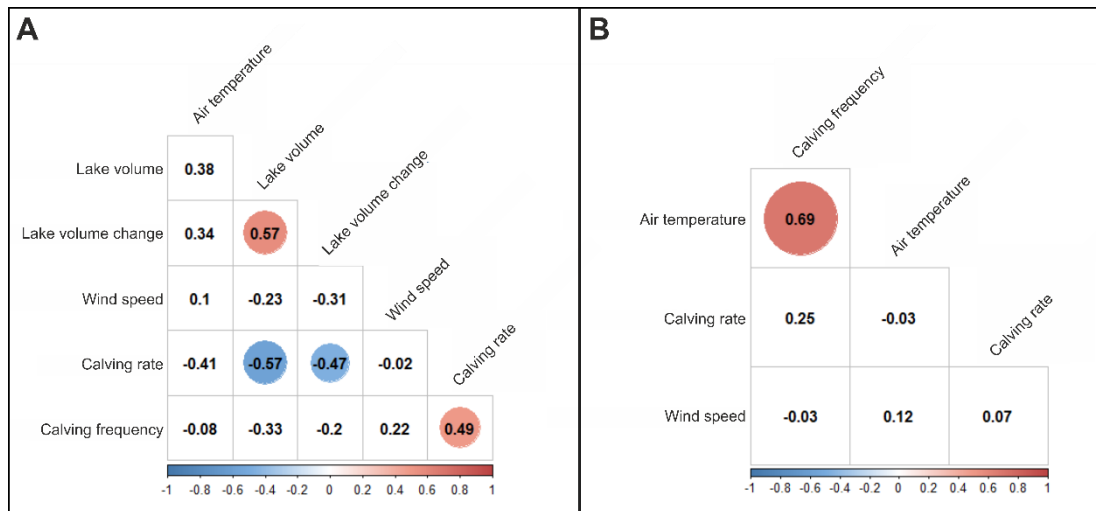


Figure 6.6. Spearman's rank correlation matrix of calving and environmental variables at Russell Glacier IDL. Statistically significant relationships ( $p < 0.05$ ) are denoted by a coloured circle. (a) Relationships between calving and environmental variables whilst the lake remained ice-free (27 July - 29 September 2014 and 26 June - 20 September 2015); (b) relationships between calving and environmental variables whilst the lake was partially or fully frozen (29 September 2014 - 26 June 2015).

#### 6.4.3 EFFECTS OF SUDDEN LAKE DRAINAGE ON CALVING DYNAMICS

Two lake drainage events occurred during the survey period. The first, on 3 August 2014, caused a fall in lake stage of 15.60 m over a ~41 hour period, corresponding to a reduction in lake volume of 8.05 M m<sup>3</sup>. The second event occurred on 28 July 2015 with a fall in lake stage of 12.65 m over ~44 hours, corresponding to a reduction of 6.41 M m<sup>3</sup> in lake volume (Figure 6.7, Table 6.1). Both events revealed the presence of a ~1.5 m deep thermo-erosional notch spanning the ice-cliff at the maximum elevation of the lake level (Figures 6.7, 6.3a). Calving activity in the six days prior to the 2014 drainage event was dominated by collapse, waterline and ice-fall events (Figure 6.7) representative of the operative calving mechanisms during the months of August and September in the seasonal calving survey (Figure 6.5g). During the drainage event itself calving activity was dominated by a series of discrete ice-falls immediately above the newly exposed thermo-erosional notch (Figures 6.7, 6.3c). In the 3 days subsequent to the lake drainage, calving losses were dominated by waterline, ice-fall and topple events, but within 6 days patterns and mechanisms of calving broadly mirrored those prior to the drainage event. Calving activity during the 2015 lake drainage replicated the patterns observed in 2014, but with the absence of any collapse events prior to and topple events subsequent to the lake drainage. Notably, high-magnitude collapse events were observed within 6 days of both the 2014 and 2015 lake drainage (Figure 6.7).

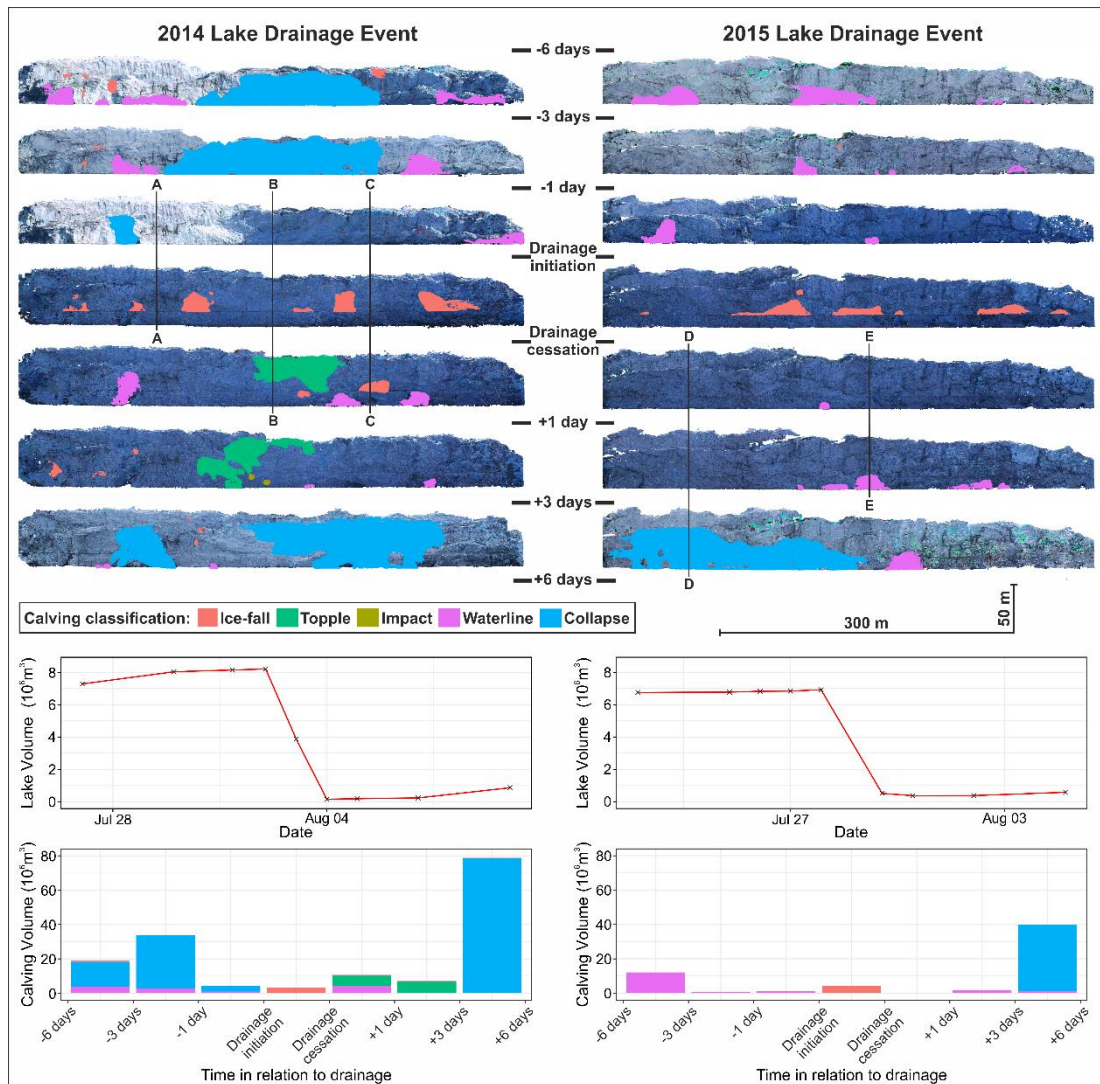


Figure 6.7. Spatio-temporal record of calving associated with lake drainage events commencing on the 3 August 2014 and 28 July 2015. Transects A-E denote the positions of the 2D ice-cliff profiles illustrated in Figure 6.3.

## 6.5 DISCUSSION

### 6.5.1 CALVING PROCESSES

Comparison of calving activity across multiple sites is challenging due to the absence of a standardised system for classifying observed calving events and divergent techniques for measuring event magnitude. However, the magnitude-frequency distribution of calving events observed at Russell Glacier IDL broadly replicates existing records from both lacustrine (e.g. Warren et al., 1995a; Minowa et al., 2018) and marine termini (e.g. Chapuis and Tetzlaff, 2014; Medrzycka et al., 2016; How et al., 2019), whereby relatively low-magnitude falls are the most prevalent calving mechanism, but mass loss is dominated by a small number of high-magnitude events.

The propagation of undercuts via subaqueous melting below the waterline is integral to calving processes because they increase force imbalances at the terminus and promote calving failures (Benn et al., 2007). Recent efforts by Benn et al. (2017) to simulate these calving processes at marine termini via discrete element modelling showed that undercutting of the calving front is associated with two magnitudes of calving event. Low-magnitude events occurred where the loss of support by undercutting exacerbated existing faults in the ice-cliff, causing localised, shallow subaerial failures, whereas high-magnitude events were associated with the propagation of suitably orientated surface fractures and outward bending of the ice-cliff over the undercut, leading to the collapse of the entire ice column. The observations and volumetric measurements of ice-fall and collapse events at Russell Glacier IDL (Figure 6.2, Table 6.4) therefore provide compelling evidence for these modelled low- and high-magnitude calving mechanisms respectively, and suggest that these processes are similar at both marine and lacustrine termini. These findings also support the observations of both Kirkbride and Warren (1997) and How et al. (2019) that calving follows a cyclical pattern whereby lower magnitude events, associated with failures at the waterline and the progressive upwards growth of an overhang, effectively precondition the calving front for high-magnitude events, which here are manifest as collapses and topples.

In comparison to marine margins, rates of subaqueous melt (and thus undercutting) at lacustrine margins are typically thought to be inhibited by the weak circulation characteristic of ice-marginal lakes that arises from negligible thermal stratification and limited upwelling of glacial meltwater (Eijpen et al., 2003; Warren et al., 1995a; Truffer and Motyka, 2016). However, existing observations illustrate significant variability in the contribution of subaqueous melt to frontal ablation at lacustrine margins. For example, although several studies have found subaqueous melt to be a negligible component of ablation (e.g. Boyce et al., 2007; Trussel et al., 2013), others have found it to be a significant component of mass loss and a rate-controlling process on calving, particularly where lake temperatures are exceptionally warm (e.g. Sugiyama et al., 2016; Haresign and Warren, 2005; Minowa et al., 2017) and/or the terminus is slow-flowing with limited crevassing (Kirkbride and Warren, 1997; Röhl, 2006). In this study, subaqueous melt is hypothesised to form a significant component of frontal ablation at Russell Glacier IDL due to the absence of an extensive projecting ice-foot at the base of the calving front following lake drainage (Figure 6.3a, 6.3c), or associated subaqueous calving events in the image archive. Consequently, these observations provide further evidence that subaqueous melt can be a significant component



of frontal ablation at lacustrine margins. However, a more detailed understanding of how the thermal regime and circulation of ice-marginal lakes affect subaqueous melt rates remains hindered by the scarcity of relevant records from lacustrine termini.

The extensive occurrence of waterline and collapse events across the width of the calving front at Russell Glacier IDL (e.g. Figure 6.7) suggests that melt-undercutting via thermo-erosional notch propagation is the primary control on calving losses and that, when the lake is ice-free, the long-term calving rate will therefore be related to the rate of undercutting. In addition, the presence of a thermo-erosional notch, rather than undercut, at the waterline (Figure 6.3a, 6.3c) illustrates an element of stratification in lake temperature. Such stratification in water temperature could conceivably also exist at marine glacier margins. Few measurements of notch propagation at lacustrine margins exist due to their inherently hazardous nature, but rates of  $0.8 \text{ m.day}^{-1}$  have been reported from Glaciar Leon (Haresign and Warren, 2005) and  $0.2$  to  $0.3 \text{ m.day}^{-1}$  from both the Miage (Diolaiuti et al., 2006) and Tasman (Röhl, 2006) glaciers. Although this study lacks direct measurements, such rates would not be inconceivable at Russell Glacier IDL because extensive waterline failures (exceeding the  $0.5 \text{ m}$  depth detection threshold) were observed within 24 hours of the 2014 lake drainage and 72 hours of the 2015 lake drainage, both of which considerably lowered lake level and thus reset notch formation (Figure 6.7). As with observations from other lacustrine termini (Truffer and Motyka, 2016) no upwelling meltwater plumes were observed at the calving margin during the survey, nor were en- or sub-glacial conduits revealed following the lake drainage. Consequently, meltwater upwelling is not considered to have had a significant effect on spatial patterns of calving along the ice-cliff. Because lake drainage at Russell Glacier IDL is flotation triggered, a transition from undercut driven calving to buoyancy driven calving, as documented at other lacustrine termini following downwasting (Dykes et al., 2011; Boyce et al., 2007; Trussel et al., 2013), remains unlikely despite recent observations of surface thinning (Carrivick et al., 2017a).

#### 6.5.2 SEASONAL VARIABILITY IN CALVING DYNAMICS

Calving activity at Russell Glacier IDL can be characterised into two distinct temporal regimes that are broadly coincident with the presence and absence of lake ice cover. Whilst the lake remains ice-free, calving processes and mass loss are driven by melt-undercutting, whereas following lake freeze calving is driven by force imbalances at the terminus that promote the outward toppling of unstable flakes and pillars of ice (Figures 6.5c, 6.5f). The significant

reduction in calving rates and monthly calving volumes commencing in December 2014 is hypothesised to be a consequence of calved material accumulating on the frozen lake surface throughout the autumn increasing buttressing of the calving front and thus suppressing further events (cf. topple image in Figure 6.2). The low calving rates observed in July 2015 are indicative of limited melt-undercutting despite the break-up of lake ice in the preceding month. However, records of lake temperature from 2010 and 2012 indicate that this time period coincided not only with the warming regime of the lake, but also with rapid increases in lake level (Figures 6.5b, 6.5c). Such high rates of lake level rise are likely to have considerably inhibited rates of melt-undercutting due to the dissipation of thermal energy over a greater elevation range (cf. Röhl et al., 2006). Suppression of calving rates by lake level fluctuations is also evidenced by the significant negative correlation identified between calving rate and the rate of lake volume change (Figure 6.6a). The ~10 m rise in lake level between mid-June and late-July 2015 is hypothesised to have inhibited calving processes associated with outward force imbalances over this period by reducing stress gradients at the calving front. In addition, the presence of a significant negative correlation between lake volume and calving rate (Figure 6.6a) also indicates that elevated lake levels restricted the magnitude of calving events by diminishing the vertical extent of the sub-aerial calving front.

Together these findings suggest that thermo-erosional notch development and associated ice-cliff collapse is the primary physical explanation for the recorded seasonal variability in calving activity. The observed ice-margin advance throughout winter and spring could arise from the process no longer operating, whereas ice-margin recession in summer is most likely driven by the resumption of melt-undercutting following lake warming (Figure 6.5). Furthermore, the seasonal advance and recession of the ice-margin coincides with the formation and disintegration of lake ice cover. In this regard the dynamics of lacustrine termini appear similar to the observed relationships between marine-terminating glaciers and ice-melange, whereby marine termini advance and retreat in response to the presence or absence of buttressing by an ice-melange respectively (Vieli et al., 2002; Amundson et al., 2010; Cassotto et al. 2015; Xie et al., 2019).

This study demonstrates that both lake thermal regime and lake ice cover could act as substantial controls on calving processes at lacustrine termini. Therefore climate-driven changes to lake water temperatures and ice cover regimes may have significant potential for perturbing rates of mass loss at calving margins, and consequently lacustrine ice-margin

dynamics. For example, studies of non ice-contact lakes in the Arctic region have identified a progressive earlier break-up of winter ice cover and extension of ice-free days in response to atmospheric warming in recent decades (Duguay et al., 2006; Smejkalova et al., 2016; Surdu et al., 2016). At lacustrine margins, similar shifts in ice cover regime would extend the duration of the calving season associated with higher-magnitude calving events (e.g. melt-undercut induced collapses), accelerating rates of mass loss, and potentially initiating a positive feedback whereby enhanced ice-margin recession, lake expansion and glacier thinning create favourable conditions for a transition from melt-undercutting to buoyancy driven calving, which has been associated with the rapid disintegration of several lacustrine termini in alpine environments (e.g. Boyce et al., 2007; Tsutaki et al., 2013). Similar responses have been observed at several Greenlandic marine outlets where terminus recession has been linked to reductions in sea ice duration and the earlier onset of melange disintegration (e.g. Joughin et al., 2008; Howat et al., 2010; Christoffersen et al., 2011). However, it is important to note that the sensitivity of ice-marginal lakes in Greenland to atmospheric warming is unlikely to be uniform, because: (i) the ice cover regime of Arctic lakes is primarily controlled by lake geometry (Arp et al., 2010); and (ii) the presence or absence of glacial meltwater inputs further complicates the seasonal evolution of proglacial lake thermal regimes (Carrivick and Tweed, 2013).

### 6.5.3 EFFECTS OF SUDDEN LAKE DRAINAGE ON CALVING DYNAMICS

Although immediate calving responses to the 2015 lake drainage were confined to discrete ice-falls along the thermo-erosional notch, the subsequent topple events under ice-free lake conditions are indicative of increased stress gradients at the calving front promoting the outward toppling of unstable flakes and pillars of ice in response to debuttressing. Similarly, How et al. (2019) observed that calving termini are highly sensitive to variations in backstress, with even relatively small reductions, such as those associated with the falling limb of an ocean tide, observed to increase calving frequency. The recurrence of waterline events within 24 hours of both the 2014 and 2015 lake drainages implies rapid re-establishment of melt-undercutting as the dominant driver of calving at Russell Glacier IDL. However, increased stress gradients promoting the outward bending of the ice-cliff over a newly formed undercut may also account for the large collapse events recorded within 6 days of both the 2014 and 2015 lake drainages, and thus signify the additional presence of a delayed process-response to lake drainage. Consequently, the capacity of lake drainage events to perturb dominant calving processes appears temporally-limited, although,

provided that the lake does not fully drain, calving rates are likely to increase in the aftermath of lake drainages due to the increased vertical extent of the sub-aerial calving front. Additionally, comparing the 2014 and 2015 lake drainages to earlier events from the same site suggests that the response of the ice-margin is strongly conditioned by the magnitude of the lake drainage. For example, lake level falls of 40 m and 48 m respectively were observed to trigger continuous ice-falls along the length of the ice-cliff in the 24 hours following a 1984 drainage (Sugden et al., 1985) and a 50 m advance into the lake basin in the months following a 2007 drainage (Russell et al., 2011). There has been no analysis of the impact of sudden lake drainages on ice-margin dynamics regionally, despite recognition of the increasing number of both ice-marginal lakes (Carrivick and Quincey, 2014) and sudden ice-marginal lake drainages (Carrivick and Tweed, 2019) around the GrIS.

#### 6.5.4 METHODOLOGICAL EVALUATION

This study has demonstrated that an integrated time-lapse and SfM-MVS approach has significant potential for acquiring extended (>1 yr) volumetric records of calving activity at lacustrine glacier margins and, with due consideration of the baselines involved, may also be suited to studies of marine termini with favourable geometry. A detailed evaluation of the camera array setup is provided in Chapter 5 and Mallalieu et al. (2017), so this section considers the effects of sampling interval on the calving dataset and priorities for the future development of the integrated time-lapse and SfM-MVS technique.

Time-lapse photography permits the monitoring of terminus dynamics at a considerably higher temporal resolution than those of traditional remote sensing surveys using satellite or airborne platforms. However, where time-lapse imagery is integrated with SfM-MVS processing, the construction and analysis of point clouds manually will necessitate extended survey intervals that are likely to exceed those of the calving processes under observation. For example, in this study although the total volumetric calving losses between repeat surveys are considered to be representative, the magnitudes and mechanisms assigned to individual events are necessarily tentative due to the potential for multiple events to coalesce between surveys. Similar effects of survey interval on calving records, particularly the under-representation of low-magnitude events at the expense of higher-magnitude events, have also been recognised in other calving analyses (e.g. Medrzycka et al., 2016; Pełlicki et al., 2015). Several recent time-lapse studies have attempted to mitigate the influence of survey interval on calving records, either by employing image analysis

techniques to automatically detect calving events (Vallot et al., 2019), or effectively adopting continuous process surveillance at calving termini, such as the acquisition of imagery at 3 second intervals in How et al. (2019). If integrated with SfM-MVS processing, such developments have significant potential for the acquisition of volumetric calving records at the event scale. Consequently, future priorities for the development of the integrated time-lapse and SfM-MVS technique include the full automation of the point cloud workflow to permit analysis of higher-temporal resolution datasets and, where surveys are to extend beyond several days, the remote-transmission of imagery to avoid limits to memory capacity. Innovation in these areas has considerable potential for facilitating the real-time acquisition of volumetric calving records and thus the investigation of seasonality in calving processes at the event scale. In addition, such volumetric datasets would be well suited to the purposes of parameterising and validating the latest generation of discrete element calving models (e.g. Åström et al., 2013; Benn et al., 2017). More widely, the real-time transmission of photogrammetric records of ice-marginal lake and glacier dynamics is emerging as a novel method for the prediction, monitoring and early warning of glacial lake outburst floods in densely populated mountain regions (e.g. Mulsow et al., 2015; Carvallo et al., 2017).

Although this study identified some statistically significant correlations between calving activity and environmental variables, the complex properties of proglacial water bodies and calving mechanics typically challenge statistical analyses of environmental drivers. For example, even when records of lake temperature are available they are not necessarily indicative of melt-undercutting rates because of the confounding effects of a wider array of intrinsically linked parameters, including ice-cliff geometry, lake circulation and fluctuations in water level (Röhl, 2006). Consequently, more advanced statistical analyses may be necessary to link environmental drivers to calving activity, although it should be noted that the application of stepwise regressions, capable of considering the additive effect of two or more variables, have also struggled to elucidate environmental controls on calving processes (e.g. Pętllicki et al., 2015).

## **6.6 CONCLUSIONS**

This study has presented the first extended (>1 yr) volumetric record of calving losses at a lacustrine ice-margin. The associated dataset enabled the recognition of two distinct calving regimes: when the lake was ice-free high calving rates were driven by processes associated with thermally-driven melt-undercutting; whereas when the lake was frozen lower calving

rates were driven by force imbalances at the ice-cliff. We also inferred that a further reduction in calving activity in the winter months was a response to the buttressing effect of previously calved material accumulating in front of the ice-margin on the frozen lake surface. Consequently, changes to lake water temperature and to seasonal lake ice cover, as would be expected with warmer and lengthening summers with climate change, are hypothesised to have significant implications for rates of mass loss and thus wider lacustrine ice-margin dynamics. In addition, sudden lake drainage events were observed to have a temporally-limited impact on calving activity, with dominant calving processes re-establishing within days of lake drainage. However, calving rates did increase following lake drainage events due to the increased vertical extent of the sub-aerial calving front. More widely, the integration of time-lapse photography and SfM-MVS techniques has been demonstrated to be well suited to the acquisition of volumetric calving records from glacier termini and, with advances in the automation of point cloud workflows and the remote-transmission of imagery, has considerable potential to facilitate the real-time acquisition of volumetric calving records and investigation of calving processes at the event scale.

# Chapter 7

## Discussion and Conclusions

### 7.1 INTRODUCTION

The increased prevalence of ice-marginal lakes in many of the world's glacierised regions is important because of their capacity to amplify rates of mass loss and glacier recession through a series of thermo-mechanical controls at the ice-margin, including the onset of calving. However, a sparsity of data means that lacustrine ice-margin dynamics and mass loss processes remain poorly understood and are typically omitted from projections of glacier change and sea level rise. The enhanced formation and growth of ice-marginal lakes along the western margin of the GrIS in recent decades is therefore of particular importance because the ice sheet is one of the largest contributors to contemporary sea level rise, and because dynamic change at ice sheet margins is one of the greatest sources of uncertainty in sea level rise projections. Consequently, the purpose of this thesis was to present the first quantitative assessment of the impact of ice-marginal lakes on the ice-margin dynamics of the GrIS. Specifically, a combination of remote sensing analyses and field-based time-lapse photography have been employed to investigate lacustrine ice-margin change at a regional-decadal and a local-seasonal scale respectively. This chapter provides a summary of the work presented in the thesis, considers the broader implications of the results and identifies priorities for future research. Detailed discussions of the individual components of the research are included within the respective results chapters (4-6) and are therefore not repeated here.

### 7.2 RESEARCH SUMMARY

A remote sensing approach was employed in Chapter 4 to investigate changes in ice-margin extent along the western margin of the GrIS at a regional-decadal scale. The Landsat image archive was used to generate an inventory of ice-marginal lakes and delineate the ice-margin along a ~5000 km stretch of the GrIS at approximately 5-year intervals between 1987 and 2015. Statistical analyses were used to perform a comparative study of changes in the extent of ice-margins terminating in lacustrine, terrestrial and marine settings, and investigate relationships between ice-marginal lake properties and rates of recession at lacustrine termini. The analyses identified an extended and accelerating phase of ice-margin recession in west Greenland from 1992 onwards irrespective of margin type, but also revealed

divergent rates of change at lacustrine, terrestrial and marine margins respectively. In particular, lacustrine termini were notable for a progressive increase in mean annual ice-margin recession rates, which grew by an order of magnitude between 1987 and 2015. Furthermore, ice-margin recession at lacustrine margins increasingly outpaced that of terrestrial margins over the duration of the study, which was hypothesised to arise from increases in lake size and a lengthening of the season over which lacustrine driven processes of mass loss were active. In addition, significant relationships between rates of lacustrine margin recession and several lake properties were also identified, including lake area, latitude, altitude, and the length of the lake – ice-margin interface. Although the results suggested that ice-marginal lakes are becoming increasingly important drivers of mass loss from the GrIS, the causal connections between ice-marginal lake prevalence and enhanced ice-margin recession could only be hypothesised in the absence of volumetric records of change and observations of the processes driving mass loss at the lake – ice-margin interface.

Chapter 5 therefore presented and evaluated a new method for acquiring volumetric records of lacustrine ice-margin change on a local-seasonal scale. Developments in the field of SfM-MVS were integrated with time-lapse photography to create a time-lapse camera array capable of reconstructing 3D feature geometry from sparse image datasets acquired using trail cameras. The camera array was deployed at Russell Glacier IDL, a lacustrine margin of the GrIS in west Greenland, between July 2014 and September 2015 with the aim of acquiring extended fine spatio-temporal resolution datasets of ice-margin dynamics. Approximately 19,000 images of the ice-margin were acquired over a continuous 426 day period, from which a series of test point clouds were generated. The technique successfully detected a variety of topographic changes at the lacustrine margin throughout the survey period, including calving events and the accumulation of calved debris on the frozen lake surface. However, challenges associated with ambient light levels, reflective surfaces and the large survey range prevented the detection and measurement of smaller magnitude ice-margin dynamics, such as daily rates of ice-margin advection/recession or buoyancy of the ice-margin.

The time-lapse camera array was subsequently employed in Chapter 6 to investigate seasonal variability in lacustrine calving processes at Russell Glacier IDL. A total of 56 successive point clouds of ice-margin topography were differenced to detect mechanical calving losses systematically throughout the 14-month long survey period, which also incorporated two sudden lake drainage events. An extended record of calving activity was



established by measuring the area and volume of individual calving events and classifying associated mechanisms of calving failure. In addition, relationships between calving and potential environmental drivers were tested statistically. Over the duration of the survey 216 calving events were detected, amounting to total calving losses of 1.05 M m<sup>3</sup>. The classified calving mechanisms were characterised by notable disparities in event volume, with collapse and topple events considerably greater in magnitude than waterline, ice-fall and impact events. Collapse and topple events were also the dominant calving mechanisms over the duration of the survey, cumulatively accounting for 92% of total mass loss. Temporal analysis of the dataset identified two distinct calving regimes: under ice-free lake conditions high calving rates were driven by processes associated with thermally-driven melt-undercutting; whereas, when the lake was frozen, low calving rates were driven by force imbalances at the ice-cliff and were further diminished throughout the winter months by the buttressing effect of calved material on the frozen lake surface. Consequently, climate-driven changes to lake water temperature and to seasonal lake ice cover were hypothesised to have significant implications for rates of mass loss at lacustrine ice-margins. Furthermore, high lake levels and lake level variability were found to be inversely correlated with calving rates. Finally, two sudden lake drainage events were found to have a temporally-limited impact on calving activity, with dominant calving processes re-establishing within days of both lake drainages.

### **7.3 RESEARCH IMPLICATIONS**

Favourable conditions for enhanced ice-marginal lake formation and growth are likely to occur in western Greenland over the 21<sup>st</sup> century in response to: amplified atmospheric warming (Schuenemann and Cassano, 2010; Bevis et al., 2019); increased surface melt and runoff (Franco et al., 2013; Trusel et al., 2018); and continued ice-margin thinning and recession (Pritchard et al., 2009; Aschwanden et al., 2019), predominantly over an inverse bed slope (Carrivick et al., 2017b; Morlighem et al., 2017). Consequently, the research outcomes of this thesis are particularly pertinent for the future dynamics of the GrIS and its ultimate contribution to sea level rise. Specifically, three key findings suggest that ice-marginal lakes will play an increasingly important role in rates and patterns of deglaciation at the western margin of the GrIS in coming decades. Firstly, the evidence that lacustrine margins of the GrIS receded faster than, and increasingly outpaced, their terrestrial counterparts between 1987 and 2015 (Chapter 4, Section 4.4.2), indicates that any future expansion in the number and area of ice-marginal lakes is likely to be accompanied by an associated increase in local rates of ice-margin recession and thus mass loss. Secondly, the

statistically significant relationships identified between lake parameters and rates of lacustrine margin recession (Chapter 4, Section 4.4.3) suggest that continued increases in ice-marginal lake size (see Carrivick and Quincey, 2014) will further amplify rates of ice-margin recession, especially for lakes situated at lower latitudes and altitudes. In addition, the greater depths typically associated with larger lakes (Huggel et al., 2002) will create increasingly favourable conditions for buoyancy driven calving, particularly when paired with thinning ice-margins, thus leading to higher magnitude calving losses and enhanced ice-margin recession (e.g. Boyce et al., 2007; Dykes et al., 2011; Trussel et al., 2013). Finally, the recognition of distinct seasonal calving regimes associated with melt-undercutting and lake ice cover (Chapter 6, Section 6.4.2), highlights the considerable potential for atmospheric warming to alter rates and mechanisms of mass loss at the lake – ice-margin interface. In particular, lengthening summer seasons are likely to extend the duration over which high magnitude calving processes are operative, thus further enhancing ice-margin recession and mass loss from the lacustrine margins of the GrIS.

The enhanced formation and growth of ice-marginal lakes at the margin of the GrIS is also likely to have a number of broader implications for the proglacial environment. For example, newly formed ice-marginal lakes may present considerable opportunities for hydropower production, water supply and tourism in Greenland, whilst concurrently increasing the risks posed by natural hazards, such as GLOFs, to local communities. A review conducted by Haeberli et al. (2016) of the opportunities and risks posed by the formation of new ice-marginal lakes in the Swiss Alps, observed that the rapid pace of deglaciation and ice-marginal lake evolution could act as a major constraint on the time available for complex decision making and the effective management of conflicts between local stakeholders. Therefore, focused monitoring and modelling of deglaciation in Greenland may be necessary to respond with sufficient speed to the opportunities and threats posed by ice-marginal lake evolution to local communities. In addition, ice-marginal lakes and rivers have become increasingly recognised as important components of geomorphological, geochemical and ecological systems due to their role in the storage and transportation of sediments and solutes, including nutrients and carbon, through the proglacial zone (e.g. Yde et al., 2014; Anderson et al., 2017; Hasholt et al., 2018; Pierre et al., 2019; Wadham et al., 2019). Consequently, the changes to meltwater supply and storage that could result from rapid deglaciation and ice-marginal lake evolution in Greenland (for example, in response to expanded lake capacity, enhanced frontal ablation, an extended melt season, or increasingly

frequent GLOFs), are likely to have complex and wide-ranging impacts throughout the proglacial environment.

Reconstructions of the last deglaciation indicate that the relative importance of lacustrine forcing on the dynamics of the GrIS could increase considerably in response to continued ice-margin recession over millennial timescales. Specifically, the recession of major marine termini onto land will limit the influence of marine forcing on ice-margin dynamics (e.g. Winsor et al., 2015), whilst the coalescence of large ice-marginal lakes at ice sheet margins has been widely cited as a key control on ice-stream formation and subsequent rapid ice sheet collapse (e.g. Stokes and Clark, 2003; Stokes and Clark, 2004; Demidov et al., 2006; Perkins and Brennand, 2015). Notably, ice stream initiation is hypothesised to commence via the same positive feedback responsible for increasing the buoyancy and velocity of contemporary lacustrine termini, and ultimately enhancing rates of ice-margin recession, mass loss and dynamic thinning. Consequently, the recent increases in the number and area of ice-marginal lakes at the margin of the GrIS can be interpreted as a key juncture in the deglaciation of Greenland.

#### **7.4 FUTURE RESEARCH**

This thesis has detailed the first attempt to quantitatively assess the impacts of ice-marginal lakes on the ice-margin-dynamics of the GrIS. The primary processes and dynamics investigated through this research, and their context within the broader suite of lacustrine ice-margin dynamics, are illustrated in Figure 7.1. However, due to the wide array of lacustrine impacts on ice-margin dynamics, the research objectives here have only addressed a relatively narrow subset of ice-margin behaviour: specifically calving processes at a local-seasonal scale and lacustrine ice-margin recession at a regional-decadal scale. Consequently, there remains considerable scope for further analyses of lacustrine ice-margin dynamics at both the GrIS and at other ice masses. In particular, a sparsity of data means that many lacustrine impacts and ice-marginal processes remain unquantified or poorly constrained. Furthermore, several new hypotheses have developed from the research presented in this thesis, particularly regarding the effects of a lengthening melt season and increasing lake temperatures on frontal ablation processes. This section therefore considers future research priorities for the study of lacustrine ice-margin dynamics at both a local-seasonal and a regional-decadal scale, and also explores how theoretical approaches could be employed to investigate lacustrine ice-margin dynamics more widely. Finally, this section will also consider

the potential broader cryospheric and geomorphological applications of the time-lapse camera array developed in Chapter 5.

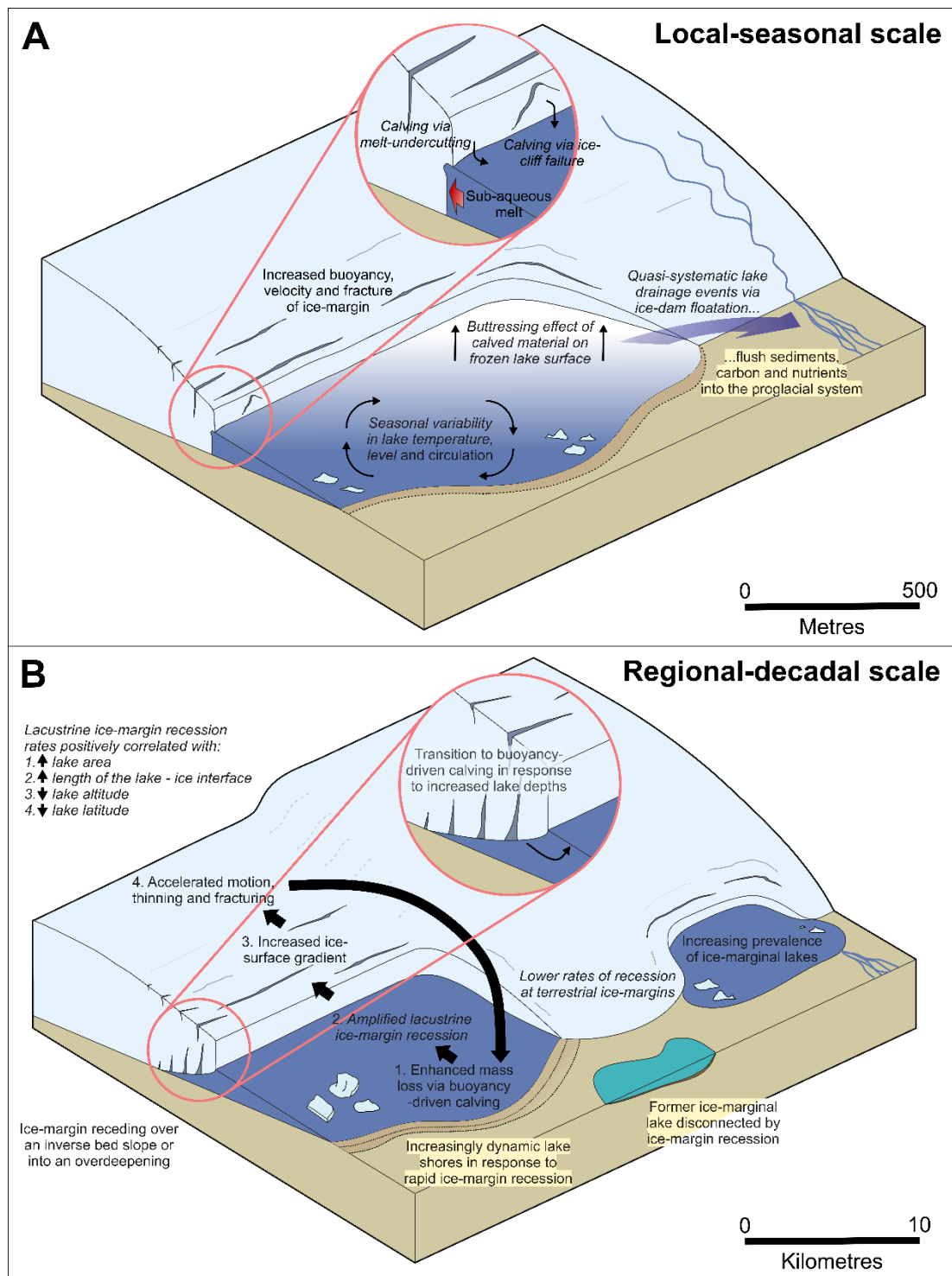


Figure 7.1. Conceptual diagram illustrating the key impacts of ice-marginal lakes on the ice-margin dynamics of the GrIS at (a) a local-seasonal scale and (b) a regional-decadal scale. Impacts observed and/or quantified in this thesis are italicised. Note exaggerated vertical scale for illustrative purposes.

#### 7.4.1 LOCAL-SEASONAL SCALE PRIORITIES

Given the increasing prevalence of ice-marginal lakes in many of the world's glacierised regions, a key research priority is further constraining the processes of subaqueous melt and calving that drive mass loss from lacustrine termini. This is particularly pertinent given the emergent hypothesis in Chapter 6 that continued atmospheric warming is likely to both increase lake water temperatures and extend the melt season, thereby enhancing and prolonging the operation of melt-undercutting at lacustrine termini. Furthermore, the relatively few studies that have considered the effects of frontal ablation in a lacustrine setting have failed to reach a consensus regarding the relative contribution of subaqueous melt to overall mass loss. Subaqueous melt rates are primarily controlled by the temperature and circulation of proglacial water bodies (Truffer and Motyka, 2016), but these variables are often inadequately quantified in lacustrine settings. For example, there can be considerable heterogeneity in lake temperature and circulation, particularly between the proximal and distal shores of lakes in contact with an ice-margin (Haresign and Warren, 2005), yet existing studies typically record water temperatures at either a solitary point (e.g. Boyce et al. 2007; Minowa et al. 2017), or interpolate temperatures from a sparse set of isolated data points (e.g. Sugiyama et al., 2016). Future studies could therefore improve consideration of spatial variability in ice-marginal lake temperatures, and thus subaqueous melt, through the use of currently underutilised remote sensing techniques, such as the thermal infrared bands of the ASTER and Landsat satellites (e.g. Watson et al., 2020), or the mounting of thermal imaging cameras to airborne platforms (e.g. Webster et al., 2017). It should be noted however, that these approaches will still need to be paired with field observations (e.g. the use of thermistor chains) for validation purposes and to quantify variability in water temperatures with lake depth. Finally, subaqueous melt rates are typically inferred from water temperatures due to the inherent dangers of measuring undercut or thermo-erosional notch propagation directly (e.g. Röhl, 2006). However, the recent use of side-scanning sonars fitted to motorboats has successfully captured the subaqueous geometry of both marine and lacustrine ice-margins (e.g. Rignot et al., 2015; Sugiyama et al., 2019), thereby illustrating the considerable potential of repeat sonar surveys for quantifying the evolution of undercuts and thermo-erosional notches, particularly if proximity to the ice-front can be improved by fitting the sonar to a remotely operated boat (e.g. Yamasaki et al., 2017).

The time-lapse camera array employed in Chapters 5 and 6 has significant potential for the continued investigation and quantification of calving processes. In particular, further

monitoring and characterisation of calving events at both lacustrine and marine termini could provide the basis of a standardised classification system for calving processes, thereby facilitating the direct comparison of calving activity across a range of ice-marginal environments and thus reducing the need for study- and site-specific calving criteria (e.g. Warren et al., 1995b; Medrzycka et al., 2016; Minowa et al., 2018; How et al., 2019). Such an approach would also provide a strengthened foundation for linking calving rates and processes to local environmental controls, including terminus geometry, bathymetry and water temperature. Furthermore, fine spatio-temporal resolution volumetric datasets of calving activity from a diverse range of sites would be well-suited to the parameterisation and validation of calving laws derived from the new generation of discrete element models (e.g. Åström et al., 2013; Benn et al., 2017).

The efficiency and versatility of time-lapse camera array based studies of calving processes are also likely to be considerably enhanced in coming years as algorithms for automating key stages of the SfM-MVS and point cloud workflow become increasingly available. For example, the automated detection of morphometric change via sequential image analysis (e.g. Vallot et al., 2019) or point cloud cluster analysis (e.g. Tonini and Abellan, 2014) could considerably reduce manual processing requirements and, if coupled with remote transmission of imagery, ultimately permit the investigation of calving activity in real-time and at the event scale. In addition, time-lapse based research approaches also provide a valuable opportunity to integrate calving analyses into a broader suite of glaciological measurements and thereby assess the coupling between dynamic processes at lacustrine ice-margins. For example, the derivation of horizontal and vertical velocity components of glacier termini from oblique time-lapse image sequences (e.g. James et al., 2016; How et al., 2020), could elucidate the relationships between calving activity and the velocity and buoyancy of an ice-margin.

#### 7.4.2 REGIONAL-DECADAL SCALE PRIORITIES

Three primary themes emerge from this thesis as future priorities for continuing research into the impacts of ice-marginal lakes on the ice-margin dynamics of the GrIS at a regional-decadal scale. The first concerns the broader dynamic response of the ice sheet to ice-marginal lake formation and expansion. Although Chapter 4 demonstrated that the lacustrine margins of the GrIS retreated faster than their terrestrial counterparts between 1987-2015, the causal connections between ice-marginal lake prevalence and enhanced ice-

margin recession could only be hypothesised in the absence of data concerning wider ice-margin dynamics. In particular, analyses of changes in velocity, structure and ice-surface elevation up-ice of lacustrine termini of the GrIS are necessary to fully elucidate the mechanisms and feedbacks by which lakes drive enhanced rates of ice-margin recession. For example, King et al. (2018) used a 15-year time-series of DEMs and optical satellite archives to conduct a comparative analysis of dynamic change at terrestrial and lacustrine terminating glaciers in the Himalaya, and found that many lacustrine terminating glaciers could be distinguished from their terrestrial counterparts by their increased surface velocities, enhanced surface thinning and increased surface gradients. Similar analyses at the margins of the GrIS could be conducted using the extensive archival datasets, including DEMs (e.g. Korsgaard et al., 2016; Porter et al., 2018) and optical satellite imagery (see Table 3.1), that are already in the public domain and frequently span multiple decades. Furthermore, determining the volumetric response of the ice sheet to ice-marginal lake formation and expansion, particularly the extent of surface thinning up-ice of the terminus, is integral to refining the contribution of the GrIS to sea level rise.

Secondly, the increased ice-marginal lake temperatures and extension of the melt season in response to atmospheric warming hypothesised in Chapters 4 and 6 could be investigated using the thermal infrared bands of existing optical satellite sensors. For example, Watson et al. (2020) employed a time-series of thermal data from the Landsat and ASTER sensors to explore seasonal variability in the ice cover regime and temperature of several ice-marginal lakes in the Himalaya. The availability of Landsat thermal data products extending back to the 1980s (Table 3.1), coupled with the increasing automation of the associated workflow (e.g. Parastatidis et al., 2017), therefore provides an ideal opportunity to not only quantify seasonal variability in the ice cover regime and temperature of specific ice-marginal lakes in Greenland, but to also conduct a regional scale longitudinal study of ice-marginal lake temperatures spanning multiple decades. In addition, the corresponding dataset would also facilitate the investigation of associations between lake temperature, lake properties and ice-margin dynamics.

Finally, projecting ice-marginal lake evolution at the margin of the GrIS in both the short- and long-term is increasingly necessary to understand the future extent of lacustrine forcing on ice-margin dynamics, and thus rates of mass loss, at the ice sheet. In particular, sections of the ice-margin that possess favourable properties for lake formation in the short-term could

be determined by the application of morphometric and dynamic criteria, similar to those employed to forecast ice-marginal lake formation in the Himalaya (Reynolds, 2000; Quincey et al., 2007). However, longer-term projections of ice-marginal lake evolution are likely to require a more complex integration of high-resolution maps of GrIS bed topography (e.g. Lindback et al., 2014; Morlighem et al., 2017) with simulated ice sheet extents at a range of timescales and parameterised for a variety of climate warming scenarios (e.g. Aschwanden et al., 2018).

#### 7.4.3 THEORETICAL APPROACHES

A comprehensive understanding of the effects of lacustrine forcing at the margin of the GrIS is necessary if ice sheet evolution, dynamics, mass loss, and contributions to sea level rise, are to be accurately quantified. However, to date disparities in the spatio-temporal coverage of datasets acquired through field-based observations and remote sensing analyses have restricted the process-understanding of lacustrine ice-margin dynamics. In particular, quantitative field observations of ice-margin dynamics are frequently characterised by limited spatial and/or temporal coverage, whereas remote sensing analyses, although well-suited to documenting dynamic change at a regional-decadal scale, are less suited to isolating the mechanisms and drivers of change. Theoretical approaches therefore have significant potential to bridge the spatio-temporal disparities between field and remote sensing observations, and thus improve the process-understanding of lacustrine ice-margin dynamics at a broad range of spatial and temporal scales. For example, Tsutaki et al. (2019) recently employed a two-dimensional flow model to simulate the impacts of ice-marginal lakes on the flow regimes and mass loss of Himalayan glaciers, and both Berends and van de Wal (2016) and Hinck et al. (2020) have coupled topographic datasets with advances in flood-fill algorithms to model the extent and depth of ice-marginal lakes at the margin of the Laurentide Ice Sheet during deglaciation. However, beyond these isolated examples, the vast majority of glacier and ice sheet models have continued to omit the effects of ice-marginal lakes on ice-margin dynamics, and may therefore underestimate both rates of mass loss and sea level rise contributions from lacustrine terminating ice masses. This omission partially arises from the challenges associated with constraining the considerable spatio-temporal variability in boundary conditions at lake terminating ice-margins (e.g. lake and glacier extent, lake level, lake temperature), but also from the sparsity of quantitative datasets available to parameterise and validate models of ice-marginal processes, such as subaqueous melt and calving. However, continued efforts to quantify ice-marginal processes using field-



and remote sensing-based observations are strengthening the empirical foundation upon which theoretical approaches can enhance process-understanding of lacustrine ice-margin dynamics at a broad range of spatial and temporal scales. Consequently, a key research priority for the GrIS should be the integration of lacustrine forcing into ice sheet models in order to refine projections of ice sheet dynamics and its contribution to sea level rise in both the short- and long-term.

#### 7.4.4 BROADER APPLICATIONS OF THE TIME-LAPSE CAMERA ARRAY

In addition to the monitoring and quantification of calving activity, the time-lapse camera array developed in Chapter 5 has potential for a number of broader cryospheric and geomorphological applications. In particular, time-lapse camera array setups are well-suited to the detection and quantification of topographic change in settings where relatively slow or unpredictable environmental processes necessitate extended monitoring campaigns. For example, since the publication of Mallalieu et al. (2017) the integrated time-lapse SfM-MVS methodology has been adopted in other studies for a range of such purposes, including: the quantification of seasonal slump activity in thermokarst (Armstrong et al., 2018); the measurement of snow depths throughout a winter season (Filhol et al., 2019); and the monitoring of slope stability (Parente et al., 2019). Furthermore, the time-lapse camera array also has potential to be deployed as a novel tool for the prediction, monitoring and early warning of a range of environmental hazards. For example, monoscopic timelapse camera installations are increasingly being used in populated mountain regions to monitor ice-marginal lakes for the rapid changes in lake level that often mark the onset of a GLOF (e.g. Mulsow et al., 2015; Carvallo et al. 2017). However, the use of such monoscopic setups to alert downstream communities to GLOF events is highly vulnerable to camera redundancy, either through equipment failure or by transient objects (e.g. icebergs, animals, vegetation) obscuring the camera's view of the lake level. The alternative installation of a time-lapse camera array setup could reduce the vulnerability of the alert system to camera redundancy and capture valuable volumetric records of geomorphological change associated with GLOF events, potentially revealing the mechanisms and drivers of the GLOF itself. Furthermore, if the remote-transmission of camera imagery and full automation of the SfM-MVS workflow were realised, the time-lapse camera array setup could conceivably provide extended notice of GLOF events by hours or days via the early detection of ice-marginal processes that can trigger GLOFs, such as increased ice-margin buoyancy or high-magnitude calving events into the lake. Finally, fully automated time-lapse camera installations may also provide an

affordable alternative to the ground-based TLS and radar systems commonly employed to monitor real-time deformation in unstable rock slopes (e.g. Kromer et al., 2017; Ferrigno et al., 2017).

## **7.5 CONCLUSIONS**

This thesis has presented the first quantitative assessment of the impact of ice-marginal lakes on the ice-margin dynamics of the GrIS. Specifically, the role of lacustrine forcing on ice-margin dynamics has been investigated at multiple spatial and temporal scales through a combination of established remote sensing analyses and novel field-based time-lapse photography.

A regional-decadal scale analysis of changes in the extent of the ice sheet margin in western Greenland revealed that lacustrine margins receded faster than their terrestrial counterparts between 1987 and 2015. In addition, mean annual recession rates at lacustrine margins increased by an order of magnitude over the duration of the survey, and increasingly outpaced recession at terrestrial margins. A number of lake parameters, including lake latitude, altitude, area and the length of the lake – ice-margin interface, were also found to be significantly correlated with rates of lacustrine ice-margin change. The results demonstrate that ice-marginal lakes act as key controls on rates and spatial patterns of mass loss from the GrIS, and are likely to further grow in importance in response to anticipated increases in the prevalence and extent of ice-marginal lakes in western Greenland.

A local-seasonal scale analysis of calving at a lacustrine terminating margin of the GrIS identified distinct seasonality in calving rates and processes. In particular, high calving rates were driven by melt-undercutting at the ice-cliff during ice-free lake conditions, whereas force imbalances at the ice-cliff promoted lower calving rates when the lake was frozen. The recognition of distinct calving regimes is significant because existing volumetric analyses of calving processes commonly omit consideration of seasonality. Furthermore, lengthening summer seasons in response to atmospheric warming are likely to amplify future rates of mass loss from lacustrine margins due to the extended longevity of high-magnitude calving processes.

The integration of time-lapse photography with SfM-MVS techniques has been demonstrated to be an effective method for the extended acquisition of fine spatio-temporal

resolution datasets of ice-margin topography, and thus the investigation of ice-margin dynamics at both the seasonal- and event-scale. Furthermore, the integrated time-lapse SfM-MVS method has considerable potential for deployment in a wide range of non-glacial environments to detect and quantify geomorphological change.

Finally, this research has illustrated the impacts of lacustrine forcing on the ice-margin dynamics of the GrIS, and is particularly pertinent given anticipated increases in ice-margin recession and mass loss in coming decades in response to continued ice-marginal lake expansion and a lengthening melt season. In addition, the quantitative data derived through this study provide an empirical foundation upon which modelling efforts can incorporate the influence of ice-marginal processes.

## References

- Abdalati W., Krabill W., Frederick E., Manizade S., Martin C., Sonntag J., Swift R., Thomas R., Wright W. and Yungel J. 2001. Outlet glacier and margin elevation changes: Near-coastal thinning of the Greenland ice sheet. *Journal of Geophysical Research: Atmospheres*. **106**, pp.33729-33741.
- Abellán A., Oppikofer T., Jaboyedoff M., Rosser N.J., Lim M. and Lato M.J. 2014. Terrestrial laser scanning of rock slope instabilities. *Earth Surface Processes and Landforms*. **39**, pp.80-97.
- Aggarwal A., Jain S.K., Lohani A.K. and Jain N. 2016. Glacial lake outburst flood risk assessment using combined approaches of remote sensing, GIS and dam break modelling. *Geomatics Natural Hazards & Risk*. **7**, pp.18-36.
- Amundson J.M., Fahnestock M., Truffer M., Brown J., Lüthi M.P. and Motyka R.J. 2010. Ice mélange dynamics and implications for terminus stability, Jakobshavn Isbræ, Greenland. *Journal of Geophysical Research: Earth Surface*. **115**, F01005.
- Anderson K., Westoby M.J. and James M.R. 2019. Low-budget topographic surveying comes of age: Structure from motion photogrammetry in geography and the geosciences. *Progress in Physical Geography: Earth and Environment*. **43**, pp.163-173.
- Anderson N.J., Saros J.E., Bullard J.E., Cahoon S.M.P., McGowan S., Bagshaw E.A., Barry C.D., Bindler R., Burpee B.T., Carrivick J.L., Fowler R.A., Fox A.D., Fritz S.C., Giles M.E., Hamerlik L., Ingeman-Nielsen T., Law A.C., Mernild S.H., Northington R.M., Osburn C.L., Pla-Rabès S., Post E., Telling J., Stroud D.A., Whiteford E.J., Yallop M.L. and Yde J.C. 2017. The Arctic in the Twenty-First Century: Changing Biogeochemical Linkages across a Paraglacial Landscape of Greenland. *BioScience*. **67**, pp.118-133.
- Anderson R.S., Walder J.S., Anderson S.P., Trabant D.C. and Fountain A.G. 2005. The dynamic response of Kennicott Glacier, Alaska, USA, to the Hidden Creek Lake outburst flood. *Annals of Glaciology*. **40**, pp.237-242.
- Anderson S.P., Walder J.S., Anderson R.S., Kraal E.R., Cunico M., Fountain A.G. and Trabant D.C. 2003. Integrated hydrologic and hydrochemical observations of Hidden Creek Lake jokulhlaups, Kennicott Glacier, Alaska. *Journal of Geophysical Research: Earth Surface*. **108**, 6003.
- Andreassen L.M., Paul F., Kaab A. and Hausberg J.E. 2008. Landsat-derived glacier inventory for Jotunheimen, Norway, and deduced glacier changes since the 1930s. *The Cryosphere*. **2**, pp.131-145.

- Armstrong W.H. and Anderson R.S. 2020. Ice-marginal lake hydrology and the seasonal dynamical evolution of Kennicott Glacier, Alaska. *Journal of Glaciology*. **67**, pp.1-15.
- Armstrong L., Lacelle D., Fraser R.H., Kokelj S. and Knudby A. 2018. Thaw slump activity measured using stationary cameras in time-lapse and Structure-from-Motion photogrammetry. *Arctic Science*. **4**, pp.827-845.
- Arp C.D., Jones B.M., Whitman M., Larsen A. and Urban F.E. 2010. Lake temperature and ice cover regimes in the Alaskan Subarctic and Arctic: Integrated monitoring, remote sensing, and modeling. *Journal of the American Water Resources Association*. **46**, pp.777-791.
- Aschwanden A., Fahnestock M.A., Truffer M., Brinkerhoff D.J., Hock R., Khroulev C., Mottram R. and Khan S.A. 2019. Contribution of the Greenland Ice Sheet to sea level over the next millennium. *Science Advances*. **5**, eaav9396.
- Åström J.A., Riikilä T.I., Tallinen T., Zwinger T., Benn D., Moore J.C. and Timonen J. 2013. A particle based simulation model for glacier dynamics. *The Cryosphere*. **7**, pp.1591-1602.
- Bamber J.L., Westaway R.M., Marzeion B. and Wouters B. 2018. The land ice contribution to sea level during the satellite era. *Environmental Research Letters*. **13**, 063008.
- Basnett S., Kulkarni A.V. and Bolch T. 2013. The influence of debris cover and glacial lakes on the recession of glaciers in Sikkim Himalaya, India. *Journal of Glaciology*. **59**, pp.1035-1046.
- Bates D., Machler M., Bolker B.M. and Walker S.C. 2015. Fitting Linear Mixed-Effects Models Using lme4. *Journal of Statistical Software*. **67**, pp.1-48.
- Baurley N.R., Robson B.A. and Hart J.K. 2020. Long-term impact of the proglacial lake Jökulsárlón on the flow velocity and stability of Breiðamerkurjökull glacier, Iceland. *Earth Surface Processes and Landforms*. esp.4920.
- Bemis S.P., Micklethwaite S., Turner D., James M.R., Akciz S., Thiele S.T. and Bangash H.A. 2014. Ground-based and UAV-Based photogrammetry: A multi-scale, high-resolution mapping tool for structural geology and paleoseismology. *Journal of Structural Geology*. **69**, Part A, pp.163-178.
- Benn D.I., Åström J.a.N., Zwinger T., Todd J.O.E., Nick F.M., Cook S., Hulton N.R.J. and Luckman A. 2017. Melt-under-cutting and buoyancy-driven calving from tidewater glaciers: new insights from discrete element and continuum model simulations. *Journal of Glaciology*. **63**, pp.691-702.
- Benn D.I., Warren C.R. and Mottram R.H. 2007. Calving processes and the dynamics of calving glaciers. *Earth-Science Reviews*. **82**, pp.143-179.

Bennett M.R., Hambrey M.J., Huddart D., Classer N.F. and Crawford K. 1998. The ice-dammed lakes of Ossian Sarsfjellet (Svalbard): Their geomorphology and significance. *Boreas*. **27**, pp.25-43.

Berends C. J. and van de Wal R.S.W: A computationally efficient depression-filling algorithm for digital elevation models, applied to proglacial lake drainage. *Geoscientific Model Development*. **9**, pp.4451-4460.

Bernard E., Friedt J.M., Tolle F., Marlin C. and Griselin, M. 2017. Using a small COTS UAV to quantify moraine dynamics induced by climate shift in Arctic environments. *International Journal of Remote Sensing*. **38**, pp.2480-2494.

Bevan S.L., Luckman A.J. and Murray T. 2012. Glacier dynamics over the last quarter of a century at Helheim, Kangerdlugssuaq and 14 other major Greenland outlet glaciers. *The Cryosphere*. **6**, pp.923-937.

Bevis M., Harig C., Khan S.A., Brown A., Simons F.J., Willis M., Fettweis X., Van Den Broeke M.R., Madsen F.B., Kendrick E., Caccamise D.J., Van Dam T., Knudsen P. and Nylén T. 2019. Accelerating changes in ice mass within Greenland, and the ice sheet's sensitivity to atmospheric forcing. *Proceedings of the National Academy of Sciences*. **116**, pp.1934-1939.

Bhattacharya I., Jezek K.C., Wang L. and Liu H. 2009. Surface melt area variability of the Greenland ice sheet: 1979–2008. *Geophysical Research Letters*. **36**, L20502.

Bindschadler R. 1983. The importance of pressurized subglacial water in separation and sliding at the glacier bed. *Journal of Glaciology*. **29**, pp.3-19.

Bjørk A.A., Aagaard S., Lutt A., Khan S.A., Box J.E., Kjeldsen K.K., Larsen N.K., Korsgaard N.J., Cappelen J., Colgan W.T., Machguth H., Andresen C.S., Peings Y. and Kjaer K.H. 2018. Changes in Greenland's peripheral glaciers linked to the North Atlantic Oscillation. *Nature Climate Change*. **8**, pp.48-52.

Bjørk A.A., Kjær K.H., Korsgaard N.J., Khan S.A., Kjeldsen K.K., Andresen C.S., Box J.E., Larsen N.K. and Funder S. 2012. An aerial view of 80 years of climate-related glacier fluctuations in southeast Greenland. *Nature Geoscience*. **5**, pp.427-432.

Bolch T., Peters J., Yegorov A., Pradhan B., Buchroithner M. and Blagoveshchensky V. 2011. Identification of potentially dangerous glacial lakes in the northern Tien Shan. *Natural Hazards*. **59**, pp.1691-1714.

Boyce E.S., Motyka R.J. and Truffer M. 2007. Flotation and retreat of a lake-calving terminus, Mendenhall Glacier, Southeast Alaska, USA. *Journal of Glaciology*. **53**, pp.211-224.

Brasington J., Langham J. and Rumsby B. 2003. Methodological sensitivity of morphometric estimates of coarse fluvial sediment transport. *Geomorphology*. **53**, pp.299-316.

Brun F., Wagnon P., Berthier E., Jomelli V., Maharjan S.B., Shrestha F. and Kraaijenbrink P.D.A. 2019. Heterogeneous Influence of Glacier Morphology on the Mass Balance Variability in High Mountain Asia. *Journal of Geophysical Research: Earth Surface*. **124**, pp.1331-1345.

Buckel J., Otto J.C., Prasicek G. and Keuschnig M. 2018. Glacial lakes in Austria - Distribution and formation since the Little Ice Age. *Global and Planetary Change*. **164**, pp.39-51.

Carr J.R., Stokes C.R. and Vieli A. 2013. Recent progress in understanding marine-terminating Arctic outlet glacier response to climatic and oceanic forcing: Twenty years of rapid change. *Progress in Physical Geography: Earth and Environment*. **37**, pp.436-467.

Carrivick J.L. and Quincey D.J. 2014. Progressive increase in number and volume of ice-marginal lakes on the western margin of the Greenland Ice Sheet. *Global and Planetary Change*. **116**, pp.156-163.

Carrivick J.L., Smith M.W. and Quincey D.J. 2016. *Structure from Motion in the Geosciences*. Chichester: Wiley Blackwell.

Carrivick J.L., Turner A.G.D., Russell A.J., Ingeman-Nielsen T. and Yde J.C. 2013. Outburst flood evolution at Russell Glacier, western Greenland: effects of a bedrock channel cascade with intermediary lakes. *Quaternary Science Reviews*. **67**, pp.39-58.

Carrivick J.L. and Tweed F.S. 2013. Proglacial lakes: character, behaviour and geological importance. *Quaternary Science Reviews*. **78**, pp.34-52.

Carrivick J.L. and Tweed F.S. 2016. A global assessment of the societal impacts of glacier outburst floods. *Global and Planetary Change*. **144**, pp.1-16.

Carrivick J.L. and Tweed F.S. 2019. A review of glacier outburst floods in Iceland and Greenland with a megafloods perspective. *Earth-Science Reviews*. **196**, 102876.

Carrivick J.L., Tweed F.S., Ng F., Quincey D.J., Mallalieu J., Ingeman-Nielsen T., Mikkelsen A.B., Palmer S.J., Yde J.C., Homer R., Russell A.J. and Hubbard A. 2017a. Ice-Dammed Lake Drainage Evolution at Russell Glacier, West Greenland. *Frontiers in Earth Science*. **5**, 2017.00100.

Carrivick J.L., Yde J.C., Knudsen N.T. and Kronborg C. 2018. Ice-dammed lake and ice-margin evolution during the Holocene in the Kangerlussuaq area of west Greenland. *Arctic, Antarctic, and Alpine Research*. **50**, e1420854.

Carrivick J.L., Yde J.C., Russell A.J., Quincey D.J., Ingeman-Nielsen T. and Mallalieu J. 2017b. Ice-margin and meltwater dynamics during the mid-Holocene in the Kangerlussuaq area of west Greenland. *Boreas*. **46**, pp.369-387.

- Carvalho R., Llanos P., Noceti R. and Casassa G. 2017. Real-time transmission of time-lapse imagery of glaciers in the southern Andes. In: *2017 First IEEE International Symposium of Geoscience and Remote Sensing (GRSS-CHILE), 15-16 June 2017, Valdivia, Chile*. New York City: IEEE, pp.1-3.
- Cassotto R., Fahnestock M., Amundson J.M., Truffer M. and Joughin I. 2015. Seasonal and interannual variations in ice melange and its impact on terminus stability, Jakobshavn Isbræ, Greenland. *Journal of Glaciology*. **61**, pp.76-88.
- Catania G.A., Stearns L.A., Sutherland D.A., Fried M.J., Bartholomaeus T.C., Morlighem M., Shroyer E. and Nash J. 2018. Geometric Controls on Tidewater Glacier Retreat in Central Western Greenland. *Journal of Geophysical Research: Earth Surface*. **123**, pp.2024-2038.
- Chambers J.R., Smith M.W., Quincey D.J., Carrivick J.L., Ross A.N. and James M.R. 2020. Glacial Aerodynamic Roughness Estimates: Uncertainty, Sensitivity, and Precision in Field Measurements. *Journal of Geophysical Research: Earth Surface*. **125**, F005167.
- Chandler D.M., Waller R.I. and Adam W.G. 2005. Basal ice motion and deformation at the ice-sheet margin, West Greenland. *Annals of Glaciology*. **42**, pp.67-70.
- Chapuis A. and Tetzlaff T. 2014. The variability of tidewater-glacier calving: origin of event-size and interval distributions. *Journal of Glaciology*. **60**, pp.622-634.
- Chernos M., Koppe, M. and Moore R.D. 2016. Ablation from calving and surface melt at lake-terminating Bridge Glacier, British Columbia, 1984–2013. *The Cryosphere*. **10**, pp.87-102.
- Chen X.Q., Cui P., Li Y., Yang Z. and Qi Y.Q. 2007. Changes in glacial lakes and glaciers of post-1986 in the Poiqu River basin, Nyalam, Xizang (Tibet). *Geomorphology*. **88**, pp.298-311.
- Chinn T.J. 1996. New Zealand glacier responses to climate change of the past century. *New Zealand Journal of Geology and Geophysics*. **39**, pp.415-428.
- Chinn T.J. 1999. New Zealand glacier response to climate change of the past 2 decades. *Global and Planetary Change*. **22**, pp.155-168.
- Christoffersen P., Mugford R.I., Heywood K.J., Joughin I., Dowdeswell J.A., Syvitski J.P.M., Luckman A. and Benham T.J. 2011. Warming of waters in an East Greenland fjord prior to glacier retreat: mechanisms and connection to large-scale atmospheric conditions. *The Cryosphere*. **5**, pp.701-714.
- Chudley T.R., Christoffersen P., Doyle S.H., Abellan A. and Snooke N. 2019. High-accuracy UAV photogrammetry of ice sheet dynamics with no ground control. *The Cryosphere*. **13**, pp.955-968.



Church J.A., Clark P.U., Cazenave A., Gregory J.M., Jevrejeva S., Levermann A., Merrifield M.A., Milne G.A., Nerem R.S., Nunn P.D., Payne A.J., Pfeffer W.T., Stammer D. and Unnikrishnan A.S. 2013. Sea Level Change. In: Stocker T.F., Qin D., Plattner G.K., Tignor M., Allen S.K., Boschung J., Nauels A., Xia Y., Bex V. and Midgley P.M. eds. *Climate Change 2013: The Physical Science Basis. Contribution of Working Group I to the Fifth Assessment Report of the Intergovernmental Panel on Climate Change*. Cambridge, Cambridge University Press, pp. 1137-1216.

Citterio M., Paul F., Ahlstrom A.P., Jepsen H.F. and Weidick A. 2009. Remote sensing of glacier change in West Greenland: accounting for the occurrence of surge-type glaciers. *Annals of Glaciology*. **50**, pp.70-80.

Clague J.J. and Evans S.G. 2000. A review of catastrophic drainage of moraine-dammed lakes in British Columbia. *Quaternary Science Reviews*. **19**, pp.1763-1783.

Clement P. 1984. The drainage of a marginal ice-dammed lake at Nordbogletscher, Johan-Dahl-Land, South Greenland. *Arctic and Alpine Research*. **16**, pp.209-216.

CloudCompare v.2.7. 2016. GPL software, retrieved from <http://www.cloudcompare.org>. [Accessed 7 August 2016].

Costa J.E. and Schuster R.L. 1988. The formation and failure of natural dams. *Geological Society of America Bulletin*. **100**, pp.1054-1068.

Danielson B. and Sharp M. 2013. Development and application of a time-lapse photograph analysis method to investigate the link between tidewater glacier flow variations and supraglacial lake drainage events. *Journal of Glaciology*. **59**, pp.287-302.

Davies B.J., Carrivick J.L., Glasser N.F., Hambrey M.J. and Smellie J.L. 2012. Variable glacier response to atmospheric warming, northern Antarctic Peninsula, 1988–2009. *The Cryosphere*. **6**, pp.1031-1048.

Deems J.S., Painter T.H. and Finnegan D.C. 2013. Lidar measurement of snow depth: a review. *Journal of Glaciology*. **59**, pp.467-479.

Deline P., Diolaiuti G., Kirkbride M.P., Mortara G., Pavan M., Smiraglia C. and Tamburini A. 2004. Drainage of ice-contact Miage Lake (Mont Blanc Massif, Italy) in September 2004. *Geografia Fisica e Dinamica Quaternaria*. **27**, pp.113-119.

Dell R., Carr R., Phillips E. and Russell A.J. 2019. Response of glacier flow and structure to proglacial lake development and climate at Fjallsjokull, south-east Iceland. *Journal of Glaciology*. **65**, pp.321-336.

Demidov I.N., Houmark-Nielsen M., Kjaer K.H. and Larsen E. 2006. The last Scandinavian Ice Sheet in northwestern Russia: ice flow patterns and decay dynamics. *Boreas*. **35**, pp.425-443.

- Ding Q., Wallace J.M., Battisti D.S., Steig E.J., Gallant A.J.E., Kim H. and Geng, L. 2014. Tropical forcing of the recent rapid Arctic warming in northeastern Canada and Greenland. *Nature*. **509**, pp.209-212.
- Diolaiuti G., Citterio M., Carnielli T., D'agata C., Kirkbride M. and Smiraglia C. 2006. Rates, processes and morphology of freshwater calving at Miage Glacier (Italian Alps). *Hydrological Processes*. **20**, pp.2233-2244.
- Dormann C.F., Elith J., Bacher S., Buchmann C., Carl G., Carre G., Marquez J.R.G., Gruber B., Lafourcade B., Leitao P.J., Munkemuller T., McClean C., Osborne P.E., Reineking B., Schroder B., Skidmore A.K., Zurell D. and Lautenbach S. 2013. Collinearity: a review of methods to deal with it and a simulation study evaluating their performance. *Ecography*. **36**, pp.27-46.
- Dubey S. and Goyal M.K. 2020. Glacial lake outburst flood hazard, downstream impact, and risk over the Indian Himalayas. *Water Resources Research*. **56**, e2019WR026533.
- Duck R.W. and Mcmanus J. 1985. Short-term bathymetric changes in an ice-contact proglacial lake. *Norsk Geografisk Tidsskrift*. **39**, pp.39-45.
- Duguay C.R., Prowse T.D., Bonsal B.R., Brown R.D., Lacroix M.P. and Menard P. 2006. Recent trends in Canadian lake ice cover. *Hydrological Processes*. **20**, pp.781-801.
- Dykes R.C. and Brook M.S. 2010. Terminus recession, proglacial lake expansion and 21st century calving retreat of Tasman Glacier, New Zealand. *New Zealand Geographer*. **66**, pp.203-217.
- Dykes R.C., Brook M.S., Robertson C.M. and Fuller I.C. 2011. Twenty-First Century Calving Retreat of Tasman Glacier, Southern Alps, New Zealand. *Arctic, Antarctic and Alpine Research*. **43**, pp.1-10.
- Eijpen K.J., Warren C.R. and Benn D.I. 2003. Subaqueous melt rates at calving termini: a laboratory approach. *Annals of Glaciology*. **36**, pp.179-183.
- Eiken T. and Sund M. 2012. Photogrammetric methods applied to Svalbard glaciers: accuracies and challenges. *Polar Research*. **31**, 18671.
- Eltner A., Kaiser A., Abellán A. and Schindewolf M. 2017. Time lapse structure-from-motion photogrammetry for continuous geomorphic monitoring. *Earth Surface Processes and Landforms*. **42**, pp.2240-2253.
- Eltner A., Kaiser A., Castillo C., Rock G., Neugirg F. and Abellán A. 2016. Image-based surface reconstruction in geomorphometry – merits, limits and developments. *Earth Surface Dynamics*. **4**, pp.359-389.

Emmer A., Harrison S., Mergili M., Allen S., Frey H. and Huggel C. 2020. 70 years of lake evolution and glacial lake outburst floods in the Cordillera Blanca (Peru) and implications for the future. *Geomorphology*. **365**, 107178.

Engel Z., Sobr M. and Yerokhin S.A. 2012. Changes of Petrov glacier and its proglacial lake in the Akshirak massif, central Tien Shan, since 1977. *Journal of Glaciology*. **58**, pp.388-398.

Evans S.G. and Clague J.J. 1994. Recent climatic-change and catastrophic geomorphic processes in mountain environments. *Geomorphology*. **10**, pp.107-128.

Fausto R.S. and van As D. 2019 Programme for monitoring of the Greenland ice sheet (PROMICE): Automatic weather station data version: v03. *Geological Survey of Denmark and Greenland*. [Online]. [Accessed 5 January 2020]. Available from: <http://www.promice.org/PromiceDataPortal/>

Ferrigno F., Gigli G., Fanti R., Intrieri E. and Casagli N. 2017. GB-InSAR monitoring and observational method for landslide emergency management: the Montaguto earthflow (AV, Italy). *Natural Hazards and Earth System Sciences*. **17**, pp.845-860.

Filhol S., Perret A., Girod L., Sutter G., Schuler T.V. and Burkhart J.F. 2019. Time-Lapse Photogrammetry of Distributed Snow Depth During Snowmelt. *Water Resources Research*. **55**, pp.7916-7926.

Fischer M., Huss M., Kummert M. and Hoelzle M. 2016. Application and validation of long-range terrestrial laser scanning to monitor the mass balance of very small glaciers in the Swiss Alps. *The Cryosphere*. **10**, pp.1279-1295.

Fonstad M.A., Dietrich J.T., Courville B.C., Jensen J.L. and Carbonneau P.E. 2013. Topographic structure from motion: a new development in photogrammetric measurement. *Earth Surface Processes and Landforms*. **38**, pp.421-430.

Franco B., Fettweis X. and Ericum M. 2013. Future projections of the Greenland ice sheet energy balance driving the surface melt. *The Cryosphere*. **7**, pp.1-18.

Funk M. and Rothlisberger H. 1989. Forecasting the effects of a planned reservoir which will partially flood the the tongue of Unteraargletscher in Switzerland. *Annals of Glaciology*. **13**, pp.76-81.

Furuya M. and Wahr J.M. 2005. Water level changes at an ice-dammed lake in west Greenland inferred from InSAR data. *Geophysical Research Letters*. **32**, L14501.

Gabbud C., Micheletti N. and Lane S.N. 2015. Lidar measurement of surface melt for a temperate Alpine glacier at the seasonal and hourly scales. *Journal of Glaciology*. **61**, pp.963-974.

- Gardelle J., Arnaud Y. and Berthier E. 2011. Contrasted evolution of glacial lakes along the Hindu Kush Himalaya mountain range between 1990 and 2009. *Global and Planetary Change*. **75**, pp.47-55.
- Geirsdottir A., Miller G.H., Wattrus N.J., Bjornsson H. and Thors K. 2008. Stabilization of glaciers terminating in closed water bodies: Evidence and broader implications. *Geophysical Research Letters*. **35**, L17502.
- Gienko G.A. and Terry J.P. 2014. Three-dimensional modeling of coastal boulders using multi-view image measurements. *Earth Surface Processes and Landforms*. **39**, pp.853-864.
- Gillet-Chaulet F., Gagliardini O., Seddik H., Nodet M., Durand G., Ritz C., Zwinger T., Greve R. and Vaughan D.G. 2012. Greenland ice sheet contribution to sea-level rise from a new-generation ice-sheet model. *The Cryosphere*. **6**, pp.1561-1576.
- Girod L., Nielsen N.I., Couderette F., Nuth C. and Kaab, A. 2018. Precise DEM extraction from Svalbard using 1936 high oblique imagery. *Geoscientific Instrumentation Methods and Data Systems*. **7**, pp.277-288.
- Gómez-Gutiérrez Á., De Sanjosé-Blasco J., De Matías-Bejarano J. and Berenguer-Sempere F. 2014. Comparing Two Photo-Reconstruction Methods to Produce High Density Point Clouds and DEMs in the Corral del Veleta Rock Glacier (Sierra Nevada, Spain). *Remote Sensing*. **6**, pp.5407-5427.
- Gordon J.E. 1986. Glacial lake drainage near Søndre Strømfjord, West Greenland. *Journal of Glaciology*. **32**, pp.304-304.
- Gudmundsson S., Björnsson H., Pálsson F., Magnússon E., Saemundsson T. and Jóhannesson T. 2019. Terminus lakes on the south side of Vatnajökull ice cap, SE-Iceland. *Jökull*. **69**, pp.1-34.
- Haeberli W., Buetler M., Huggel C., Friedli T.L., Schaub Y. and Schleiss A.J. 2016. New lakes in deglaciating high-mountain regions – opportunities and risks. *Climatic Change*. **139**, pp.201-214.
- Hall D.K., Riggs G.A. and Salomonson V.V. 1995. Development of methods for mapping global snow cover using moderate resolution imaging spectroradiometer data. *Remote Sensing of Environment*. **54**, pp.127-140.
- Hanna E., Huybrechts P., Steffen K., Cappelen J., Huff R., Shuman C., Irvine-Fynn T., Wise S. and Griffiths M. 2008. Increased runoff from melt from the Greenland Ice Sheet: A response to global warming. *Journal of Climate*. **21**, pp.331-341.

- Hanna E., Navarro F.J., Pattyn F., Domingues C.M., Fettweis X., Ivins E.R., Nicholls R.J., Ritz C., Smith B., Tulaczyk S., Whitehouse P.L. and Zwally H.J. 2013. Ice-sheet mass balance and climate change. *Nature*. **498**, pp.51-59.
- Haresign E. and Warren C.R. 2005. Melt rates at calving termini: a study at Glaciar León, Chilean Patagonia. *Geological Society, London, Special Publications*. **242**, pp.99-109.
- Hasholt B., Mikkelsen A.B., Nielsen M.H. and Larsen M.A.D. 2013. Observations of Runoff and Sediment and Dissolved Loads from the Greenland Ice Sheet at Kangerlussuaq, West Greenland, 2007 to 2010. *Zeitschrift für Geomorphologie*. **57**, pp.3-27.
- Hasholt B., van As D., Mikkelsen A.B., Mernild S.H. and Yde J.C. 2018. Observed sediment and solute transport from the Kangerlussuaq sector of the Greenland Ice Sheet (2006–2016). *Arctic, Antarctic, and Alpine Research*. **50**, S100009.
- Higgins A.K. 1970. On some ice-dammed lakes in the Frederikshåb district, south-west Greenland. *Meddelelser fra Dansk Geologisk Forening*. **19**, pp.378-397.
- Hill E.A., Carr J.R., Stokes C.R. and Gudmundsson G.H. 2018. Dynamic changes in outlet glaciers in northern Greenland from 1948 to 2015. *The Cryosphere*. **12**, pp.3243-3263.
- Hinck S., Gowan E.J. and Lohmann G. 2020. LakeCC: a tool for efficiently identifying lake basins with application to palaeogeographic reconstructions of North America. *Journal of Quaternary Science*. **35**, pp.422-432.
- Holland D.M., Thomas R.H., De Young B., Ribergaard M.H. and Lyberth B. 2008. Acceleration of Jakobshavn Isbræ triggered by warm subsurface ocean waters. *Nature Geoscience*. **1**, pp.659-664.
- How P., Hulton N.R.J., Buie L. and Benn D.I. 2020. PyTrx: A Python-based monoscopic terrestrial photogrammetry toolset for glaciology. *Frontiers in Earth Science*. **8**, 2020.00021.
- How P., Schild K.M., Benn D.I., Noormets R., Kirchner N., Luckman A., Vallot D., Hulton N.R.J. and Borstad C. 2019. Calving controlled by melt-under-cutting: detailed calving styles revealed through time-lapse observations. *Annals of Glaciology*. **60**, pp.20-31.
- Howat I.M., Box J.E., Ahn Y., Herrington A. and Mcfadden E.M. 2010. Seasonal variability in the dynamics of marine-terminating outlet glaciers in Greenland. *Journal of Glaciology*. **56**, pp.601-613.
- Howat I.M., Joughin I., Fahnestock M., Smith B.E. and Scambos T.A. 2008. Synchronous retreat and acceleration of southeast Greenland outlet glaciers 2000-06: ice dynamics and coupling to climate. *Journal of Glaciology*. **54**, pp.646-660.

Huggel C., Kaab A., Haeberli W., Teyssie P. and Paul F. 2002. Remote sensing based assessment of hazards from glacier lake outbursts: a case study in the Swiss Alps. *Canadian Geotechnical Journal*. **39**, pp.316-330.

Huss M., Bauder A., Werder M., Funk M. and Hock R. 2007. Glacier-dammed lake outburst events of Gornersee, Switzerland. *Journal of Glaciology*. **53**, pp.189-200.

Immerzeel W.W., Kraaijenbrink P.D.A., Shea J.M., Shrestha A.B., Pellicciotti F., Bierkens M.F.P. and De Jong S.M. 2014. High-resolution monitoring of Himalayan glacier dynamics using unmanned aerial vehicles. *Remote Sensing of Environment*. **150**, pp.93-103.

James M.R., How P. and Wynn P.M. 2016. Pointcatcher software: analysis of glacial time-lapse photography and integration with multitemporal digital elevation models. *Journal of Glaciology*. **62**, pp.159-169.

James M.R. and Robson S. 2012. Straightforward reconstruction of 3D surfaces and topography with a camera: Accuracy and geoscience application. *Journal of Geophysical Research: Earth Surface*. **117**, F03017.

James M.R. and Robson S. 2014a. Sequential digital elevation models of active lava flows from ground-based stereo time-lapse imagery. *ISPRS Journal of Photogrammetry and Remote Sensing*. **97**, pp.160-170.

James M.R. and Robson S. 2014b. Mitigating systematic error in topographic models derived from UAV and ground-based image networks. *Earth Surface Processes and Landforms*. **39**, pp.1413-1420.

James M.R., Robson S., D'oleire-Oltmanns S. and Niethammer U. 2017. Optimising UAV topographic surveys processed with structure-from-motion: Ground control quality, quantity and bundle adjustment. *Geomorphology*. **280**, pp.51-66.

Javemick L., Brasington J. and Caruso B. 2014. Modeling the topography of shallow braided rivers using Structure-from-Motion photogrammetry. *Geomorphology*. **213**, pp.166-182.

Jiang Y., Dixon T.H. and Wdowinski S. 2010. Accelerating uplift in the North Atlantic region as an indicator of ice loss. *Nature Geoscience*. **3**, pp.404-407.

Jones D.H., Robinson C. and Gudmundsson G.H. 2016. A new high-precision and low-power GNSS receiver for long-term installations in remote areas. *Geoscientific Instrumentation, Methods and Data Systems*. **5**, pp.65-73.

Joughin I., Howat I.M., Fahnestock M., Smith B., Krabill W., Alley R.B., Stern H. and Truffer M. 2008. Continued evolution of Jakobshavn Isbrae following its rapid speedup. *Journal of Geophysical Research: Earth Surface*. **113**, F04006.

Joughin I., Smith B.E., Howat I.M., Floricioiu D., Alley R.B., Truffer M. and Fahnestock M. 2012. Seasonal to decadal scale variations in the surface velocity of Jakobshavn Isbrae, Greenland: Observation and model-based analysis. *Journal of Geophysical Research: Earth Surface*. **117**, F02030.

Joughin I., Smith B.E., Howat I.M., Scambos T. and Moon T. 2010. Greenland flow variability from ice-sheet-wide velocity mapping. *Journal of Glaciology*. **56**, pp.415-430.

Jouvet G., Weidmann Y., Van Dongen E., Lüthi M.P., Vieli A. and Ryan J.C. 2019. High-Endurance UAV for Monitoring Calving Glaciers: Application to the Inglefield Bredning and Eqip Sermia, Greenland. *Frontiers in Earth Science*. **7**, 2019.00206.

Kargel J.S., Ahlstrøm A.P., Alley R.B., Bamber J.L., Benham T.J., Box J.E., Chen C., Christoffersen P., Citterio M., Cogley J.G., Jiskoot H., Leonard G.J., Morin P., Scambos T., Sheldon T. and Willis I. 2012. Brief communication: Greenland's shrinking ice cover: "Fast times" but not that fast. *The Cryosphere*. **6**, pp.533-537.

Kennett M., Laumann T. and Kjollmoen B. 1997. Predicted response of the calving glacier Svartisheibreen, Norway, and outbursts from it, to future changes in climate and lake level. *Annals of Glaciology*. **24**, pp.16-20.

Khan S.A., Aschwanden A., Bjork A.A., Wahr J., Kjeldsen K.K. and Kjaer K.H. 2015. Greenland ice sheet mass balance: a review. *Reports on Progress in Physics*. **78**, 046801.

Kienholz C., Pierce J., Hood E., Amundson J.M., Wolken G.J., Jacobs A., Hart S., Wikstrom Jones K., Abdel-Fattah D., Johnson C. and Conaway J.S. 2020. Deglaciation of a Marginal Basin and Implications for Outburst Floods, Mendenhall Glacier, Alaska. *Frontiers in Earth Science*. **8**, 2020.00137.

King O., Bhattacharya A., Bhambri R. and Bolch T. 2019. Glacial lakes exacerbate Himalayan glacier mass loss. *Scientific Reports*. **9**, 18145.

King O., Dehecq A., Quincey D. and Carrivick J. 2018. Contrasting geometric and dynamic evolution of lake and land-terminating glaciers in the central Himalaya. *Global and Planetary Change*. **167**, pp.46-60.

Kirkbride M.P. 1993. The temporal significance of transitions from melting to calving termini at glaciers in the central Southern Alps of New Zealand. *The Holocene*. **3**, pp.232-240.

Kirkbride M.P. and Warren C.R. 1997. Calving processes at a grounded ice cliff. *Annals of Glaciology*. **24**, pp.116-121.

Kjeldsen K.K., Korsgaard N.J., Bjork A.A., Khan S.A., Box J.E., Funder S., Larsen N.K., Bamber J.L., Colgan W., Van Den Broeke M., Siggaard-Andersen M.L., Nuth C., Schomacker A., Andresen C.S., Willerslev E. and Kjaer K.H. 2015. Spatial and temporal distribution of mass loss from the Greenland Ice Sheet since AD 1900. *Nature*. **528**, pp.396-400.

Knight P.G., Waller R.I., Patterson C.J., Jones A.P. and Robinson Z.P. 2000. Glacier advance, ice-marginal lakes and routing of meltwater and sediment: Russell Glacier, Greenland. *Journal of Glaciology*. **46**, pp.423-426.

Knudsen N.T. and Theakstone W.H. 1988. Drainage of the Austre-Okstindbreen ice-dammed lake, Okstindan, Norway. *Journal of Glaciology*. **34**, pp.87-94.

Koller M. 2016. robustlmm: An R Package for Robust Estimation of Linear Mixed-Effects Models. *Journal of Statistical Software*. **75**, pp.1-24.

Komori J. 2008. Recent expansions of glacial lakes in the Bhutan Himalayas. *Quaternary International*. **184**, pp.177-186.

Korsgaard N.J., Nuth C., Khan S.A., Kjeldsen K.K., Bjørk A.A., Schomacker A. and Kjær K.H. 2016. Digital elevation model and orthophotographs of Greenland based on aerial photographs from 1978–1987. *Scientific Data*. **3**, 160032.

Kraaijenbrink P., Meijer S.W., Shea J.M., Pellicciotti F., De Jong S.M. and Immerzeel W.W. 2016. Seasonal surface velocities of a Himalayan glacier derived by automated correlation of unmanned aerial vehicle imagery. *Annals of Glaciology*. **57**, pp.103-113.

Krabill W., Hanna E., Huybrechts P., Abdalati W., Cappelen J., Csatho B., Frederick E., Manizade S., Martin C., Sonntag J., Swift R., Thomas R. and Yungel J. 2004. Greenland Ice Sheet: Increased coastal thinning. *Geophysical Research Letters*. **31**, L24402.

Krinner G., Mangerud J., Jakobsson M., Crucifix M., Ritz C. and Svendsen J.I. 2004. Enhanced ice sheet growth in Eurasia owing to adjacent ice-dammed lakes. *Nature*. **427**, pp.429-432.

Kromer R.A., Abellán A., Hutchinson D.J., Lato M., Chanut M.A., Dubois L. and Jaboyedoff M. 2017. Automated terrestrial laser scanning with near-real-time change detection - monitoring of the Séchilienne landslide. *Earth Surface Dynamics*. **5**, pp.293-310.

Lague D., Brodu N. and Leroux J. 2013. Accurate 3D comparison of complex topography with terrestrial laser scanner: Application to the Rangitikei canyon (N-Z). *ISPRS Journal of Photogrammetry and Remote Sensing*. **82**, pp.10-26.

Larsen C.F., Burgess E., Arendt A.A., O'neel S., Johnson A.J. and Kienholz C. 2015. Surface melt dominates Alaska glacier mass balance. *Geophysical Research Letters*. **42**, pp.5902-5908.



Larsen C.F., Motyka R.J., Arendt A.A., Echelmeyer K.A. and Geissler P.E. 2007. Glacier changes in southeast Alaska and northwest British Columbia and contribution to sea level rise. *Journal of Geophysical Research: Earth Surface*. **112**, F01007.

Lea J.M., Mair D.W.F. and Rea B.R. 2014. Evaluation of existing and new methods of tracking glacier terminus change. *Journal of Glaciology*. **60**, pp.323-332.

Leclercq P.W., Weidick A., Paul F., Bolch T., Citterio M. and Oerlemans J. 2012. Brief communication: Historical glacier length changes in West Greenland. *The Cryosphere*. **6**, pp.1339-1343.

Lesnek A.J., Briner J.P., Young N.E. and Cuzzone J.K. 2020. Maximum southwest Greenland ice sheet recession in the early Holocene. *Geophysical Research Letters*. **47**, GL083164.

Lindbäck K., Pettersson R., Doyle S.H., Helanow C., Jansson P., Kristensen S.S., Stenseng L., Forsberg R. and Hubbard A.L. 2014. High-resolution ice thickness and bed topography of a land-terminating section of the Greenland Ice Sheet. *Earth System Science Data*. **6**, pp.331-338.

Liu Q., Mayer C., Wang X., Nie Y., Wu K., Wei J. and Liu S. 2020. Interannual flow dynamics driven by frontal retreat of a lake-terminating glacier in the Chinese Central Himalaya. *Earth and Planetary Science Letters*. **546**, 116450.

Loriaux T. and Casassa G. 2013. Evolution of glacial lakes from the Northern Patagonia Icefield and terrestrial water storage in a sea-level rise context. *Global and Planetary Change*. **102**, pp.33-40.

Lovell A.M., Carr J.R. and Stokes C.R. 2019. Spatially Variable Glacier Changes in the Annapurna Conservation Area, Nepal, 2000 to 2016. *Remote Sensing*. **11**, 1452.

Mallalieu J., Carrivick J.L., Quincey D.J. and Smith M.W. 2020. Calving seasonality associated with melt-undercutting and lake ice cover. *Geophysical Research Letters*. **47**, GL086561.

Mallalieu J., Carrivick J.L., Quincey D.J., Smith M.W. and James W.H.M. 2017. An integrated Structure-from-Motion and time-lapse technique for quantifying ice-margin dynamics. *Journal of Glaciology*. **63**, pp.937-949.

Mangerud J., Jakobsson M., Alexanderson H., Astakhov V., Clarke G.K.C., Henriksen M., Hjort C., Krinner G., Lunkka J.P., Moller P., Murray A., Nikolskaya O., Saarnisto M. and Svendsen J.I. 2004. Ice-dammed lakes and rerouting of the drainage of northern Eurasia during the Last Glaciation. *Quaternary Science Reviews*. **23**, pp.1313-1332.

- Mätzler E., Messerli A., How P., Høegh Bojesen M., Langley K., Santoro M., Wiesmann A., Caduff R., Strozzi T., Käab A. and Paul F. 2019. *A Greenland-wide inventory of ice marginal lakes*. [Poster]. International Glaciological Society Nordic Branch Meeting, 30<sup>th</sup> October - 1<sup>st</sup> November 2019, Reykholt, Iceland.
- Mayer C., Lambrecht A., Hagg W., Helm A. and Scharrer K. 2008. Post-drainage ice dam response at Lake Merzbacher, Inylchek glacier, Kyrgyzstan. *Geografiska Annaler*. **90A**, pp.87-96.
- Mayer C. and Schuler T.V. 2005. Breaching of an ice dam at Qorlortossup tasia, south Greenland. *Annals of Glaciology*. **42**, pp.297-302.
- Mcfadden E.M., Howat I.M., Joughin I., Smith B.E. and Ahn Y. 2011. Changes in the dynamics of marine terminating outlet glaciers in west Greenland (2000–2009). *Journal of Geophysical Research: Earth Surface*. **116**, F02022.
- Mcfeters S.K. 1996. The use of the Normalized Difference Water Index (NDWI) in the delineation of open water features. *International Journal of Remote Sensing*. **17**, pp.1425-1432.
- Medrzycka D., Benn D.I., Box J.E., Copland L. and Balog J. 2016. Calving behavior at Rink Isbrae, West Greenland, from time-lapse photos. *Arctic, Antarctic and Alpine Research*. **48**, pp.263-277.
- Mernild S.H. and Hasholt B. 2009. Observed runoff, jokulhlaups and suspended sediment load from the Greenland ice sheet at Kangerlussuaq, West Greenland, 2007 and 2008. *Journal of Glaciology*. **55**, pp.855-858.
- Mernild S.H., Malmros J.K., Yde J.C. and Knudsen N.T. 2012. Multi-decadal marine- and land-terminating glacier recession in the Ammassalik region, southeast Greenland. *The Cryosphere*. **6**, pp.625-639.
- Mertes J.R., Gulley J.D., Benn D.I., Thompson S.S. and Nicholson L.I. 2017. Using structure-from-motion to create glacier DEMs and orthoimagery from historical terrestrial and oblique aerial imagery. *Earth Surface Processes and Landforms*. **42**, pp.2350-2364.
- Micheletti N., Chandler J.H. and Lane S.N. 2015. Investigating the geomorphological potential of freely available and accessible structure-from-motion photogrammetry using a smartphone. *Earth Surface Processes and Landforms*. **40**, pp.473-486.
- Midgley N.G. and Tonkin T.N. 2017. Reconstruction of former glacier surface topography from archive oblique aerial images. *Geomorphology*. **282**, pp.18-26.

Mikkelsen A.B., Hasholt B., Knudsen N.T. and Nielsen M.H. 2013. Jökulhlaups and sediment transport in Watson River, Kangerlussuaq, West Greenland. *Hydrology Research*. **44**, pp.58-67.

Minowa M., Podolskiy E.A., Sugiyama S., Sakakibara D. and Skvarca P. 2018. Glacier calving observed with time-lapse imagery and tsunami waves at Glaciar Perito Moreno, Patagonia. *Journal of Glaciology*. **64**, pp.362-376.

Minowa M., Sugiyama S., Sakakibara D. and Skvarca P. 2017. Seasonal Variations in Ice-Front Position Controlled by Frontal Ablation at Glaciar Perito Moreno, the Southern Patagonia Icefield. *Frontiers in Earth Science*. **5**, 2017.00001.

Molg N. and Bolch T. 2017. Structure-from-Motion Using Historical Aerial Images to Analyse Changes in Glacier Surface Elevation. *Remote Sensing*. **9**, 1021.

Moon T. and Joughin I. 2008. Changes in ice front position on Greenland's outlet glaciers from 1992 to 2007. *Journal of Geophysical Research: Earth Surface*. **113**, F02022.

Morlighem M., Williams C.N., Rignot E., An L., Arndt J.E., Bamber J.L., Catania G., Chauché N., Dowdeswell J.A., Dorschel B., Fenty I., Hogan K., Howat I., Hubbard A., Jakobsson M., Jordan T.M., Kjeldsen K.K., Millan R., Mayer L., Mouginot J., Noël B.P.Y., O'Cofaigh C., Palmer S., Rysgaard S., Seroussi H., Siegert M.J., Slabon P., Straneo F., Van den broeke M.R., Weinrebe W., Wood M. and Zinglarsen K.B. 2017. BedMachine v3: Complete Bed Topography and Ocean Bathymetry Mapping of Greenland From Multibeam Echo Sounding Combined With Mass Conservation. *Geophysical Research Letters*. **44**, pp.11051-11061.

Motyka R.J., Hunter L., Echelmeyer K. and Connor C. 2003a. Submarine melting at the terminus of a temperate tidewater glacier, LeConte Glacier, Alaska, U.S.A. *Annals of Glaciology*. **36**, pp.57-65.

Motyka R.J., O'Neel S., Connor C.L. and Echelmeyer K.A. 2003b. Twentieth century thinning of Mendenhall Glacier, Alaska, and its relationship to climate, lake calving, and glacier runoff. *Global and Planetary Change*. **35**, pp.93-112.

Mouginot J., Rignot E., Bjørk A.A., Van Den Broeke M., Millan R., Morlighem M., Noël B., Scheuchl B. and Wood M. 2019. Forty-six years of Greenland Ice Sheet mass balance from 1972 to 2018. *Proceedings of the National Academy of Sciences*. **116**, pp.9239-9244.

Murray T., Selmes N., James T.D., Edwards S., Martin I., O'farrell T., Aspey R., Rutt I., Nettles M. and Bauge T. 2015. Dynamics of glacier calving at the ungrounded margin of Helheim Glacier, southeast Greenland. *Journal of Geophysical Research: Earth Surface*. **120**, pp.964-982.

Mulsow C., Koschitzki R. and Maas H.G. 2015. Photogrammetric monitoring of glacier margin lakes. *Geomatics, Natural Hazards and Risk*. **6**, pp.600-613.

Myers P.G., Kulan N. and Ribergaard M.H. 2007. Irminger Water variability in the West Greenland Current. *Geophysical Research Letters*. **34**, L17601.

Naruse R. and Skvarca P. 2000. Dynamic features of thinning and retreating Glaciar Upsala, a Lacustrine Calving Glacier in southern Patagonia. *Arctic, Antarctic and Alpine Research*. **32**, pp.485-491.

Nick F.M., Vieli A., Andersen M.L., Joughin I., Payne A., Edwards T.L., Pattyn F. and van de Wal R.S.W. 2013. Future sea-level rise from Greenland's main outlet glaciers in a warming climate. *Nature*. **497**, pp.235-238.

Nie Y., Sheng Y., Liu Q., Liu L., Liu S., Zhang Y. and Song C. 2017. A regional-scale assessment of Himalayan glacial lake changes using satellite observations from 1990 to 2015. *Remote Sensing of Environment*. **189**, pp.1-13.

Parastatidis D., Mitraka Z., Chrysoulakis N. and Abrams M. 2017. Online Global Land Surface Temperature Estimation from Landsat. *Remote Sensing*. **9**, 1208.

Parente L., Chandler J.H. and Dixon N. 2019. Optimising the quality of an SfM-MVS slope monitoring system using fixed cameras. *The Photogrammetric Record*. **34**, pp.408-427.

Patton H., Hubbard A., Andreassen K., Auriac A., Whitehouse P.L., Stroeven A.P., Shackleton C., Winsborrow M., Heyman J. and Hall A.M. 2017. Deglaciation of the Eurasian ice sheet complex. *Quaternary Science Reviews*. **169**, pp.148-172

Pattyn F., Ritz C., Hanna E., Asay-Davis X., Deconto R., Durand G., Favier L., Fettweis X., Goelzer H., Gollledge N.R., Kuipers Munneke P., Lenaerts J.T.M., Nowicki S., Payne A.J., Robinson A., Seroussi H., Trusel L.D. and Van Den Broeke M. 2018. The Greenland and Antarctic ice sheets under 1.5 °C global warming. *Nature Climate Change*. **8**, pp.1053-1061.

Paul F., Kaab A. and Haeberli W. 2007. Recent glacier changes in the Alps observed by satellite: Consequences for future monitoring strategies. *Global and Planetary Change*. **56**, pp.111-122.

Pelto M.S. and Hedlund C. 2001. Terminus behavior and response time of North Cascade glaciers, Washington, U.S.A. *Journal of Glaciology*. **47**, pp.497-506.

Perkins A.J. and Brennand T.A. 2015. Refining the pattern and style of Cordilleran Ice Sheet retreat: palaeogeography, evolution and implications of lateglacial ice-dammed lake systems on the southern Fraser Plateau, British Columbia, Canada. *Boreas*. **44**, pp.319-342.

Pętllicki M., Cieplý M., Jania J.A., Promińska A. and Kinnard C. 2015. Calving of a tidewater glacier driven by melting at the waterline. *Journal of Glaciology*. **61**, pp.851-863.

- Piermattei L., Carturan L. and Guarnieri A. 2015. Use of terrestrial photogrammetry based on structure-from-motion for mass balance estimation of a small glacier in the Italian alps. *Earth Surface Processes and Landforms*. **40**, pp.1791-1802.
- Pierre K.A.S., Louis V.L.S., Schiff S.L., Lehnherr I., Dainard P.G., Gardner A.S., Aukes P.J. and Sharp M.J. 2019. Proglacial freshwaters are significant and previously unrecognized sinks of atmospheric CO<sub>2</sub>. *Proceedings of the National Academy of Sciences*. **116**, pp.17690-17695.
- Podgorski J., Pełlicki M. and Kinnard C. 2018. Revealing recent calving activity of a tidewater glacier with terrestrial LiDAR reflection intensity. *Cold Regions Science and Technology*. **151**, pp.288-301.
- Podrasky D., Truffer M., Lüthi M. and Fahnestock M. 2014. Quantifying velocity response to ocean tides and calving near the terminus of Jakobshavn Isbrae, Greenland. *Journal of Glaciology*. **60**, pp.609-621.
- Porter C., Morin P., Howat I., Noh M.J., Bates B., Peterman K., Keesey S., Schlenk M., Gardiner J., Tomko K., Willis M., Kelleher C., Cloutier M., Husby E., Foga S., Nakamura H., Platson M., Wethington M., Williamson C., Bauer G., Enos J., Arnold G., Kramer W., Becker P., Doshi A., D'Souza C., Cummins P., Laurier F. and Bojesen M. 2018. ArcticDEM. *National Geospatial-Intelligence Agency and National Science Foundation*. [Online]. [Accessed 1 July 2020]. Available from: <https://doi.org/10.7910/DVN/OHHUKH>
- Porter D.F., Tinto K.J., Boghosian A.L., Csatho B.M., Bell R.E. and Cochran J.R. 2018. Identifying Spatial Variability in Greenland's Outlet Glacier Response to Ocean Heat. *Frontiers in Earth Science*. **6**, 2018.00090.
- Price S.F., Payne A.J., Catania G.A. and Neumann T.A. 2008. Seasonal acceleration of inland ice via longitudinal coupling to marginal ice. *Journal of Glaciology*. **54**, pp.213-219.
- Pritchard H.D., Arthern R.J., Vaughan D.G. and Edwards L.A. 2009. Extensive dynamic thinning on the margins of the Greenland and Antarctic ice sheets. *Nature*. **461**, pp.971-975.
- Purdie H., Bealing P., Tidey E., Gomez C. and Harrison J. 2016. Bathymetric evolution of Tasman Glacier terminal lake, New Zealand, as determined by remote surveying techniques. *Global and Planetary Change*. **147**, pp.1-11.
- Quincey D.J. and Glasser N.F. 2009. Morphological and ice-dynamical changes on the Tasman Glacier, New Zealand, 1990-2007. *Global and Planetary Change*. **68**, pp.185-197.
- Quincey D.J. and Luckman A. 2009. Progress in satellite remote sensing of ice sheets. *Progress in Physical Geography*. **33**, pp.547-567.

- Quincey D.J., Richardson S.D., Luckman A., Lucas R.M., Reynolds J.M., Hambrey M.J. and Glasser N.F. 2007. Early recognition of glacial lake hazards in the Himalaya using remote sensing datasets. *Global and Planetary Change*. **56**, pp.137-152.
- Quincey D.J., Smith M.W., Rounce D., Ross A., King O. and Watson C.S. 2017. Evaluating morphological estimates of the aerodynamic roughness of debris covered glacier ice. *Earth Surface Processes and Landforms*. **42**, pp.2541-2553.
- R Core Team 2019. *R: A Language and Environment for Statistical Computing*. R Foundation for Statistical Computing. Vienna, Austria. URL <https://www.R-project.org/>.
- Rastner P., Bolch T., Molg N., Machguth H., Le Bris R. and Paul F. 2012. The first complete inventory of the local glaciers and ice caps on Greenland. *The Cryosphere*. **6**, pp.1483-1495.
- Rastner P., Bolch T., Notarnicola C. and Paul F. 2014. A Comparison of Pixel- and Object-Based Glacier Classification With Optical Satellite Images. *IEEE Journal of Selected Topics in Applied Earth Observations and Remote Sensing*. **7**, pp.853-862.
- Reynolds J.M. 2000. On the formation of supraglacial lakes on debris-covered glaciers. In: Nakawo M., Raymond C.F. and Fountain A. (eds.) *Debris-Covered Glaciers*. Wallingford: International Association of Hydrological Sciences, pp.153-161.
- Riesen P., Sugiyama S. and Funk M. 2010. The influence of the presence and drainage of an ice-marginal lake on the flow of Gornergletscher, Switzerland. *Journal of Glaciology*. **56**, pp.278-286.
- Rignot E., Fenty I., Xu Y., Cai C. and Kemp C. 2015. Undercutting of marine-terminating glaciers in West Greenland. *Geophysical Research Letters*. **42**, pp.5909-5917.
- Rignot E. and Mouginot J. 2012. Ice flow in Greenland for the International Polar Year 2008–2009. *Geophysical Research Letters*. **39**, L11501.
- Rivera A., Corripio J., Bravo C. and Cisternas S. 2012. Glaciar Jorge Montt (Chilean Patagonia) dynamics derived from photos obtained by fixed cameras and satellite image feature tracking. *Annals of Glaciology*. **53**, pp.147-155.
- Roberts M.J., Palsson F., Gudmundsson M.T., Bjornsson H. and Tweed F.S. 2005. Ice-water interactions during floods from Graenalon glacier-dammed lake, Iceland. *Annals of Glaciology*. **40**, pp.133-138.
- Röhl K. 2006. Thermo-erosional notch development at fresh-water-calving Tasman Glacier, New Zealand. *Journal of Glaciology*. **52**, pp.203-213.

Rosenau R., Schwalbe E., Maas H.G., Baessler M. and Dietrich R. 2013. Grounding line migration and high-resolution calving dynamics of Jakobshavn Isbræ, West Greenland. *Journal of Geophysical Research: Earth Surface*. **118**, pp.382-395.

Rosentau A., Vassiljev J., Hang T., Saarse L. and Kalm V. 2009. Development of the Baltic Ice Lake in the eastern Baltic. *Quaternary International*. **206**, pp.16-23.

Roy D.P., Wulder M.A., Loveland T.R., C.E W., Allen R.G., Anderson M.C., Helder D., Irons J.R., Johnson D.M., Kennedy R., Scambos T.A., Schaaf C.B., Schott J.R., Sheng Y., Vermote E.F., Belward A.S., Bindschadler R., Cohen W.B., Gao F., Hipple J.D., Hostert P., Huntington J., Justice C.O., Kilic A., Kovalskyy V., Lee Z.P., Lymburner L., Masek J.G., Mccorkel J., Shuai Y., Trezza R., Vogelmann J., Wynne R.H. and Zhu Z. 2014. Landsat-8: Science and product vision for terrestrial global change research. *Remote Sensing of Environment*. **145**, pp.154-172.

Russell A.J. 1989. A comparison of 2 recent jökulhlaups from an ice-dammed lake, Søndre Strømfjord, West Greenland. *Journal of Glaciology*. **35**, pp.157-162.

Russell A.J. 2007. Controls on the sedimentology of an ice-contact jokulhlaup-dominated delta, Kangerlussuaq, west Greenland. *Sedimentary Geology*. **193**, pp.131-148.

Russell A.J., Carrivick J.L., Ingeman-Nielsen T., Yde J.C. and Williams M. 2011. A new cycle of jokulhlaups at Russell Glacier, Kangerlussuaq, West Greenland. *Journal of Glaciology*. **57**, pp.238-246.

Ryan J.C., Hubbard A.L., Box J.E., Todd J., Christoffersen P., Carr J.R., Holt T.O. and Snooke N. 2015. UAV photogrammetry and structure from motion to assess calving dynamics at Store Glacier, a large outlet draining the Greenland ice sheet. *The Cryosphere*. **9**, pp.1-11.

Sakai A. and Fujita K. 2017. Contrasting glacier responses to recent climate change in high-mountain Asia. *Scientific Reports*. **7**, 13717.

Scherler D., Bookhagen B. and Strecker M.R. 2011. Spatially variable response of Himalayan glaciers to climate change affected by debris cover. *Nature Geoscience*. **4**, pp.156-159.

Schild K.M. and Hamilton G.S. 2013. Seasonal variations of outlet glacier terminus position in Greenland. *Journal of Glaciology*. **59**, pp.759-770.

Schomacker A. 2010. Expansion of ice-marginal lakes at the Vatnajökull ice cap, Iceland, from 1999 to 2009. *Geomorphology*. **119**, pp.232-236.

Schuenemann K.C. and Cassano J.J. 2010. Changes in synoptic weather patterns and Greenland precipitation in the 20th and 21st centuries: 2. Analysis of 21st century atmospheric changes using self-organizing maps. *Journal of Geophysical Research: Atmospheres*. **115**, D05108.

Seale A., Christoffersen P., Mugford R.I. and O'leary M. 2011. Ocean forcing of the Greenland Ice Sheet: Calving fronts and patterns of retreat identified by automatic satellite monitoring of eastern outlet glaciers. *Journal of Geophysical Research: Earth Surface*. **116**, F03013.

Shepherd A., Ivins E., Rignot E., Smith B., Van Den Broeke M., Velicogna I., Whitehouse P., Briggs K., Joughin I., Krinner G., Nowicki S., Payne T., Scambos T., Schlegel N., Geruo A., Agosta C., Ahlstrøm A., Babonis G., Barletta V.R., Bjørk A.A., Blazquez A., Bonin J., Colgan W., Csatho B., Cullather R., Engdahl M.E., Felikson D., Fettweis X., Forsberg R., Hogg A.E., Gallee H., Gardner A., Gilbert L., Gourmelen N., Groh A., Gunter B., Hanna E., Harig C., Helm V., Horvath A., Horwath M., Khan S., Kjeldsen K.K., Konrad H., Langen P.L., Lecavalier B., Loomis B., Luthcke S., Mcmillan M., Melini D., Mernild S., Mohajerani Y., Moore P., Mottram R., Mouginot J., Moyano G., Muir A., Nagler T., Nield G., Nilsson J., Noël B., Ootosaka I., Pattle M.E., Peltier W.R., Pie N., Rietbroek R., Rott H., Sørensen L.S., Sasgen I., Save H., Scheuchl B., Schrama E., Schröder L., Seo K.-W., Simonsen S.B., Slater T., Spada G., Sutterley T., Talpe M., Tarasov L., Jan Van De Berg W., Van Der Wal W., Van Wessem M., Vishwakarma B.D., Wiese D., Wilton D., Wagner T., Wouters B., Wuite J. and The Imbie Team. 2020. Mass balance of the Greenland Ice Sheet from 1992 to 2018. *Nature*. **579**, pp.233-239.

Silverio W. and Jaquet J.M. 2005. Glacial cover mapping (1987-1996) of the Cordillera Blanca (Peru) using satellite imagery. *Remote Sensing of Environment*. **95**, pp.342-350.

Skvarca P., Raup B. and De Angelis H. 2003. Recent behaviour of Glaciar Upsala, a fast-flowing calving glacier in Lago Argentino, southern Patagonia. *Annals of Glaciology*. **36**, pp.184-188.

Smejkalova T., Edwards M.E. and Dash J. 2016. Arctic lakes show strong decadal trend in earlier spring ice-out. *Scientific Reports*. **6**, 38449.

Smith M.W., Carrivick J.L. and Quincey D.J. 2016a. Structure from motion photogrammetry in physical geography. *Progress in Physical Geography*. **40**, pp.247-275.

Smith M.W., Quincey D.J., Dixon T., Bingham R.G., Carrivick J.L., Irvine-Fynn T.D.L. and Rippin D.M. 2016b. Aerodynamic roughness of glacial ice surfaces derived from high-resolution topographic data. *Journal of Geophysical Research: Earth Surface*. **121**, pp.748-766.

Smith M.W. and Vericat D. 2015. From experimental plots to experimental landscapes: topography, erosion and deposition in sub-humid badlands from Structure-from-Motion photogrammetry. *Earth Surface Processes and Landforms*. **40**, pp.1656-1671.

Snively N., Seitz S.M. and Szeliski R. 2006 Photo tourism: Exploring photo collections in 3D. *ACM Transactions on Graphics*. **25**, pp.835-846.

Stokes C.R. and Clark C.D. 2003. The Dubawnt Lake palaeo-ice stream: evidence for dynamic ice sheet behaviour on the Canadian Shield and insights regarding the controls on ice-stream location and vigour. *Boreas*. **32**, pp.263-279.



- Stokes C.R. and Clark C.D. 2004. Evolution of late glacial ice-marginal lakes on the northwestern Canadian Shield and their influence on the location of the Dubawnt Lake palaeo-ice stream. *Palaeogeography, Palaeoclimatology, Palaeoecology*. **215**, pp.155-171.
- Stokes C.R., Popovnin V., Aleynikov A., Gurney S.D. and Shahgedanova M. 2007. Recent glacier retreat in the Caucasus Mountains, Russia, and associated increase in supraglacial debris cover and supra-/proglacial lake development. *Annals of Glaciology*. **46**, pp.195-203.
- Storrar R.D., Jones A.H. and Evans D.J. 2017. Small-scale topographically-controlled glacier flow switching in an expanding proglacial lake at Breiðamerkurjökull, SE Iceland. *Journal of Glaciology*. **63**, pp.745-750.
- Straneo F. and Heimbach P. 2013. North Atlantic warming and the retreat of Greenland's outlet glaciers. *Nature*. **504**, pp.36-43.
- Stroeven A.P., Hattestrand C., Kleman J., Heyman J., Fabel D., Fredin O., Goodfellow B.W., Harbor J.M., Jansen J.D., Olsen L., Caffee M.W., Fink D., Lundqvist J., Rosqvist G.C., Stromberg B. and Jansson K.N. 2016. Deglaciation of Fennoscandia. *Quaternary Science Reviews*. **147**, pp.91-121.
- Sugden D.E., Clapperton C.M. and Knight P.G. 1985. A jokulhlaup near Sondre Stromfjord, West Greenland, and some effects on the ice-sheet margin. *Journal of Glaciology*. **31**, pp.366-368.
- Sugiyama S., Bauder A., Huss M., Riesen P. and Funk M. 2008. Triggering and drainage mechanisms of the 2004 glacier-dammed lake outburst in Gornergletscher, Switzerland. *Journal of Geophysical Research: Earth Surface*. **113**, F04019.
- Sugiyama S., Bauder A., Weiss P. and Funk M. 2007. Reversal of ice motion during the outburst of a glacier-dammed lake on Gornergletscher, Switzerland. *Journal of Glaciology*. **53**, pp.172-180.
- Sugiyama S., Minowa M., Sakakibara D., Skvarca P., Sawagaki T., Ohashi Y., Naito N. and Chikita K. 2016. Thermal structure of proglacial lakes in Patagonia. *Journal of Geophysical Research: Earth Surface*. **121**, pp.2270-2286.
- Sugiyama S., Minowa M. and Schaefer M. 2019. Underwater ice terrace observed at the front of Glaciar Grey, a freshwater calving glacier in Patagonia. *Geophysical Research Letters*. **46**, pp.2602-2609.
- Surdu C.M., Duguay C.R. and Prieto D.F. 2016. Evidence of recent changes in the ice regime of lakes in the Canadian High Arctic from spaceborne satellite observations. *The Cryosphere*. **10**, pp.941-960.

- Teller J.T. 1995. History and drainage of large ice-dammed lakes along the Laurentide Ice-Sheet. *Quaternary International*. **28**, pp.83-92.
- Thompson S., Benn D.I., Mertes J. and Luckman A. 2016. Stagnation and mass loss on a Himalayan debris-covered glacier: processes, patterns and rates. *Journal of Glaciology*. **62**, pp.467-485.
- Todd J., Christoffersen P., Zwinger T., Råback P. and Benn D.I. 2019. Sensitivity of a calving glacier to ice–ocean interactions under climate change: new insights from a 3-D full-Stokes model. *The Cryosphere*. **13**, pp.1681-1684.
- Tonini M. and Abellan A. 2014. Rockfall detection from terrestrial LiDAR point clouds: A clustering approach using R. *Journal of Spatial Information Science*. **8**, pp.95-110.
- Tonkin T.N., Midgley N.G., Cook S.J. and Graham D.J. 2016. Ice-cored moraine degradation mapped and quantified using an unmanned aerial vehicle: A case study from a polythermal glacier in Svalbard. *Geomorphology*. **258**, pp.1-10.
- Truffer M. and Motyka R.J. 2016. Where glaciers meet water: Subaqueous melt and its relevance to glaciers in various settings. *Reviews of Geophysics*. **54**, pp.220-239.
- Trusel L.D., Das S.B., Osman M.B., Evans M.J., Smith B.E., Fettweis X., McConnell J.R., Noël B.P.Y. and Van Den Broeke M.R. 2018. Nonlinear rise in Greenland runoff in response to post-industrial Arctic warming. *Nature*. **564**, pp.104-108.
- Trussel B.L., Motyka R.J., Truffer M. and Larsen C.F. 2013. Rapid thinning of lake-calving Yakutat Glacier and the collapse of the Yakutat Icefield, southeast Alaska, USA. *Journal of Glaciology*. **59**, pp.149-161.
- Tsutaki S., Fujita K., Nuimura T., Sakai A., Sugiyama S., Komori J. and Tshering P. 2019. Contrasting thinning patterns between lake- and land-terminating glaciers in the Bhutanese Himalaya. *The Cryosphere*. **13**, pp. 2733-2750.
- Tsutaki S., Nishimura D., Yoshizawa T. and Sugiyama S. 2011. Changes in glacier dynamics under the influence of proglacial lake formation in Rhonegletscher, Switzerland. *Annals of Glaciology*. **52**, pp.31-36.
- Tsutaki S., Sugiyama S., Nishimura D. and Funk M. 2013. Acceleration and flotation of a glacier terminus during formation of a proglacial lake in Rhonegletscher, Switzerland. *Journal of Glaciology*. **59**, pp.559-570.
- Tweed F.S. and Russell A.J. 1999. Controls on the formation and sudden drainage of glacier-impounded lakes: implications for jokulhlaup characteristics. *Progress in Physical Geography: Earth and Environment*. **23**, pp.79-110.

- Utting D.J. and Atkinson N. 2019. Proglacial lakes and the retreat pattern of the southwest Laurentide Ice Sheet across Alberta, Canada. *Quaternary Science Reviews*. **225**, 106034.
- Vallot D., Adinugroho S., Strand R., How P., Pettersson R., Benn D.I. and Hulton N.R.J. 2019. Automatic detection of calving events from time-lapse imagery at Tunabreen, Svalbard. *Geoscientific Instrumentation Methods and Data Systems*. **8**, pp.113-127.
- Van As D., Fausto R.S. and Team P.P. 2011. Programme for Monitoring of the Greenland Ice Sheet (PROMICE): first temperature and ablation records. *Geological Survey of Denmark and Greenland Bulletin*. **23**, pp.73-76.
- Van de Wal R.S.W., Greuell W., Van Den Broeke M.R., Reijmer C.H. and Oerlemans J. 2005. Surface mass-balance observations and automatic weather station data along a transect near Kangerlussuaq, West Greenland. *Annals of Glaciology*. **42**, pp.311-316.
- Van Den Broeke M., Bamber J., Ettema J., Rignot E., Schrama E., Van De Berg W.J., Van Meijgaard E., Velicogna I. and Wouters B. 2009. Partitioning Recent Greenland Mass Loss. *Science*. **326**, pp.984-986.
- Van Den Broeke M., Enderlin E.M., Howat I.M., Kuipers Munneke P., Noël B.P.Y., Van De Berg W.J., Van Meijgaard E. and Wouters B. 2016. On the recent contribution of the Greenland ice sheet to sea level change. *The Cryosphere*. **10**, pp.1933-1946.
- Van Den Broeke M., Smeets P., Ettema J. and Munneke P.K. 2008. Surface radiation balance in the ablation zone of the west Greenland ice sheet. *Journal of Geophysical Research: Atmospheres*. **113**, D13105.
- Van Der Veen C.J. 2002. Calving glaciers. *Progress in Physical Geography*. **26**, pp.96-122.
- Van Tatenhove F.G.M., Roelfsema C.M., Blommers G. and Voorden A.V. 1995. Change in position and altitude of a small outlet glacier during the period 1943–92: Leverett Glacier, West Greenland. *Annals of Glaciology*. **21**, pp.251-258.
- Veh G., Korup O. and Walz A. 2020. Hazard from Himalayan glacier lake outburst floods. *Proceedings of the National Academy of Sciences*. **117**, pp.907-912.
- Velicogna I. 2009. Increasing rates of mass loss from the Greenland and Antarctic ice sheets revealed by GRACE. *Geophysical Research Letters*. **36**, L19503.
- Vieli A., Jania J. and Kolondra L. 2002. The retreat of a tidewater glacier: observations and model calculations on Hansbreen, Spitsbergen. *Journal of Glaciology*. **48**, pp.592-600.
- Völksen C. and Mayer C. 2015. Monitoring the Continuous Surface Motion of Glaciers by Low-Cost GNSS Receivers. *EGU General Assembly*. Vienna: EGU.

- Wadham J.L., Hawkings J.R., Tarasov L., Gregoire L.J., Spencer R.G.M., Gutjahr M., Ridgwell A. and Kohfeld K.E. 2019. Ice sheets matter for the global carbon cycle. *Nature Communications*, **10**, pp.1-17.
- Walder J.S. and Costa J.E. 1996. Outburst floods from glacier-dammed lakes: The effect of mode of lake drainage on flood magnitude. *Earth Surface Processes and Landforms*. **21**, pp.701-723.
- Walder J.S., Trabant D.C., Cunico M., Fountain A.G., Anderson S.P., Anderson R.S. and Malm A. 2006. Local response of a glacier to annual filling and drainage of an ice-marginal lake. *Journal of Glaciology*. **52**, pp.440-450.
- Wang W.C., Yao T.D. and Yang X.X. 2011. Variations of glacial lakes and glaciers in the Boshula mountain range, southeast Tibet, from the 1970s to 2009. *Annals of Glaciology*. **52**, pp.9-17.
- Warren C.R. 1991. Terminal environment, topographic control and fluctuations of West Greenland glaciers. *Boreas*. **20**, pp.1-15.
- Warren C.R., Benn D., Winchester V. and Harrison S. 2001. Buoyancy-driven lacustrine calving, Glaciar Nef, Chilean Patagonia. *Journal of Glaciology*. **47**, pp.135-146.
- Warren C.R., Glasser N.F., Harrison S., Winchester V., Kerr A.R. and Rivera A. 1995b. Characteristics of tide-water calving at Glaciar San-Rafael, Chile. *Journal of Glaciology*. **41**, pp.273-289.
- Warren C.R., Greene D.R. and Glasser N.F. 1995a. Glaciar Upsala, Patagonia: Rapid calving retreat in fresh water. *Annals of Glaciology*. **21**, pp.311-316.
- Warren C.R. and Kirkbride M.P. 2003. Calving speed and climatic sensitivity of New Zealand lake-calving glaciers. *Annals of Glaciology*. **36**, pp.173-178.
- Warren C.R. and Rivera A. 1994. Nonlinear climatic response of calving glaciers - a case-study of Pio-Xi glacier, Chilean Patagonia. *Revista Chilena De Historia Natural*. **67**, pp.385-394.
- Watson C.S., Kargel J.S., Shugar D.H., Haritashya U.K., Schiassi E. and Furfaro R. 2020. Mass Loss From Calving in Himalayan Proglacial Lakes. *Frontiers in Earth Science*. **7**, 2019.00342.
- Watson C.S., Quincey D.J., Carrivick J.L. and Smith M.W. 2016. The dynamics of supraglacial ponds in the Everest region, central Himalaya. *Global and Planetary Change*. **142**, pp.14-27.
- Webster C., Westoby M., Rutter N. and Jonas T. 2018. Three-dimensional thermal characterization of forest canopies using UAV photogrammetry. *Remote Sensing of Environment*. **209**, pp.835-847.

Weidick A. 1991. Present-day expansion of the southern part of the Inland Ice. *Rapport Gronlands Geologiske Undersogelse*. **152**, pp.73-79.

Welty E.Z., Bartholomaeus T.C., O'neel S. and Pfeffer W.T. 2013. Cameras as clocks. *Journal of Glaciology*. **59**, pp.275-286.

Westoby M.J., Brasington J., Glasser N.F., Hambrey M.J. and Reynolds J.M. 2012. 'Structure-from-Motion' photogrammetry: A low-cost, effective tool for geoscience applications. *Geomorphology*. **179**, pp.300-314.

Westoby M.J., Dunning S.A., Woodward J., Hein A.S., Marrero S.M., Winters K. and Sugden D.E. 2016. Interannual surface evolution of an Antarctic blue-ice moraine using multi-temporal DEMs. *Earth Surface Dynamics*. **4**, pp.515-529.

Whitehead K., Moorman B.J. and Hugenholtz C.H. 2013. Brief Communication: Low-cost, on-demand aerial photogrammetry for glaciological measurement. *The Cryosphere*. **7**, pp.1879-1884.

Wilcox A.C., Wade A.A. and Evans E.G. 2014. Drainage events from a glacier-dammed lake, Bear Glacier, Alaska: Remote sensing and field observations. *Geomorphology*. **220**, pp.41-49.

Williams R.S. and Ferrigno J.G. 2012. State of the Earth's cryosphere at the beginning of the 21st century: glaciers, global snow cover, floating ice, and permafrost and periglacial environments. *Satellite Image Atlas of Glaciers of the World*. U.S. Geological Survey Professional Paper 1386-A.

Willis M.J., Melkonian A.K., Pritchard M.E. and Rivera A. 2012. Ice loss from the Southern Patagonian Ice Field, South America, between 2000 and 2012. *Geophysical Research Letters*. **39**, L17501.

Wilson R., Glasser N.F., Reynolds J.M., Harrison S., Anaconda P.I., Schaefer M. and Shannon S. 2018. Glacial lakes of the Central and Patagonian Andes. *Global and Planetary Change*. **162**, pp. 275-291.

Winsor K., Carlson A.E., Caffee M.W. and Rood D.H. 2015. Rapid last-deglacial thinning and retreat of the marine-terminating southwestern Greenland ice sheet. *Earth and Planetary Science Letters*. **426**, pp.1-12.

Wolfe D.F.G., Kargel J.S. and Leonard G.J. 2014. Glacier-dammed ice-marginal lakes of Alaska. In: Kargel J.S., Leonard G.J., Bishop M.P., Kaab A. and Raup B. (eds.) *Global Land Ice Measurements From Space*. Springer Praxis Books, pp.263-295.

Xie S., Dixon T.H., Holland D.M., Voytenko D. and Vaňková I. 2019. Rapid iceberg calving following removal of tightly packed pro-glacial mélange. *Nature Communications*. **10**, pp.3250-3215.

Yamasaki S., Tabusa T., Iwasaki S. and Hiramatsu, M. 2017. Acoustic water bottom investigation with a remotely operated watercraft survey system. *Progress in Earth and Planetary Science*. **4**, 25.

Yao T., Li Z., Yang W., Guo X., Zhu L., Kang S., Wu Y. and Yu W. 2010. Glacial distribution and mass balance in the Yarlung Zangbo River and its influence on lakes. *Chinese Science Bulletin*. **55**, pp.2072-2078.

Yde J.C., Knudsen N.T., Hasholt B. and Mikkelsen A. 2014. Meltwater chemistry and solute export from a Greenland Ice Sheet catchment, Watson River, West Greenland. *Journal of Hydrology*. **519**, pp. 2165-2179.

Zhang G., Yao T., Xie H., Wang W. and Yang W. 2015. An inventory of glacial lakes in the Third Pole region and their changes in response to global warming. *Global and Planetary Change*. **131**, pp.148-157.

Zwally H.J. 1989. Growth of Greenland ice sheet - Interpretation. *Science*. **246**, pp.1589-1591.

7 years - bloody hell!